

Electronic Thesis and Dissertation Repository

10-26-2022 2:00 PM

The Spectro-Temporal Relationships of Repeating Fast Radio Bursts

Mohammed Afif Chamma, *The University of Western Ontario*

Supervisor: Houde, Martin, *The University of Western Ontario*

A thesis submitted in partial fulfillment of the requirements for the Doctor of Philosophy degree in Astronomy

© Mohammed Afif Chamma 2022

Follow this and additional works at: <https://ir.lib.uwo.ca/etd>



Part of the [External Galaxies Commons](#), and the [Physical Processes Commons](#)

Recommended Citation

Chamma, Mohammed Afif, "The Spectro-Temporal Relationships of Repeating Fast Radio Bursts" (2022). *Electronic Thesis and Dissertation Repository*. 8958.
<https://ir.lib.uwo.ca/etd/8958>

This Dissertation/Thesis is brought to you for free and open access by Scholarship@Western. It has been accepted for inclusion in Electronic Thesis and Dissertation Repository by an authorized administrator of Scholarship@Western. For more information, please contact wlsadmin@uwo.ca.

Abstract

Fast radio bursts (FRBs) are short and extremely energetic bursts of radiation detected from galaxies across the universe that occur thousands of times a day. Despite advances in instrumentation, it is difficult to explain the enormous implied energy reservoirs of FRBs, their emission mechanism and the existence of repeating and periodic sources. This thesis explores the spectro-temporal properties of repeating FRBs and details the discovery of several new relationships between them, providing valuable information on the nature of FRBs. By measuring the spectro-temporal properties of a sample of bursts from the repeating source FRB20121102A I show that the magnitude of a burst’s time derivative of the frequency (or “sub-burst slope”) is inversely proportional to its duration. This relationship is a key prediction of the triggered relativistic dynamical model (TRDM), a model that assumes FRBs are inherently narrow-band in nature and originate from a cloud of material. I then investigate other FRB sources by analysing bursts from the repeaters FRB20180814A and FRB20180916B, discovering that the same slope-duration relationship describes the bursts from all three sources. Because FRBs are subject to dispersion by free ions along the line of sight, and because the measurement of spectro-temporal properties are dramatically affected by the choice of dispersion measure (DM), measurements of each burst are performed over a range of DMs to estimate uncertainties and validate any relationships found. Finally, I developed a software tool for preparing and measuring properties of FRBs and used it to survey a broad sample of 167 bursts from FRB20121102A. This sample spans 1 to 7 GHz, the entire range of burst frequencies observed for this source. I find relationships between a burst’s duration, slope, and frequency consistent with the TRDM, and discover an unexpected relationship between the bandwidth of a burst and its duration. These spectro-temporal relationships can be important tools and suggest a narrow-band emission mechanism for FRBs.

Keywords: Fast radio bursts, relativity, quantum optics, compact objects, transient astronomy, radio astronomy

Summary for General Audience

The sky can be observed in colors far beyond what our own eyes can see. At radio frequencies, radio telescopes can detect short bursts that come from extreme environments such as neutron stars. Fast radio bursts (FRBs) are one such type of burst discovered in 2007. Extremely bright and coming from distant galaxies, these bursts were difficult to discover because they are shorter than a few milliseconds and arrive at Earth distorted by the material between galaxies. This distortion is caused by electrons and other ions and is similar to the dispersion of white light by a prism into a rainbow. After correcting for this dispersion astronomers can study FRBs but to this day struggle to explain why there are thousands per day, where they come from, and how they can be bright enough to be seen from galaxies far beyond our own. Some sources of FRBs are also seen to repeat, and some of those still are periodic and follow a known schedule.

Telescopes today can split up the frequencies that make up an FRB like a prism does while measuring its brightness with time. With this information, we can make two-dimensional images of each burst called a waterfall. I study the shapes FRBs make in their waterfalls and use this information to understand what might be causing them. Bursts often appear as lines in their waterfalls, and I find that the steeper that line is, the shorter the burst. Patterns like this help us to understand what is happening, and by using physical theories like relativity we find we can explain the shapes FRBs make in their waterfalls. The patterns I have found are most easily explained if FRBs come from a cloud of atoms and are emitted at a single narrow frequency. These clouds could be triggered by a small dense object like a neutron star. The high speeds of these clouds, close to the speed of light, shift the frequency of that narrow signal and create the many waterfall shapes we later see on Earth.

Dedication

*To my father Walid, my mother Souhair, my sister Zahra, and my brother Wael for
their support, guidance, companionship, and love.*

Acknowledgements

I am grateful for the many people that made my experience as a graduate student feel fulfilling, supported, and wonderful.

I would like to thank my supervisor Martin Houde for his patient and gentle guidance over both my Master's and Doctoral degrees. Martin provided me with space to learn and to explore material at my own pace and was always generous with his knowledge, advice and wisdom. I am also grateful for the opportunities he gave me to visit Hawaii for research, Vienna for a conference, Madison for a workshop, and almost France, barring the interference of a certain virus. Martin's steadfastness during the pandemic helped calm my nerves and I would not have wanted any other supervisor to do my doctoral degree with. Thank you.

From the faculty, I am grateful to Sarah Gallagher, John Landstreet, Aaron Sigut and Stan Metchev, thank you for your support in reference letters, as advisers on my committee, as good teachers and for helpful conversations over the course of my degrees. I'm also grateful to Pauline Barmby for recruiting me to the department. I would like to thank Brian Davis and the department staff for their support and administrative knowledge in making my experience at Western smooth.

I am grateful to my group members, Christopher Wyenberg, Aishwarya Kumar, and Fereshteh Rajabi. They have been invaluable friends to me and provided many interesting and stimulating conversations over the years, as well as contributing to my research with their feedback, perspectives, and time.

I would like to thank all the friends I've made over my years here, including Sina, Ghazal, Chris, Aishwarya, Keegan, Dan, Alexis, Matt, Sham, Deepa, Megan. We've shared many laughs and good times and I love you all.

I am especially blessed and grateful for Yung, and the love and support and joy she brings to my life. Thank you for your affection, kindness, and energy, and I love you very much.

Finally, I am thankful for my family. My parents Walid and Souhair have made all of this possible through their love, caring, and wisdom. They made the difficult decision to immigrate to Canada from Lebanon and build a new life here starting with nothing but their drive and perseverance. I am blessed for my siblings Zahra and Wael and being your brother is a ton of fun and a great privilege of my life. I am grateful for my cousins Nizar and Nader, our lifelong friendship means a lot to me. Khalo Wael and Tante Hannah I am grateful for your warmth. To my cousins, aunts, uncles, grandparents and extended family in Lebanon, thank you for giving me a second home halfway around the world.

Co-Authorship Statement

The chapters of this thesis consist of three journal articles that were prepared with the help of co-authors and this statement will explain my contributions to the manuscripts and research work.

The first journal article is titled “A simple relationship for the spectro-temporal structure of bursts from FRB121102” and was published in Volume 493 of the Monthly Notices of the Royal Astronomical Society (MNRAS) on September 9, 2020. The published author list is Fereshteh Rajabi, myself, Christopher Wyenberg, Abhilash Mathews, and Martin Houde. This paper introduces the triggered relativistic dynamical model (TRDM) for FRBs and includes an analysis of bursts from FRB20121102A that show agreement with the predictions of the TRDM. My colleagues Fereshteh Rajabi and Martin Houde had the idea for the model and derived all the equations included in the manuscript. In the manuscript, they drafted the introduction and the sections describing the equations of the model, the predictions of the model, and discussion of the results of the burst analysis. With guidance from my supervisor, I wrote the software to perform measurements of the bursts, measured the properties of the bursts, found fits to the measured properties, and made Figures 1 to 5 of the manuscript. In the manuscript I wrote the methodology used to analyse the bursts, text explaining the figures, and also contributed to the discussion of the results. All authors including myself provided feedback and made edits to all parts of the text. This paper has been adapted into my thesis by placing the primary contributions of my co-authors (namely the description of the TRDM and its key equations) in Section 1.3.4 of the Introduction with my contributions focused on in Chapter 2.

The second journal article is titled “Evidence of a shared spectro-temporal law between sources of repeating fast radio bursts” and was published in Volume 507 of MNRAS on July 20, 2021, with author list starting with myself, Fereshteh Rajabi, Christopher Wyenberg, Abhilash Mathews, and Martin Houde. This paper extends the analysis done

in our previous work to two additional repeating FRB sources and finds that the same relationship found earlier connects the burst properties of these three sources. I wrote additional software for performing measurements, performed all the measurements, and made Figures 1, 2, 3, 5, and C1 to C5. I also came up with the idea to use ranges of dispersion measures (DMs) when performing measurements to address referee concerns about the effect of DM choice on our measurements, and our paper was accepted after this change. I drafted all sections of the paper. Christopher Wyenberg contributed section 3.3 of the paper discussing uncertainty due to frequency masking, and Martin Houde contributed section 3.4 discussing the narrow-band nature of the emission process. Martin Houde also contributed Appendix B of the paper and text in the main manuscript related to it. My co-authors contributed feedback and edits on the whole paper. This paper is included in its entirety in Chapter 3.

The final article is titled “A broad survey of spectro-temporal properties from FRB 20121102A” and has been submitted to MNRAS. I chose the topic of this paper, namely to test the limits of the TRDM and investigate if as many types of bursts as we could acquire from a single source broadly obeyed the same relationships or if differences could be observed. I wrote a graphical user interface called FRBGUI and used it to perform the measurements included in the paper. I also prepared the figures and entire draft of the manuscript with valuable feedback, discussion and edits from Martin Houde, including assistance with multiple mathematical derivations. Fereshteh Rajabi read the draft and provided significant edits on the structure of the paper. This work is in Chapter 4.

All burst waterfall data used in our studies were acquired through correspondence with their respective observers, as detailed in their corresponding chapters.

List of Publications

1. **Chamma, M. A.**, Houde, M., Girart, J. M., & Rao, R. (2018), “Non-Zeeman circular polarization of molecular spectral lines in the ISM”. MNRAS, 480, 3, pp. 3123-3131. DOI:[10.1093/mnras/sty2068](https://doi.org/10.1093/mnras/sty2068).
2. Rajabi, F., **Chamma, M. A.**, Wyenberg, C. M., Mathews, A., & Houde, M. (2020), “A simple relationship for the spectro-temporal structure of bursts from FRB 121102”. MNRAS, 498, 4, pp. 4936-4942. DOI:[10.1093/mnras/staa2723](https://doi.org/10.1093/mnras/staa2723).
3. **Chamma, M. A.**, Rajabi, F., Wyenberg, C. M., Mathews, A., & Houde, M. (2021), “Evidence of a shared spectro-temporal law between sources of repeating fast radio bursts”. MNRAS, 507, 1, pp. 246-260. DOI:[10.1093/mnras/stab2070](https://doi.org/10.1093/mnras/stab2070).
4. Wyenberg, C. M., Lankhaar, B., Rajabi, F., **Chamma, M. A.**, & Houde, M. (2021), “Generalization of the Menegozzi and Lamb maser algorithm to the transient superradiance regime”. MNRAS, 507, 3, pp. 4464-4480. DOI:[10.1093/mnras/stab2222](https://doi.org/10.1093/mnras/stab2222).
5. Houde, M., Lankhaar, B., Rajabi, F., & **Chamma, M. A.** (2022), “The generation and transformation of polarization signals in molecular lines through collective anisotropic resonant scattering”. MNRAS, 511, 1, pp. 295-315. DOI:[10.1093/mnras/stab3806](https://doi.org/10.1093/mnras/stab3806).
6. Wyenberg, C., Rajabi, F., **Chamma, M. A.**, Kumar, A., & Houde, M. (2022), “Transient Structure in the Non-linear Superradiance Regime of Widely Doppler Broadened Media”. arXiv e-prints, arXiv:[2208.01523](https://arxiv.org/abs/2208.01523).
7. **Chamma, M. A.**, Rajabi, F., Kumar, A., & Houde, M. (2022) “A broad survey of spectro-temporal properties from FRB 20121102A”. Submitted to MNRAS.

Contents

Abstract	iii
Summary for General Audience	iv
Dedication	v
Acknowledgements	vii
Co-Authorship Statement	ix
List of Publications	x
List of Figures	xiv
List of Tables	xv
1 Introduction	1
1.1 Propagation of Radio Signals through Space	3
1.1.1 Dispersion	3
1.1.2 Scattering and Scintillation	7
1.1.3 Faraday Rotation	10
1.2 Discovery and History of Fast Radio Bursts	11
1.2.1 FRBs as a New Population of Astrophysical Signals	12
1.2.2 A Repeating FRB Source: FRB20121102A	17
1.2.3 The Wide Field Era of FRBs	23

1.3	Theories of Origin	27
1.3.1	Observational Constraints	28
	Spectro-Temporal Properties	28
	Polarization and Rotation Measure	29
	Activity and Periodicity	30
	Environments	32
1.3.2	Magnetars and other compact progenitors	33
1.3.3	Coherent Emission Mechanisms	36
	Curvature Emission by Bunches	37
	Synchrotron Masers and Relativistic Shocks	38
	Dicke’s Superradiance	39
1.3.4	Triggered Relativistic Dynamical Model	41
1.4	This Thesis	45
2	A simple relationship for the spectro-temporal structure of bursts from FRB 20121102A	57
2.1	Observational evidence for the triggered relativistic dynamical model	57
2.1.1	Predictions made by the model – FRB 20121102A	58
	Sub-burst duration vs. frequency of observation	60
	Sub-burst drift vs. sub-burst duration	61
	Relative drift between sub-bursts – the sad trombone	65
2.2	Discussion and summary	67
3	Evidence of a shared spectro-temporal law between sources of repeating fast radio bursts	73
3.1	Introduction	73
3.1.1	The triggered dynamical model of Rajabi et al. (2020)	76
3.2	Burst Analysis	78

3.2.1	The effect of the Dispersion Measure (DM)	79
3.2.2	Measurement exclusions and fitting	82
3.3	Results and Discussion	83
3.3.1	Unresolved bursts and slope vs. drift rate ambiguity	89
3.3.2	DM variations as a rotation of the autocorrelation function	92
3.3.3	Uncertainty due to frequency band masking	93
3.3.4	The narrow-band nature of the emission process	95
3.4	Conclusion	96
	Appendices	104
2.A	Autocorrelation Analysis	104
2.B	Determination of β^+ , ν_0 and $\Delta\beta'$	106
4	A broad survey of spectro-temporal properties from FRB 20121102A	114
4.1	Introduction	114
4.2	Burst Sampling	117
4.3	Methods and Analysis	119
4.4	Results	126
4.4.1	Spectro-temporal Properties	128
4.5	Discussion	138
4.5.1	Drift rate vs duration and frequency	142
4.5.2	Bandwidth vs. Sub-burst Duration relationship	143
4.5.3	Spectro-temporal properties and their relationship to the emission process	144
4.6	Conclusions	146
5	Summary and Conclusions	153
	Curriculum Vitae	159

List of Figures

1.1	The Lorimer Burst	6
1.2	Schematic of a scatter-broadened image	8
1.3	Waterfall of FRB110220, with insets showing interstellar scattering tails	9
1.4	Four FRB detections from Thornton et al. (2013)	18
1.5	Phase diagram of radio transients showing luminosity versus duration	26
1.6	Schematic of an FRB in the triggered relativistic dynamical model	43
1.7	Time sequence of an FRB in the triggered relativistic dynamical model	43
2.1	Burst 11A detected from FRB 20121102A by Gajjar et al. (2018)	59
2.2	Dynamic spectra of Bursts #2 and #3 from Michilli et al. (2018) with their two-dimensional autocorrelation functions	62
2.3	A plot of $ d\nu_{\text{obs}}/dt_{\text{D}} $ vs. t_{w} on logarithmic scales for a sample of sub-bursts from FRB20121102A	64
3.1	Sub-burst Slope vs Sub-burst Duration	85
3.2	Effect of Dispersion Measure (DM) on FRB waterfalls	86
3.3	Effect of DM on angle used to find drift	90
3.4	Artificial waterfall with noise for studying the effect of noise on measurement	94
3.5	Sub-burst Slope normalized by ν^2 vs frequency to explore narrow-band nature of the emission process	97
3.6	Bursts from FRB20121102A and their measurements	99
3.7	More bursts from FRB20121102A and their measurements	100
3.8	Bursts from FRB20180916B and their measurements	101

3.9	Bursts from FRB20180814A and their measurements	102
3.10	Burst #180917 from FRB20180814A, its components, and their measurements	103
4.1	Histograms of the properties of sub-bursts sampled from FRB20121102A for the survey of spectro-temporal features	120
4.2	Example measurement of burst B006 from Aggarwal et al. (2021)	125
4.3	The relationship between the sub-burst slope and sub-burst duration of surveyed bursts	128
4.4	Relationships of burst properties with burst frequency	131
4.5	Relationships between the sad trombone drift rate and burst duration and frequency	132
4.6	Relationships between the burst bandwidth and frequency, duration, and sub-burst slope	135
4.7	Search for correlations between measured spectro-temporal properties of bursts from Li et al. (2021) and their wait-times and energies	137

List of Tables

1.1	Measured properties of a RRAT, a Giant Pulse, and an FRB	14
3.1	Range of DMs used for obtaining measurements of spectro-temporal features of bursts from FRB20121102A, FRB20180916B, and FRB20180814A	80
4.1	Results from the measurement exclusion and DM optimization process used for the survey of spectro-temporal features	127
4.2	Summary of fits found and resulting values	129

Chapter 1

Introduction

The night sky is filled with diverse phenomena and their study over the last several decades has led astronomers far outside of the visible range of electromagnetic radiation, resulting in discoveries not only in the low radio frequencies or the high energy realms of gamma and X-ray astronomy, but also to the discovery of transient events, both long and short. These transient phenomena, such as supernovae which can last months or decades, often originate from highly energetic and cataclysmic events around environments that challenge and push our understanding of physics in order to explain them.

The discovery of pulsars and their short, periodic, radio emission (Hewish et al. [1968](#)) began a decades long process of improvements in observational methods and technology in an effort to understand the emission mechanism of pulsars along with their source, neutron stars, in increasingly better detail. These improvements enabled the discovery and study of a variety of short radio transients that seemed distinct from pulsar emission, either through their lack of periodicity or their variable intensities. Of these short radio transients, Fast Radio Bursts (FRBs) are a population recently discovered that distinguishes itself from other radio transients by being extremely energetic, extremely short, and by coming from distances that reach out to galaxies far beyond our own. FRBs are also notable for having no known counterpart in other bands of the electromagnetic

spectrum, including optical, X-ray, and gamma rays.

The origin of FRBs remains unknown, and in the last few years activity on this topic has increased dramatically with the development of radio telescopes with large fields of view, such as the CHIME radio telescope, that allow for FRB searches covering huge swaths of the sky. This has led to a several-fold increase in the number of observed FRBs and sources of FRBs, and a wealth of intriguing clues and new questions arise from this influx of data. Their common occurrence and extragalactic nature makes them promising candidates for probing cosmological parameters of the universe and the material between galaxies.

This thesis will explore the features of FRBs, the relationships we discovered between them, and the implications these relationships have on the origin of FRBs. It is structured in the following way. This chapter serves as an introduction to the topic of FRBs, and will discuss the propagation of radio signals through space, the discovery of FRBs, the observational characteristics of FRBs, the types of FRB sources and the environments they have been localized to, and theories of the origin and emission mechanism of FRBs. Chapter 2 will use the predictions of a simple relativistic model for the properties of FRBs and present an analysis of bursts from a repeating FRB source. Chapter 3 will describe a relationship between the duration and frequency vs time evolution of FRBs that is shared between multiple sources of FRBs located in different galaxies. Chapter 4 will survey the spectro-temporal features (ie. the features seen in the spectra and time data of an FRB) of many bursts from a single repeating FRB source named FRB20121102A, for which a wealth of data exists. These studies reveal previously unknown relationships in the features of FRBs and open up new avenues for investigation.

1.1 Propagation of Radio Signals through Space

The interstellar and intergalactic medium (ISM and IGM, respectively) leave several marks on radio signals as they propagate from their source to the observer that affect the durations of the signals measured as well as their intensities. This means that accounting for propagation effects is essential for acquiring accurate measurements of a signal and for even finding the signal in the first place. These effects include dispersion, caused by free electrons and ions along the line of sight which affects the arrival time of a signal based on its frequency, scintillation, caused by irregularities in the propagating medium which results in frequency dependent intensity fluctuations and scattering, which affects rays as they travel through irregularities in the medium and results in a long exponential tail in the shape of a pulse. Other effects such as Faraday rotation and conversion can affect the polarization properties of a signal. Here we describe these propagation effects, possible strategies used to account for them, and their implications on interpreting observations.

1.1.1 Dispersion

Dispersion is the result of a wavelength-dependent refractive index, and hence differing propagation speeds, radio frequencies have when passing through an ionized medium. This phenomenon is analogous to the dispersion of light by a prism. Electromagnetic waves propagating in a cold plasma with no magnetic field present obey the dispersion relation

$$\omega^2 = \omega_p^2 + c^2 k^2, \quad (1.1)$$

where ω is the angular frequency of the wave, k the wavenumber, c the speed of light, and $\omega_p = \sqrt{n_e e^2 / \epsilon_0 m_e}$ is the angular plasma frequency, written in terms of the electron density n_e , electron charge e , electron mass m_e and permittivity of free space ϵ_0 . This dispersion relation can be used to find the group velocity of a propagating signal, ie. the velocity of its envelope, or that of a pulse of radiation when travelling through a medium.

Using the dispersion relation the group velocity is given by

$$\frac{d\omega}{dk} = c\sqrt{1 - \left(\frac{\omega_p}{\omega}\right)^2}. \quad (1.2)$$

In a vacuum the group velocity is simply c , so we see the extra factor of $\sqrt{1 - (\omega_p/\omega)^2}$, which is the refractive index, introducing a dependence on the frequency. For cold plasmas such as the ones that make up the ISM and IGM, waves of frequency $\omega < \omega_p$ have imaginary wave numbers k , and therefore are attenuated by the plasma and do not propagate. This means any signal we hope to detect should in principle be greater than the plasma frequency. For example, in the ISM the electron number density is about $n_e \simeq 0.03 \text{ cm}^{-3}$ (Lorimer and Kramer 2012), which corresponds to a plasma frequency of 1.5 kHz that is much lower than the frequencies transmitted by the atmosphere.

Because of the frequency dependent group velocity, a radio signal that travels a length d to the earth will be delayed in time by an amount that is also frequency dependent, given by

$$\begin{aligned} t &= \left(\int_0^d \frac{d\ell}{d\omega/dk} \right) - \frac{d}{c} \\ &= \frac{e^2}{8\pi^2\epsilon_0 m_e} \frac{\int_0^d n_e d\ell}{\nu^2}, \end{aligned} \quad (1.3)$$

whenever $\omega_p \ll \omega$ and $\nu = \omega/2\pi$. The integral in equation (1.3) is used to define the dispersion measure (DM)

$$\text{DM} = \int_0^d n_e d\ell, \quad (1.4)$$

and is observationally used as a measure of the amount of dispersion a signal experiences. Thus, given signals from a single event at two frequencies ν_1 and ν_2 travelling through the same medium, the delay time between them due to dispersion is given by

$$\Delta t \approx 4.1488 \times 10^6 \frac{\text{DM}}{\nu_1^2 - \nu_2^2} \text{ ms}, \quad (1.5)$$

where the constant in front is called the dispersive constant $\mathcal{D} \equiv e^2/8\pi^2\epsilon_0 m_e$, and its value in equation (1.5) is written in the cgs unit system with units pc/cm^3 , and ν_1 and ν_2 are in MHz (Lorimer and Kramer 2012). With a model of the electron distribution n_e , the distance to a source can be estimated and the observed DM can serve as an approximate proxy for the distance. Figure 1.1 shows a frequency versus time plot (also called a waterfall) of the first fast radio burst discovered, and shows a large delay between the high and low frequency channels of the signal that follow a ν^{-2} dependence with the frequency, as expected from dispersion by a cold plasma.

There are two main strategies for compensating for the effects of dispersion, the first and simplest is called incoherent dedispersion which takes advantage of the time delays computed from equation (1.5) and the other is coherent dedispersion, which allows for the complete removal of the effects of dispersion at much greater time resolution. With the understanding that dispersion results in a time delay to the arrival time of different frequencies of a signal, the effects of dispersion can be compensated for to obtain the signal as it was before propagation to the observer. If a signal is split into separate frequency channels via a spectrometer, then equation (1.5) can be used to compute the time delay that needs to be applied to each channel such that all signals arrive at the same time (Lorimer and Kramer 2012). Incoherent dedispersion can be performed immediately with hardware at the telescope or more commonly through software after the data have been collected. However, the frequency resolution limits the precision in time that data can be shifted since any frequency channel will have its own smaller dispersive delay between the top and bottom of the channel that cannot be corrected for, limiting the time resolution that can be obtained (Lorimer and Kramer 2012).

Coherent dedispersion avoids this issue and is a more data-intensive process that is built on the understanding that dispersion of a signal from the propagating medium affects only the phase of the electromagnetic wave (Hankins and Rickett 1975). Incoming electromagnetic radiation induces a time varying voltage in the receiver of a telescope

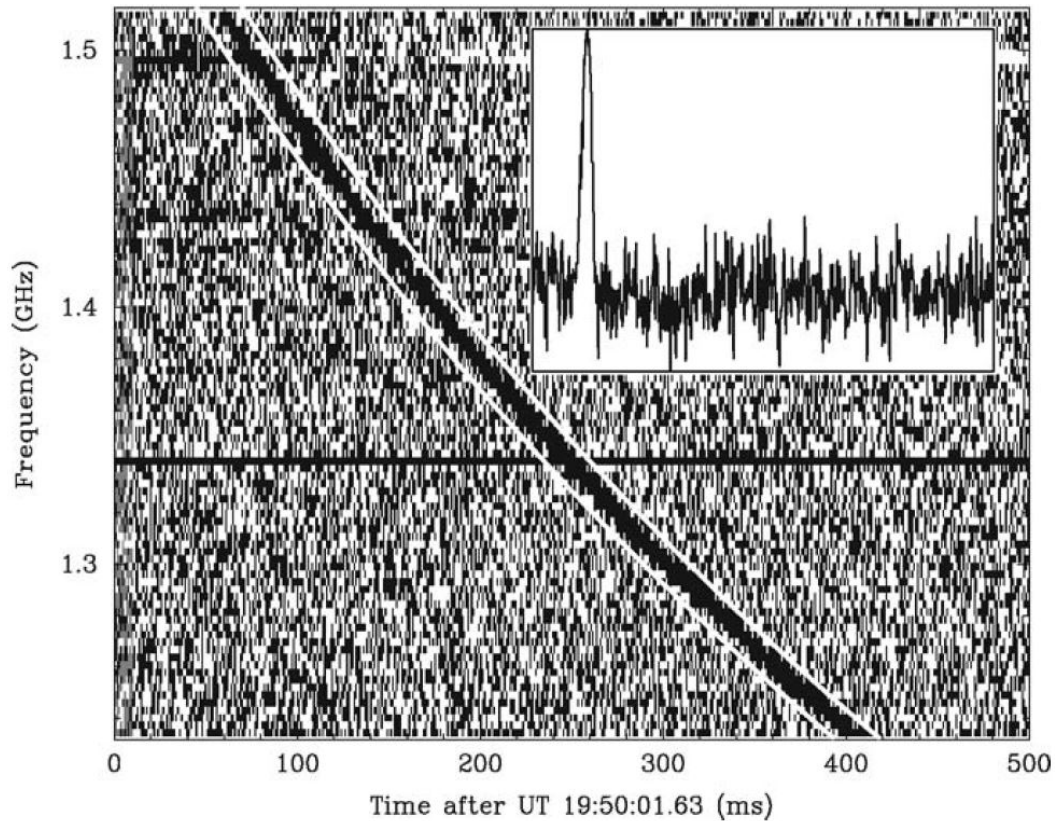


Figure 1.1: Frequency versus time plot, or waterfall, of the first fast radio burst discovered, found in 2007 from archival data collected on 24 August 2001 (Lorimer et al. 2007). This data is dispersed, meaning the signal at lower frequencies arrived delayed by a time proportional to ν^{-2} due to the propagation properties of radio signals in the cold plasma of the interstellar medium. The dispersion measure (DM) of this burst was found to be 375 pc/cm^3 , and is indicated by the white lines bounding the burst showing the theoretical behaviour for dispersion by a cold plasma (see equations 1.3 and 1.5). The inset panel shows the total power signal integrated after dedispersion to a DM of 375 pc/cm^3 . Though the width of the pulse is just a dozen or so milliseconds, the dispersive delay spreads the signal over hundreds of milliseconds. Figure from Lorimer et al. (2007), reprinted with permission from AAAS.

that can be sampled and digitised to not only measure the voltage information but also the phase of the electromagnetic wave. By using the observed DM of a source, which can be inferred from the simpler incoherent dedispersion process, for example, the phase transformation caused by dispersion in the ISM (or IGM) can be calculated and used to reverse the effects of dispersion when applied to the phase information obtained from the voltage data of the telescope. This restores the intrinsic signal as it was when emitted and is not limited by the width of the frequency channels, which allows for a signal to be dedispersed at the time resolution of the telescope. In practice, the time resolution is greatly limited by the frequency resolution when incoherently dedispersing and results in a lower time resolution than that provided by the instrument, and coherent dedispersion therefore allows for the dedispersion of pulses at much higher time resolution (Lorimer and Kramer 2012).

1.1.2 Scattering and Scintillation

A signal travelling along the line of sight will encounter clumps and inhomogeneities with different refractive indices that each distort the wavefront of a signal. Since the refractive index is dependent on the frequency, an observer will therefore see a spatially incoherent wavefront and an interference pattern formed by rays of differing frequencies that have been bent and delayed, resulting in the observation of pulse broadening due to scattering and intensity variations called scintillation (Lorimer and Kramer 2012; Petroff, Hessels, and Lorimer 2019). The scattering and diffraction of rays as they pass through inhomogeneities broadens the image of the source and delays the arrival time of rays. Figure 1.2 shows a schematic of such a scatter broadened image.

Lorimer and Kramer (2012) shows that the observed intensity of a pulse as a function of time after scattering can be written as

$$I(\Delta t) \propto e^{-\Delta t/\tau_s}, \quad (1.6)$$

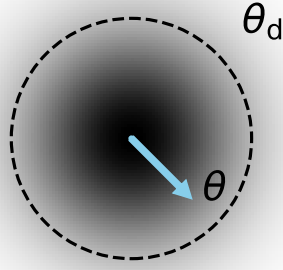


Figure 1.2: Schematic of a scatter-broadened image with angular radius θ_d . Rays at an angular distance θ have been bent and delayed by inhomogeneities in the medium they propagate through. The angular intensity distribution is shown by the fuzzy patch and is Gaussian in nature (Lorimer and Kramer 2012).

where $\Delta t = \theta^2 d/c$ is the geometric time delay as a function of the angle θ of the ray observed (see Figure 1.2) and τ_s is the scattering timescale, and is proportional to

$$\tau_s = \frac{\theta_d^2 d}{c} \propto d^2 \nu^{-4}, \quad (1.7)$$

where θ_d is the angular size of the scattered disk, d is the distance to the source, c is the speed of light and ν is the observing frequency. This means that scattering results in broadened intensity profile with a long exponential tail and with greater scattering (and a larger scattered image), a longer tail (Lorimer and Kramer 2012). The ν^{-4} dependence in τ_s indicates that signals at a higher frequency from the same source will have shorter tails. As an example, Figure 1.3 shows a waterfall of FRB110220 reported by Thornton et al. (2013) with three slices of time series data at 1494 MHz, 1369 MHz, and 1219 MHz in the inset panel that show the exponential tail expected from interstellar scattering, with shorter and shorter tails with increasing frequency. Modelling of this frequency dependent pulse broadening as well as the dispersive delay allow a determination of the distance of the source and indicate an extragalactic origin, as well as the presence of an

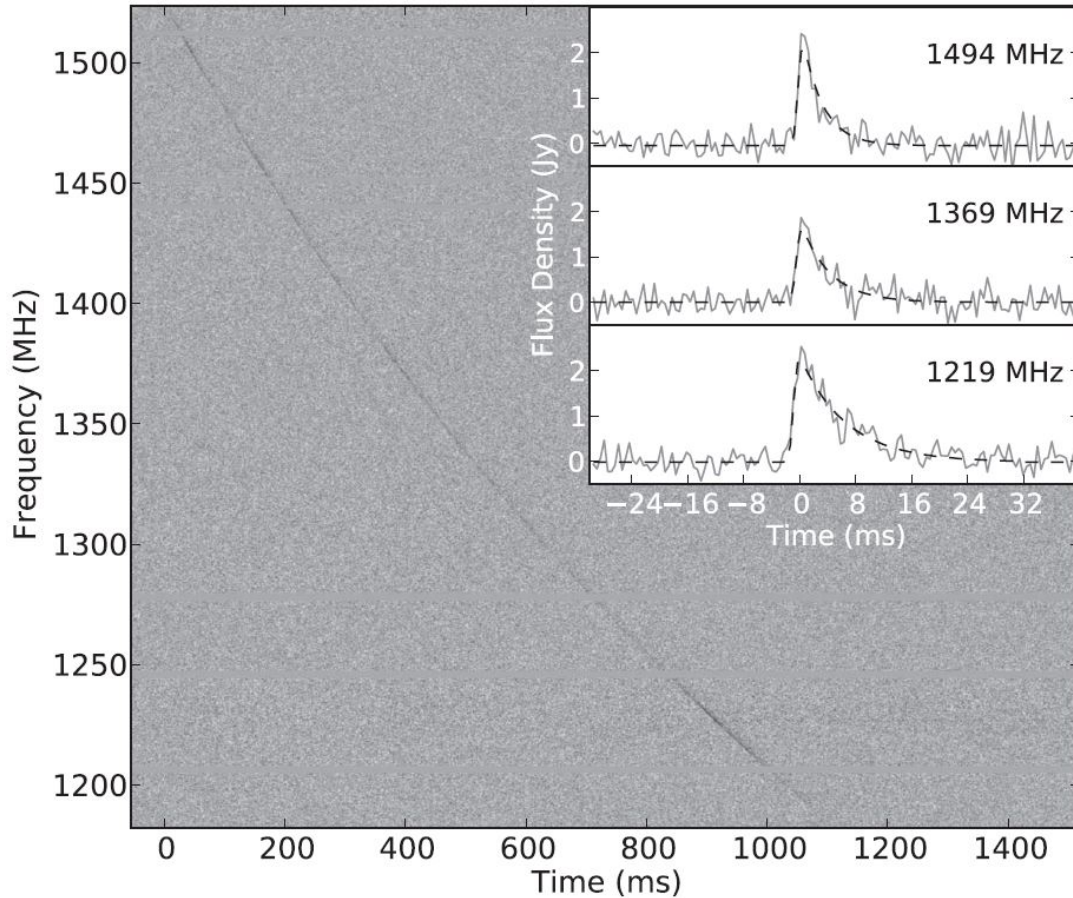


Figure 1.3: Waterfall of FRB110220 (Thornton et al. 2013) showing a long dispersive delay, and, inset, slices of time series data at 1494, 1369, and 1219 MHz showing broadened pulses with exponential tails expected from interstellar scattering due to propagation through a cold plasma. The tails are shorter with increasing frequency as expected from equation (1.7). Figure from Thornton et al. (2013), reprinted with permission from AAAS.

intervening cold plasma (Thornton et al. 2013).

The interference pattern of bright and dark spots formed by the distortion of a signal as it propagates evolves in time due to relative motions between the source, intervening material and observer and is the cause of the intensity variations and ‘twinkling’ called scintillation (Lorimer and Kramer 2012). For waves of differing frequencies to interfere in an observable way, they must be of similar frequency. Lorimer and Kramer (2012) shows that for a signal at frequency ν , there is a range of frequencies $\Delta\nu$ that contributes to

scintillation called the scintillation bandwidth given by

$$\Delta\nu \propto 1/\tau_s \propto d^{-2}\nu^4, \quad (1.8)$$

where τ_s is the scattering timescale defined in equation (1.7). This implies that scintillation results in intensity variations that can be seen both as functions of time and frequency, and complicated spectral structures in a signal can either be caused by the emission mechanism of the signal or simply due to the intervening medium and can complicate analysis (Lorimer and Kramer 2012; Petroff, Hessels, and Lorimer 2019). An example of such spectral intensity variations can be seen in the waterfall shown in Figure 1.3 (though not necessarily all due to scintillation). The cold plasma of the ISM and IGM that a signal propagates through before being observed greatly affects the structure and intensity signal observed, both in frequency and in time.

1.1.3 Faraday Rotation

The motion of charges in a cold plasma generates a magnetic field whose component along the line of sight B_{\parallel} affects the polarization properties of a radio signal as it propagates through it. Any electromagnetic wave can be written as a sum of its left-circularly- and right-circularly polarized components. The propagation speeds for the left- and right-handed polarizations differ very slightly in the presence of a magnetic field, resulting in a small frequency-dependent phase difference between the two components as the wave travels a distance d through such a medium. While B_{\parallel} negligibly affects the group velocity, it does affect the measured linear polarisation angle Ψ (Lorimer and Kramer 2012). Using the refractive indices in a cold magnetized plasma for the left- and right-circularly polarized components, it can be shown that a signal travelling a distance d through a cold magnetized plasma experiences a change in position angle $\Delta\Psi$ due to the

line-of-sight magnetic field B_{\parallel} given by (in cgs units)

$$\Delta\Psi = \lambda^2 \frac{e^3}{2\pi m_e^2 c^4} \int_0^d n_e B_{\parallel} d\ell, \quad (1.9)$$

where λ is the wavelength of radiation (Jackson 1975; Lorimer and Kramer 2012). The integral in the above expression is used to define the rotation measure (RM)

$$\text{RM} = \frac{e^3}{2\pi m_e^2 c^4} \int_0^d n_e B_{\parallel} d\ell. \quad (1.10)$$

The RM has units of rad/m^2 and can be determined observationally through measurements of the linear polarization angle at different wavelengths and then fitting to the form $\Delta\Psi = \text{RM} \times \lambda^2$, although other methods exist that are more practical (see Sec 7.4.3.2 of Lorimer and Kramer 2012). The RM can be used as a probe of the line of sight component of the magnetic field and also to reverse its effects on the linear polarization angle, enabling studies of the source signal's polarization when it was emitted.

Awareness of propagation effects like dispersion, scattering, scintillation, and Faraday rotation aids in the interpretation of FRB features, and can make it possible to differentiate features due to the emission of the FRB from features due to the intervening plasma in the ISM and IGM. Both topics are active areas of research with interesting questions, and decoupling the effects of one from the other allows investigation into these fields.

1.2 Discovery and History of Fast Radio Bursts

Despite their brightness, FRBs required significant advancements in technology and observational strategy to be discovered. With the discovery of pulsars in 1968 (Hewish et al. 1968), techniques that relied on the fundamental periodicity of the pulsar emission to increase signal-to-noise (S/N) quickly gained popularity and single pulse searches decreased despite their scientific value since the periodic methods greatly increased the sensitivity

of pulsar searches (Burns and Clark 1969; Nice 1999; Lorimer and Kramer 2012; Petroff, Hessels, and Lorimer 2019). These techniques were less effective for very short period pulsars and pulsars that had pulse-to-pulse variations in their intensity (Nice 1999). In addition, some pulsars occasionally exhibit bright single pulses called “Giant Pulses” such as the Crab pulsar, and these potentially could be used to search for extragalactic pulsars due to their high intensity (Hankins et al. 2003; McLaughlin and Cordes 2003).

To the end of performing single pulse searches Cordes and McLaughlin (2003) described issues related to the search for fast radio transients, and pointed out the necessity for telescopes with wider fields of view in order to capture sources of single pulses that cannot be tracked. They also described methods such as matched filtering where single pulses are searched for by convolving de-dispersed data with pulses of a trial width to increase the signal-to-noise ratio. These methods bore fruit when a single pulse search by Lorimer et al. (2007) in archival data of the Parkes radio telescope in Australia yielded a 5 ms burst with enormous brightness and a DM that implied an extragalactic origin. This section will describe the discovery of the first FRB, the subsequent questioning of the validity of this detection, how it became clear FRBs were a real distinct population of extragalactic signals, and the developments that followed including the discovery of repeating sources of FRBs, a sharp increase in the number of FRB detections in recent years, and the varying and often confusing observed characteristics of FRBs.

1.2.1 FRBs as a New Population of Astrophysical Signals

The first FRB was discovered in a single pulse search of archival pulsar survey data at 1.4 GHz of the Magellanic Clouds using the Parkes telescope, and was differentiated from other short radio transients by its large energy output, high dispersion, and singular, isolated, occurrence (Lorimer et al. 2007). Pulsar surveys lend themselves well to single pulse searches and had been used in the earlier discovery of a short periodic radio transient called rotating radio transients (RRATs) by McLaughlin et al. (2006). RRATs are

characterized by short, bright bursts with durations of a few milliseconds and repeating with periods on the orders of seconds. The highest flux density observed in the sample discovered by McLaughlin et al. (2006) was 3.6 Jy^1 and their burst amplitude distributions had power-law tails similar to distributions in burst amplitude from Giant Pulses seen from pulsars, leading to the conclusion that RRATs were emitted from a previously unseen population of neutron stars in the galaxy that emit through a mechanism different from pulsars (McLaughlin et al. 2006). Giant Pulses had been observed at higher spectral densities, but much lower DM implying a much closer source.

The detection of the first FRB (shown in Figure 1.1) at Parkes was seen with a flux of 30 Jy and a DM of 375 pc/cm^3 , found by modelling the ν^{-2} dispersion seen in the burst. This detection was two orders of magnitude greater than the detection threshold of the telescope, and saturated the digitizer of the observing system, indicating that the S/N was much greater than the max S/N ratio resolvable. Despite this, no bursts at lower energies were detected in the survey data used or in follow-up observations, suggesting that the burst amplitude distribution of this new burst type followed a different type of distribution from RRATs and Giant Pulses (Lorimer et al. 2007).

By modelling the electron distribution along the line of sight the measured DM can be used to estimate the distance to the source (see equation (1.4)). The contribution to the DM from our galaxy is about 100 pc/cm^3 (Cordes and Lazio 2002; Inoue 2004; Lorimer et al. 2007), while at greater distances the DM increases with redshift. This burst's DM corresponds to a redshift $z < 1$ (Ioka 2003; Inoue 2004). Assuming the source is embedded in a host galaxy, the contribution to the DM from that host is assumed to be similar to the contribution of our own (Lorimer et al. 2007). These consideration and large uncertainties lead Lorimer et al. (2007) to estimate the distance of the source to be about 500 Mpc^2 or $z \sim 0.12$, far beyond the edges of the Local Group of galaxies, which

¹The Jansky (Jy) is a non-SI unit of spectral flux density used in radio astronomy and is equivalent to $1 \text{ Jy} = 10^{-26} \text{ W}/(\text{m}^2\text{Hz})$.

²A parsec is a unit of distance in astronomy and $1 \text{ parsec (pc)} = 3.26 \text{ light-years (ly)} = 3.086 \times 10^{16} \text{ m}$

	d_L (kpc)	S_ν (Jy)	$\Delta\nu$ (MHz)	W (ms)	z	L_{iso} (W)	E_{iso} (J)	T_B (K)
Brightest RRAT from McLaughlin et al. (2006)	3.6	3.6	250	3	0	$\sim 10^{24}$	$\sim 10^{21}$	$\sim 10^{24}$
Crab Pulsar Giant Pulse (Cordes et al. 2004)	2	2000	0.024	0.13	0	$\sim 10^{22}$	$\sim 10^{18}$	$\sim 10^{30}$
Lorimer Burst/FRB010724 (Lorimer et al. 2007)	500000	30	250	5	0.12	$\sim 10^{35}$	$\sim 10^{33}$	$\sim 10^{35}$

Table 1.1: Measured properties of an example RRAT from the discovery paper by McLaughlin et al. (2006), a Giant Pulse from the Crab Pulsar reported by Cordes et al. (2004), and the first FRB discovered (Lorimer et al. 2007). The observed properties from left to right are the luminosity distance d_L , the flux density S_ν , the signal bandwidth $\Delta\nu$, the burst duration W , and the redshift z . These properties are used to roughly estimate the isotropic equivalent luminosity L_{iso} , the isotropic equivalent energy E_{iso} and the brightness temperature T_B . The isotropic equivalent luminosity assumes the energy of a burst radiates outward in all directions uniformly and is calculated as $L_{\text{iso}} = 4\pi d_L^2 S_\nu \Delta\nu / (1 + z)$ (Petroff, Hessels, and Lorimer 2019). While the assumption of isotropic emission is rarely true for energetic bursts and pulses which are beamed and emitted coherently, L_{iso} still serves as a useful estimate of a source’s luminosity. The high brightness temperatures imply a coherent emission process.

spans around 3 Mpc. By using the area of the sky monitored by the pulsar survey used as well as the assumption that these bursts are isotropic over the sky, the rate of bursts of this energy was estimated to be about 90 per day per Gpc³, which differentiated it from other potential source populations due to its higher implied rate (Lorimer et al. 2007).

Table 1.1 lists the observed properties of a RRAT, Giant Pulse, and this burst, showing differences of several orders of magnitude between the estimated energies released and brightness temperatures³ measured. This burst therefore was unlike any other burst seen to date, due to the distance of its source inferred from its DM, its high flux density, the lack of similar bursts at smaller amplitudes that should have been detectable in survey data or follow-up observations, and the implied rate of occurrence across the entire sky.

No additional FRBs were observed in the years following the discovery of the Lorimer burst. The discovery of pulses dubbed “perrytons” at the Parkes telescope that appeared

³The brightness temperature T_B of a source at frequency ν is the temperature a black body in thermodynamic equilibrium must be held at to emit at the same intensity of the source. Since the emission of a black body follows the Planck spectrum, the brightness temperature of a radio signal can be estimated as $T_B \simeq 10^{36} \text{K} \left(\frac{S_{\text{peak}}}{\text{Jy}} \right) \left(\frac{\nu}{\text{GHz}} \right)^{-2} \left(\frac{W}{\text{ms}} \right)^{-2} \left(\frac{d}{\text{Gpc}} \right)^2$, where S_{peak} is the peak flux density, ν is the frequency, W is the width of the signal, and d is the distance to the source (Lorimer and Kramer 2012; Petroff, Hessels, and Lorimer 2019).

to have dispersive delays similar to but not quite like the Lorimer burst while being clearly of terrestrial origin due to their extreme brightness and mid-morning arrivals raised questions about the extragalactic nature of FRBs (Burke-Spolaor et al. 2011). In a search for bursts with a ν^{-2} dispersive delay in archival data spanning the years 1998-2003, 16 different pulses with durations 30-50 ms were found with an apparent dispersive delay. Each pulse was detected in all thirteen beams of the telescope simultaneously, indicating that the telescope was not pointing at the source at the time of the pulse's arrival (Burke-Spolaor et al. 2011). The pulses exhibited deviations from the cold plasma dispersion law, including a discontinuity seen in one pulse and a variety of poor statistical fits to the dispersive law expected (Burke-Spolaor et al. 2011). In addition, all the pulses were observed during the daytime and based on the intensity observed, had the telescope been pointing at the source the intrinsic flux of the pulse would have been extremely bright (Burke-Spolaor et al. 2011).

These terrestrial indications led to the pulses being named ‘peryttons’ after a mythological elk with wings in order to distinguish the pulses from a known natural phenomenon (Burke-Spolaor et al. 2011). Despite the poor fits and non-astrophysical brightness, the delay times observed were approximately the same delay time observed for the Lorimer burst, implying the same DM and suggesting that the source of the Lorimer burst and these pulses were the same (Burke-Spolaor et al. 2011). It was not until rigorous radio-frequency interference (RFI) monitoring of Parkes spotted emission around 2.4 GHz at the same time as a peryton was their origin understood. Under the right conditions, the opening of a microwave oven while it was still running briefly allows radiation to escape and be detected by the telescope, resulting in the peryton signal (Petroff et al. 2015). The perytons, especially due to their detection at the same telescope as the first FRB and lack of detection at any other radio telescope, highlighted the need for validation of pulse detections to rule out terrestrial sources, especially in the initial stages of FRB study.

After the discovery of multiple extragalactic FRBs by Thornton et al. (2013), evidence that FRBs were a distinct population of short radio transients with extragalactic origins and not due to terrestrial interference grew. This study also coined the term ‘fast radio burts’ and bursts of this type were referred by that name following the discovery of these four bursts, shown in Figure 1.4. The four bursts were detected at four different positions on the sky in data taken by the Parkes telescope as part of the High Time Resolution Universe (HTRU) survey (Keith et al. 2010), which planned to survey the entire southern sky at high frequency and temporal resolution in an effort to discover new pulsars, particularly millisecond pulsars. It had studied 24% of the survey region at the time of this discovery (Thornton et al. 2013).

As shown in Figure 1.4, the four FRBs lasted approximately a dozen milliseconds. Three of the FRBs had relatively low S/N, but FRB110220 was bright enough to show an exponential tail in its profile characteristic of interstellar scattering by cold plasma. As discussed in Section 1.1.2, Figure 1.3 shows the waterfall of FRB110220 where the dispersive delay of the burst across almost an entire second can be seen and the frequency-dependant scattering tail can be seen in the inset. Thornton et al. (2013) modeled the dispersion and scattering observed and found a frequency dependence of $\nu^{-2.003 \pm 0.006}$ for the delay time and a frequency dependence of $\nu^{-4.0 \pm 0.4}$ for the width of the pulse, as expected for dispersion and scattering by a cold plasma (Section 1.1). The DMs of the four FRBs found ranged from 553 to 1103 pc/cm³ and were found at high galactic latitudes with diffuse galactic material, implying only a small contribution to these high DMs by galactic material (Thornton et al. 2013; Cordes and Lazio 2002). By using assumptions about the electron and ion content of possible host galaxies based on our own Milky way and the line-of-sight probability of viewing an FRB source through a dense part of its host galaxy, Thornton et al. (2013) argue that the contribution to the DM from a host galaxy is much smaller than the contribution due to the IGM. The high DMs therefore imply enormous distances to the sources of the FRBs ranging from 1.7 to

3.2 Gpc.

These bursts also helped distinguish FRBs from terrestrial sources such as perytons, since the DMs of the perytons peaked at much lower values, had longer durations, and followed the dispersion and scattering laws by plasma much more poorly (Thornton et al. 2013). The expected event rate implied by these detections is found by dividing the number of bursts by the fraction of the sky and amount of time surveyed, yielding about 10,000 bursts per day across the sky, and consistent with the rate implied by the Lorimer burst when assuming an intrinsic luminosity to the source (Thornton et al. 2013). The discovery of these 4 bursts with their high DMs and precise adherence to the dispersive and scattering laws in a cold plasma clearly indicated a population of fast radio bursts with extragalactic origin.

1.2.2 A Repeating FRB Source: FRB20121102A

A pulsar survey at the Arecibo telescope yielded the detection of FRB20121102A⁴, which was the first detection of an FRB by a telescope besides Parkes, and, following extensive follow up observations, was observed emitting ten additional bursts indicating for the first time that sources of FRBs could repeat (Spitler et al. 2014, 2016).

The Pulsar Arecibo L-band Feed Array (PALFA) survey was a long term survey searching for pulsars in the galactic plane at 1.4 GHz with a bandwidth of 0.3 GHz (Cordes et al. 2006). Spitler et al. (2014) performed a single pulse search of PALFA data from March 2009 to December 2012 by dedispersing raw data to ~ 5000 trial DMs ranging from 0 to 2038 pc/cm³ and applying a matched filtering algorithm to each dedispersed time series. This search yielded a single dispersed pulse on November 2, 2012 with a DM of 557.4 pc/cm³, a duration of 3 ms, a flux density of 0.4 Jy, and a dispersive delay that followed a $\nu^{-2.01 \pm 0.005}$ dependence (ie. a dispersive index of -2.01 ± 0.005), consistent

⁴Previously known as FRB121102. The current Transient Name Server (TNS) FRB naming convention is FRBYYYYMMDDA using the day of discovery and an appended letter to distinguish multiple FRB discoveries in a single day. The previous naming convention followed FRBYMMDD+(sky coordinates) and was recently replaced.

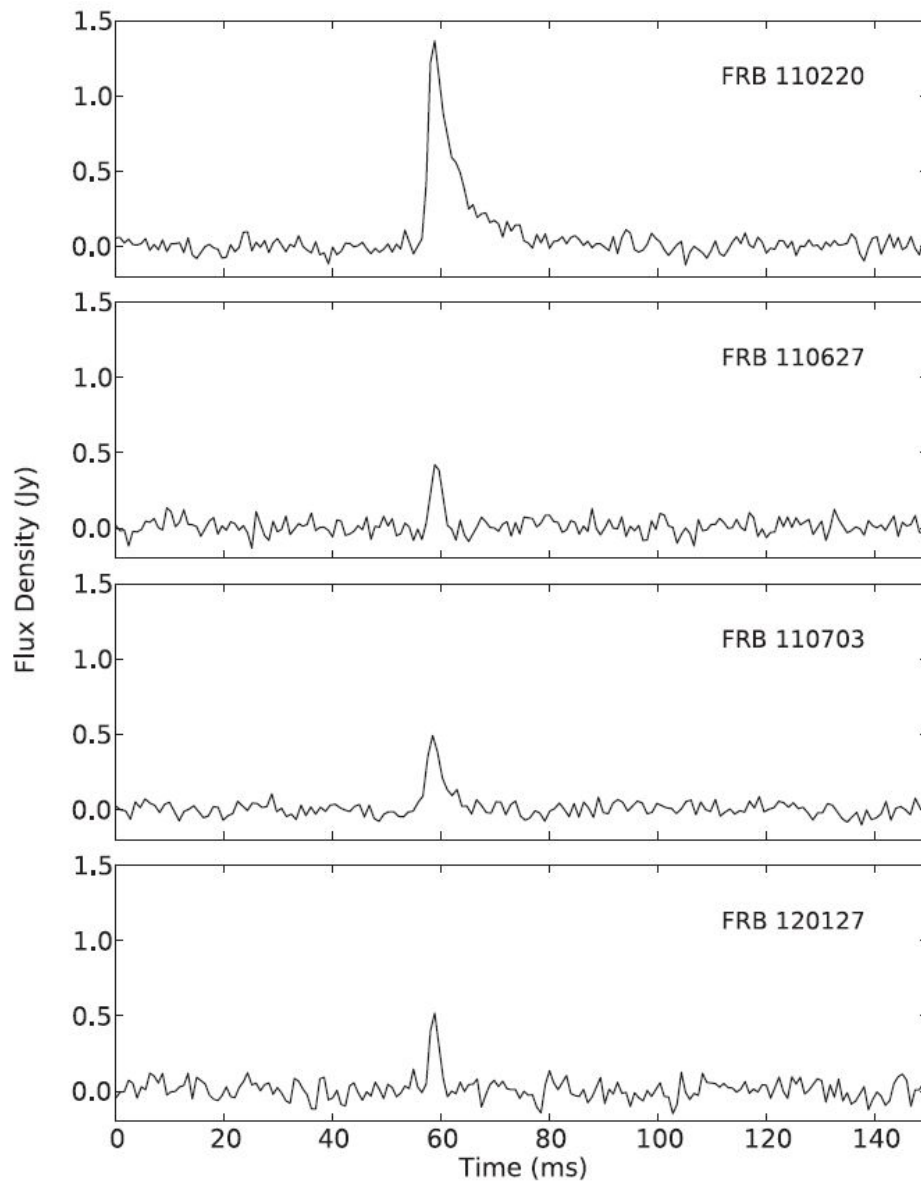


Figure 1.4: The frequency integrated flux densities of the four FRBs found by Thornton et al. (2013) in Parkes data taken as part of the High Time Resolution Universe survey (Keith et al. 2010). FRB110220 shows an exponential tail characteristic of interstellar scattering by a cold plasma (Section 1.1.2) and its waterfall is shown in Figure 1.3. Figure from Thornton et al. (2013) reprinted with permission from AAAS.

with propagation through a plasma (Spitler et al. 2014). Observations of the source two days after the burst and in 2013 revealed no additional bursts at the DM of the first burst (Spitler et al. 2014). Because the search occurred on the galactic plane, the DM contribution from the Milky Way is greater, however the predicted contribution along the line of sight where FRB20121102A was discovered is only 188 pc/cm^3 and cannot account for the observed value of 557.4 pc/cm^3 (Cordes and Lazio 2002; Spitler et al. 2014).

Extensive follow-up observations of the source and the area around it were undertaken with Arecibo from May to June 2015, and ten additional bursts were found over this period (Spitler et al. 2016). The bursts observed had a dispersive index of 2 indicating propagation through a cold plasma, durations ranging from 2.8 to 8.7 ms and had flux densities ranging from 0.02 to 0.3 Jy (Spitler et al. 2016). The rate of bursts observed was about 3 per hour and the range of flux densities suggest that lower energy bursts are produced as well, though the bursts were seen to cluster in time with periods of differing activity (Spitler et al. 2016).

Of the bursts observed, two had multiple peaks in their profile (Spitler et al. 2016), and such multi-component bursts had been seen once before in a set of five bursts discovered in HTRU data by Champion et al. (2016). The spectra of the bursts seen from FRB20121102A were also highly variable, with some intensities peaking at the lower end of the signal bandwidth and others at the high end (Spitler et al. 2016). Despite extensive follow up of other FRB sources by Parkes, FRB20121102A was the only one thus far seen to repeat, and it was unclear whether this source represented all sources, whether other follow up studies lacked the sensitivity to detect additional bursts, or if this represented a different class of FRBs that were not cataclysmic in nature and thus able to repeat (Spitler et al. 2016; Petroff, Hessels, and Lorimer 2019).

By monitoring the repeating bursts of FRB20121102A with the high angular resolution of radio interferometers, a precise location of FRB20121102A can be determined.

FRB20121102A was localized in this way to a star-forming dwarf galaxy with a persistent radio source. In papers published simultaneously by Chatterjee et al. (2017), Tendulkar et al. (2017), and Marcote et al. (2017), FRB20121102A was observed with the Very Large Array (VLA), the European Very-Long-Baseline-Interferometry (VLBI) network, Arecibo and the Gemini North telescope to obtain information about the source of the FRBs as well as the host galaxy and environment of FRB20121102A.

Radio interferometry is a technique whereby many individual radio dishes distributed over a large geographical area simultaneously observe a single source and, by correlating the signals observed at each of dish, can act as pieces of a single large dish and achieve vastly superior angular resolution than any single dish that can be reasonably constructed.

Chatterjee et al. (2017) searched for bursts from FRB20121102A with the VLA in 83 hours of observations over six months and detected 9 bursts between 2.5 and 3.5 GHz from the same position, with coordinates right ascension $\alpha = 05 \text{ h } 31 \text{ min } 58.70 \text{ s}$ and declination $\delta = +33^\circ 08' 52.5''$, achieving sub-arcsecond precision and three orders of magnitude better precision than Arecibo. Chatterjee et al. (2017) also found a persistent radio source emitting in the continuum (at a broad range of frequencies) within $0.1''$ of the burst position.

Tendulkar et al. (2017) observed the location of FRB20121102A using Gemini North, an optical/infrared telescope, and used the Gemini Multi-Object Spectrograph to obtain a spectrum of the source. They found strong Hydrogen- α , Hydrogen- β and Oxygen emission lines indicating that the source is hosted by a star-forming galaxy. The redshift of the host galaxy based on the change in wavelength of lines in the spectrum was found to be $z = 0.19273 \pm 0.0008$, or a distance of 972 Mpc. In addition, the diameter of the host galaxy inferred from the continuum images was less than 4 kpc, classifying it as a dwarf galaxy (Tendulkar et al. 2017).

In observations with VLBI, Marcote et al. (2017) detected four bursts and a persistent

radio source and resolved their positions to milliarcsecond (mas) precision, finding an overlap between the source of the bursts and the persistent radio source also observed by Chatterjee et al. (2017). The extremely high precision of the VLBI allowed Marcote et al. (2017) to constrain the angular distance between the source of the bursts and the persistent radio to less than 12 mas, or a projected distance of less than 40 pc, strongly suggesting that the two are located together. The repeating nature of FRB20121102A allowed it to be precisely located to a persistent radio source in a star-forming dwarf galaxy, providing invaluable information for understanding the emission mechanism and origin of FRBs.

Continued observations of bursts from FRB20121102A revealed polarization properties and complex time-frequency structures that indicate an extreme and energetic source environment and add additional observational constraints on the emission process. Michilli et al. (2018) observed FRB20121102A with the Arecibo telescope between 4.1 to 4.9 GHz and recorded data with full polarimetric information at a time resolution of 10.24 μ s. Sixteen bursts were detected with durations less than 1 ms including one burst with a duration of less than 30 μ s, and all bursts were 100% linearly polarized with nearly the same position angle Ψ of the electric field vector (Michilli et al. 2018).

The rotation measure (RM; see equations 1.9-1.10) was measured for each burst and the average value was about 10^5 rad/m², whose large magnitude was confirmed in observations taken several months later at the Green Bank Telescope (GBT) (Michilli et al. 2018). The RM is proportional to the integral along the line-of-sight of the free electron and ion density weighted by the line-of-sight component of the magnetic field B_{\parallel} (eq. 1.10). The expected contribution to the RM from the Milky Way and the IGM are both no greater than on the order of 10^2 rad/m² (Oppermann et al. 2015; Akahori, Ryu, and Gaensler 2016), and so the high RM observed is most likely due to a large magnetic field in a compact region around the source of the FRBs (Michilli et al. 2018). The high RM observed for FRB20121102A was also the largest value observed from any other FRB

source and all observed pulsars (Michilli et al. 2018). The ratio between the DM and RM can be used to estimate the density of electrons around the source, leading to a value of $n_e \approx 10^2 \text{cm}^{-3}$, consistent with environments around compact objects such as neutron star or black holes (Michilli et al. 2018). These observations indicate that FRB20121102A is embedded in a highly magnetized and ionized environment.

In observations of FRB20121102A using the GBT, Gajjar et al. (2018) detected 21 bursts above 5.2 GHz for the first time in less than an hour of observations, in the most active period of bursts observed yet. Several of these bursts consisted of multiple components (or sub-bursts), that arrived slightly later the lower in frequency they were, with one burst being composed of at least 4 sub-bursts of widths less than 1 ms long. The bursts again showed 100% linear polarization and a high RM value, confirming the magnetized and ionized environment observed by Michilli et al. (2018).

Hessels et al. (2019) analysed 19 bursts from FRB20121102A observed by Arecibo and GBT in order to study the sub-bursts and time-frequency structures such as those observed by Gajjar et al. (2018). Hessels et al. (2019) found bursts with up to seven sub-bursts, with separations between them on the order of a 1 ms. For each burst, the sub-bursts within a burst had a tendency to drift to lower frequencies at later times (or equivalently, bursts with lower frequencies arrived later), and Hessels et al. (2019) measured this effect quantitatively finding that the drift rate $d\nu/dt$ was always negative and that the drift rate increased linearly with frequency, however the frequency drift within individual subbursts was not studied. The high RM and polarization percentages observed from FRB20121102A indicate a magnetized and extreme environment around the source while the complex time-frequency structures observed in the bursts show unexpected relationships and add constraints on the possible emission mechanism.

1.2.3 The Wide Field Era of FRBs

With the knowledge that FRBs exist as a new population of astrophysical phenomena and the discovery of a single repeating FRB source, many new questions remained to be answered, such as whether there were other source of repeating FRBs, what the true FRB distribution on the sky was, and of course what physical process and environment is able to produce such intense radio signals. The existing radio telescopes had relatively narrow fields of view, and large surveys of the sky necessitated hundreds if not thousands of pointings. This strategy works with pulsars, whose regular periodic and frequency emission enables their discovery with just a short pointing, however with FRBs which are sporadic and unpredictable and only seemed to repeat randomly if at all, these surveys are not well suited for a broad population study of FRBs. Surveys from telescopes with wide fields of view that do not need to be pointed are better suited to this task.

The Canadian Hydrogen Intensity Mapping Experiment (CHIME) commissioned around 2018 along with its dedicated FRB processing backend (named CHIME/FRB) allows for the monitoring and detection of FRBs in realtime across a large field of view of about 200 deg² (CHIME/FRB Collaboration et al. 2018). CHIME is a radio interferometer and consists of four halfpipe reflecting cylinders each with 256 receivers suspended at the focal point of the cylinder, measuring signals in a frequency range of 400-800 MHz. CHIME cannot be pointed, instead it statically observes in the same direction while the rotation of the Earth changes the field in view, thus allowing for a sweep of the sky every day. In the commissioning phase CHIME/FRB expected to see between 2 to 42 FRBs per day across its large field of view, and survey the FRB population, measuring the sky and DM distributions in the process (CHIME/FRB Collaboration et al. 2018).

While still in its commissioning phase, CHIME/FRB detected five bursts from a second repeating FRB source, FRB20180814A⁵ with a DM of 189 pc/cm³ and downward drifting bursts such as those seen in FRB20121102A (Amiri et al. 2019). CHIME requires

⁵Also known as FRB180814.J0422+73 under the old naming convention

recording of its baseband data (raw voltages) in order to localize FRB events to an arcminute precision, but due to the high data rate this recording system was to be commissioned following the initial science phases, and could only approximately localize FRB20180814A to a region of the sky about 0.2° by 2 minutes of right ascension across. However, the DM implies a redshift of less than 0.1 (Amiri et al. 2019; CHIME/FRB Collaboration et al. 2018). This discovery early on in the the life of CHIME was an indication of its ability to study FRBs.

Another important discovery by CHIME/FRB was the discovery of an FRB source that not only repeated, but was periodic. FRB20180916B was discovered via the detection of 38 of its bursts between September 2018 to February 2020, and was also detected by the European VLBI (CHIME/FRB 2020b). To find the period, bursts arrival times were folded from the 500 days of observation onto periods ranging from 1.5 to 100 days. For trial periods that correspond to the true period, if any, bursts will be seen to cluster together whereas an unphysical period will result in bursts uniformly distributed. The amount of deviation from a uniform distribution can be quantified with a statistical quantity called the reduced- χ^2 and a peak period with a large deviation from a uniform distribution is found at 16.35 ± 0.15 days with no other periods deviating as significantly (CHIME/FRB 2020b). Though the source is periodic, its bursts do not arrive regularly, and all of the bursts occur in a 5 day window during the 16.35 day period with half of the bursts arriving in a 0.6 day window (CHIME/FRB 2020b). This discovery added an additional aspect to FRBs and excludes models that lead to purely random bursts.

A burst from a galactic magnetar SGR1935+2154, a highly magnetized neutron star, was detected by CHIME/FRB on 28 April 2020 with an energy release of $\sim 10^{34}$ erg, similar to the energies of an FRB and detectable out to 12 Mpc, marking for the first time an FRB-like burst from our own galaxy, and the brightest ever seen radio signal from any magnetar by three orders of magnitude (CHIME/FRB 2020a). The burst was also detected by Bochenek et al. (2020) using the STARE2 radio array, which allowed for a

precise localization and follow up with telescopes in other wavelengths. Though an intense burst, the luminosity was still less than any other FRB detected as shown in Figure 1.5. The burst consisted of two sub-bursts of less than 1 ms in duration, with the second sub-burst arriving higher in frequency. The burst DM was ~ 332 pc/cm³, much less than the expected contribution from the Milky Way along that line of sight, indicating the galactic origin of the burst (Cordes and Lazio 2002; CHIME/FRB 2020a). SGR1935+2154 was in an active state and was being monitored by high energy telescopes at the time of the burst, allowing the detection of a hard X-ray burst with two peaks at the same time as the radio burst (Mereghetti et al. 2020). While the magnetar was very active in X-rays and gamma rays, the burst detected by CHIME/FRB and STARE2 was the only radio signal of this brightness detected. The detection of X-rays temporally coincident with this candidate FRB marks the first detection of a non-radio counterpart to an FRB. While this detection suggests magnetars can explain some of the FRB population (CHIME/FRB 2020a) it cannot completely explain the highly active and energetic repeating FRBs or FRBs localized to galaxies with low star-formation (Bannister et al. 2019), where magnetars are not expected to be (Kaspi and Beloborodov 2017).

The first CHIME/FRB catalog released included 536 FRBs, which vastly increased the number of known FRBs in one fell swoop (CHIME/FRB Collaboration et al. 2021). The first CHIME/FRB catalog included bursts from one-off events and a total of 18 repeating FRB sources. The sky distribution of non-repeating and repeating sources appear to be uniform across the sky but for the first time showed that the duration and spectral bandwidth between the two populations differed, potentially answering the important question, do all FRBs repeat? (No). Pleunis et al. (2021b) further investigated the morphology of the bursts in the CHIME/FRB catalog showing that non-repeating FRBs cluster with high bandwidths (at 400 MHz, which is the maximum bandwidth of CHIME) while repeating FRBs rarely reached such high bandwidths. Non-repeating FRBs were also shorter in duration, rarely longer than 15 ms, while the duration of

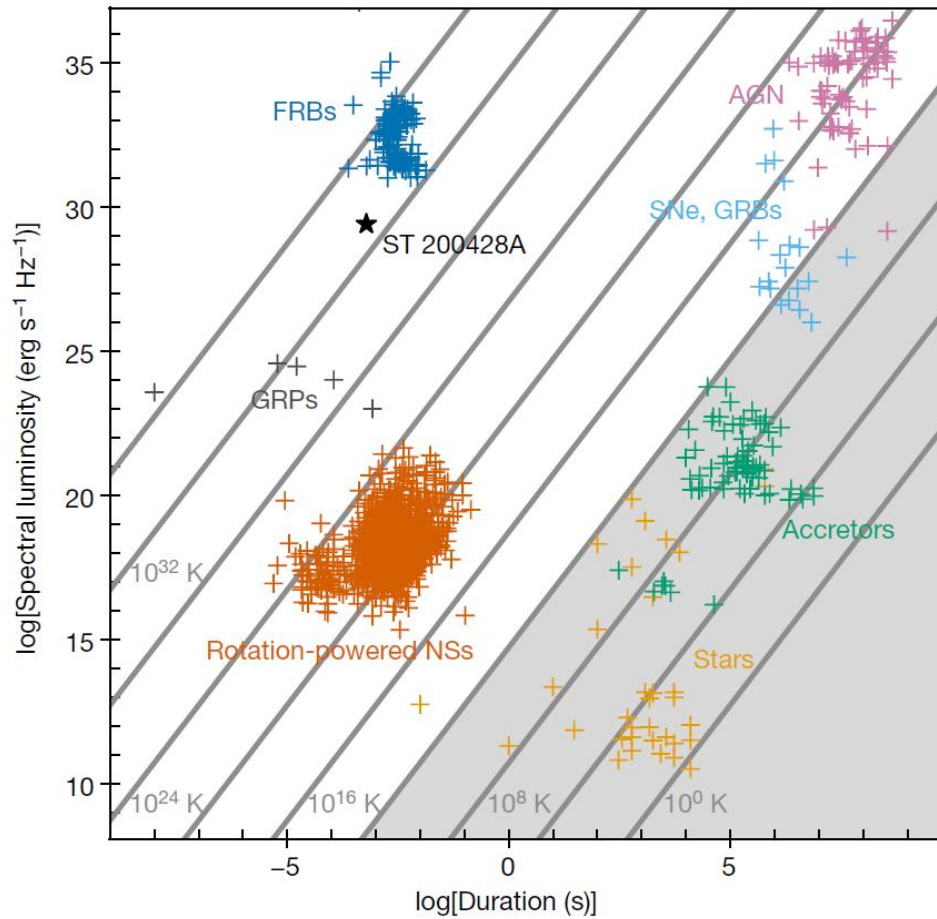


Figure 1.5: Phase diagram of radio transients showing isotropic equivalent spectral luminosities versus transient duration. ‘GRPs’ denote giant radio pulses, ‘Rotation-powered NSs’ refers to RRATs and rotation powered pulsars, ‘accretors’ denotes binary systems in the Milky way that undergo accretion, and SNe and GRBs refer to supernovae and gamma ray bursts. The black star denotes the burst detected from the galactic magnetar SGR1935+2154 and is seen below the population of FRBs. Lines indicate constant brightness temperature and the shaded region below 10^{12} K indicates sources that are likely incoherent emitters. Figure from (Bochenek et al. 2020) reprinted with permission from Springer Nature.

repeaters varied smoothly to durations up to ~ 30 ms. Pleunis et al. (2021b) also visually identifies four basic morphologies of FRB, (a) broadband bursts with a single peak, (b) narrowband bursts with a single peak, (c) complex bursts with multiple peaks, similar frequency extent, and varying intensity, and (d) complex bursts with multiple sub-bursts whose frequency drifts downward with later arrival time (see fig. 3 of Pleunis et al. 2021b for examples). It is not clear what gives rise to these burst morphologies, whether it be propagation effects or due to the emission mechanism.

The advent of wide field observations of transient phenomena brought with it the discovery of a plethora of new unexpected FRB characteristics, including many more repeating sources, periodic sources, different types of burst morphologies, and magnetars as a potential source of some, but not all, FRBs.

1.3 Theories of Origin

The high energies, short durations, and high brightness temperatures seen from FRBs imply a coherent emission mechanism from a compact source, ie. a mechanism whereby the radiation in a burst is emitted in phase resulting in a high amplitude of radiation that is usually beamed in the direction of the observer. This is as opposed to an incoherent mechanism, where thermal processes results in randomly phased photons and a radiation field that is much less intense and much less beamed.

Beyond this basic fact, it is very difficult to model all the observational characteristics seen from FRBs. As we have seen, FRBs are seen in one-off non-repeating events, or from sources that repeat. Sometimes these repeating source are periodic, possibly suggesting some kind of orbital motion between the source and a companion object. Because FRBs can repeat, the mechanism of emission is not inherently cataclysmic, and the lack of counterpart at non radio wavelengths either suggests an observational lack of sensitivity to signals at different wavelengths, or an emission process that efficiently releases energy only

at radio wavelengths. In addition, the polarization properties of FRBs are deeply coupled to the magneto-ionic environment of their source, and different combinations of linearly polarized and circularly polarized signals are seen from FRB sources, complicating our understanding of the inherent polarization induced by the emission mechanism.

This section will summarize the observational data and the constraints they place on modelling the origin and emission mechanism of FRBs, and discuss popular theories in the literature. In particular we focus on a family of theories centered around magnetars, and the triggered relativistic dynamical model for the spectro-temporal properties introduced by our group, as they are most relevant to this thesis. Early on it appeared that the number of models of FRBs would outnumber the actual number of FRBs observed, and no model currently fully explains all the observational characteristics of FRBs, and their true nature remains unknown.

1.3.1 Observational Constraints

Spectro-Temporal Properties

Spectro-temporal properties refer to the features of an FRB that can be measured from the frequency versus time plot of the signal, or waterfall. These include properties such as the burst bandwidth, the burst duration, the center frequency of the burst, the frequency drift rate between multiple sub-bursts if they are present, and the sub-burst slope⁶, which is the frequency drift within a single burst. We have already seen that FRB sources can be distinguished into non-repeating and repeating categories based on their bandwidth and duration, as in the CHIME/FRB catalog (Pleunis et al. 2021b). In addition, of the burst morphologies observed, complex bursts with downward drifting sub-bursts appear to come exclusively from repeating sources. Multiple correlations exist between these spectro temporal properties for bursts from repeaters, such as the inverse relationship

⁶We introduced this terminology in Chamma et al. (2021), and Jahns et al. (2022) uses ‘intra-burst drift rate’.

between the sub-burst slope and duration first described in Rajabi et al. (2020), and exists between distinct repeaters as well (Chamma et al. 2021). The drift rate has also been observed to vary approximately linearly with frequency, as reported in Hessels et al. (2019) and Josephy et al. (2019). These relationships provide useful guides for validating models of FRB emission.

Polarization and Rotation Measure

The polarization measurements of FRBs and RMs derived from them provide additional constraints and challenges to models. Bursts from the repeater FRB20121102A are seen to have no circular polarization and 100% linear polarization with a constant position angle even across studies, as seen in Michilli et al. (2018) and Gajjar et al. (2018). Other repeaters do not follow this trend, for example in observations of the repeater FRB20180301A by Luo et al. (2020) bursts seen to be were highly linearly polarized with no circular polarization, however the polarization angle was seen to behave in a variety of ways, being constant in some bursts, while increasing or decreasing linearly within the profile of a single burst. This behaviour has not been seen in other repeaters, and can be explained for example by the sweeping magnetic field lines around a rotating magnetar (Luo et al. 2020).

Adding additional polarization constraints, Hilmarsson et al. (2021) observed the repeating source FRB20201124A and detected circular polarization fractions of up to 20% for the first time from a repeater in 18 out of 20 bursts detected, in addition to a high fractional linear polarization, and an increase in circular polarization percentage was correlated with greater deviations from the average RM value.

The polarization properties of an FRB source can also drastically change over the timescale of months as seen in 16 bursts from the repeating source FRB20190520B, which were detected between ~ 1.1 and ~ 6.1 GHz by Anna-Thomas et al. (2022) over a span of fourteen months. Over the course of those observations, the RM varied from 2.1×10^3

rad/m to -24×10^3 rad/m, nearly spanning the full range of RMs observed for every pulsar in the Milky Way and most FRBs observed. While the magnitude of the RM observed from FRB20121102A was larger, the range of RMs observed here varied in a way unprecedented for any astrophysical source (see fig. 1 of Anna-Thomas et al. 2022), and the sign change in RM can only be explained by a flipping of the magnetic field orientation along the line of sight (see equation 1.10). The polarization fraction of the bursts seen was seen to decrease with observing frequency.

The large RM variability and decrease in polarization fraction with frequency were interpreted to be the result of propagation through a dense and turbulent plasma around the source (Anna-Thomas et al. 2022). A decrease in polarization (or depolarization) can occur through the process of Faraday conversion, which can occur in dense enough media and causes a transfer between linear polarization and circular polarization. Scattering that occurs along the line of sight through an ionized screen can result in Faraday conversion occurring with differing amounts for differing rays, and, when observed together, can result in a loss of total polarization (Gruzinov and Levin 2019; Vedantham and Ravi 2019).

In Summary, the polarization properties of FRBs are seen to have large polarization fractions as in the nearly completely linearly polarized bursts from FRB20121102A and complex and varying behaviour such as in bursts from the repeaters FRB20180301A, FRB20201124A, and FRB190520B. These observations are potentially understood through propagation through a dense plasma around a highly magnetized environment, and polarimetric observations at different frequencies can be a tool for modelling the details of such an environment.

Activity and Periodicity

Rates of burst activity from FRBs have been observed to fluctuate in unpredictable ways, with rains of bursts happening in a short period of time followed by almost silence. The

existence of periodicity in FRB repeaters implies some kind of binary orbit interaction that could modulate the FRB signals in a periodic way. These temporal properties of FRB activity are difficult to explain but can provide information about the timescales of the objects involved in FRB emission and the emission process itself.

As mentioned earlier, the repeating source FRB20180916B was the first source seen to behave periodically, with a period of 16.35 days and its bursts arriving in clusters of activity throughout the duration of the period. In observations with the Apertif (1220 to 1520 MHz) and LOFAR (110 to 190 MHz) radio telescopes covering seven activity cycles of FRB20180916B, 54 and 9 bursts were detected respectively (Pastor-Marazuela et al. 2021; Pleunis et al. 2021a). When folded over the period of the activity cycle, the higher frequency Apertif bursts were seen to occur in an earlier and narrower window than the low frequency LOFAR bursts, which were also the lowest frequency detections of any FRB. These observations mean that a successful model must explain not only the periodicity of FRB20180916B but also the frequency dependent activity cycle of its bursts.

A possible periodicity of 161 ± 5 days was also found in the first discovered repeater FRB20121102A in multi-wavelength observations by Cruces et al. (2020). The hint of a periodicity first came from the observation that bursts in FRB20121102A were clustered in time, similar to the clustering of burst activity seen from FRB20180916B, and from an analysis of bursts detected with the Lovell telescope along with archival bursts spanning 5 years (Rajwade et al. 2020). Extensive observations were needed to establish this periodicity, with 128 hours of observations over three years combined with observations from Hardy et al. (2017) and Houben et al. (2019), for a total of 165 hours of objects for a just under 3σ detection of a 161 day period. The long period 161 day period of FRB20121102A contrasts with the much shorter 16.35 day period of FRB20180916B, and challenges some models such as precessing neutron stars which are not expected to reach such long periods (Rajwade et al. 2020).

Using the FAST telescope, Xu et al. (2021) detected a whopping 1863 bursts from FRB20201124A from April 1 to June 11 2021, with an irregular burst rate that varied from ~ 5 bursts/hr to a peak of ~ 45 bursts/hr. Prior to this active period, FRB20201124A was emitting bursts at a rate of < 3.4 bursts/day (Lanman et al. 2022). Over the duration of FAST's observation period, the burst rate fluctuated but increased gradually before suddenly stopping completely, with no bursts detected 20 days after the sudden end. The RM of the bursts evolved as well, varying irregularly from -887 rad/m² to -362 rad/m² over the course of the observations. Interestingly, the RM variations halted 20 days before the sudden end in bursts while the burst rate was increasing. The bursts detected from FRB20201124A had high levels of circular polarization differing from observations of other FRBs and were thus inconsistent with Faraday conversion as the sole source of circular polarization. Since Faraday conversion is a propagation effect, this suggests that the level of circular polarization originates from the emission mechanism.

These observations show that the burst rate and activity of a source can vary in sudden and dramatic ways, and that these variations in activity can be connected to the magneto-ionic environment of the source. It is not yet clear if all repeaters have a periodicity, since FRB20121102A showed that such a period can be quite long and require years of observation to establish.

Environments

Several FRB sources have been localized to host galaxies and are typically found in or near star-forming regions, consistent with FRBs originating from a young compact source such as a magnetar (Petroff, Hessels, and Lorimer 2022). A handful of repeaters such as FRB20121102A have been co-located with a persistent radio source, supporting the association with a compact object. Using the Australian Square Kilometer Array (ASKAP), Bhandari et al. (2020) localized four different FRBs using a single burst to 4 different host galaxies and found that all of them were located in the outskirts of their

galaxy. Differences in localized environments exist between FRBs, with, for example, FRB20200120E localized to a globular cluster in the nearby galaxy M81 (Bhardwaj et al. 2021; Kirsten et al. 2021). Globular clusters consist of old stellar populations and do not host star formation, so explaining this FRB source requires a different way of forming a compact highly magnetized object such as a magnetar. For example, a merger or a stellar collapse triggered by accretion could be needed (Kirsten et al. 2021). Following the localization of the periodic repeater FRB20180916B, Tendulkar et al. (2020) studied the 60 pc environment around the source and found that FRB20180916B was 250 pc away from the nearest site of star-formation, a distance incompatible with the typical velocities of a young magnetar leaving its stellar nursery. They concluded that it would take 800 kyr - 7 Myr to arrive at its present location while a magnetar is only expected to be active in its first 10 kyr. Though FRBs seem to consistently come from highly-magnetized compact regions, these regions have been localized to a diverse array of larger environments in their host galaxies.

In addition to the constraints listed above, such as the spectro-temporal properties of bursts, their polarization signatures, the activities and periods of repeating sources, and the variety of environments that FRBs are found in, any successful model of FRBs must of course explain the vast energies and high brightness temperatures seen from FRBs. Furthermore, they should also be able to explain these signals without significant counterpart at other wavelengths of the electromagnetic spectrum, as despite several multi-wavelength studies, no significant amount of radiation in the optical, X-ray, or gamma rays have been detected except the event from SGR1935+2154, and FRBs are almost exclusively seen in the radio.

1.3.2 Magnetars and other compact progenitors

The short durations and high brightness temperatures of FRBs imply that the source of FRBs must be compact and that emission is coherent (Lyubarsky 2021). As discussed

in Section 1.2.1 brightness temperatures of FRBs are observed in excess of 10^{35} K. Since the brightness temperature of a group of emitting particles must be less than its actual temperature (we observe it at a distance), the high brightness temperature can only be explained if the electromagnetic waves are emitted in phase by a large number of particles. If we assume an event cannot originate from an extent that is larger than the time it takes for light to travel across is, then the durations of FRBs imply that the size of the emitting region a is less than about

$$a \lesssim \tau c \sim (1 \text{ ms}) c \sim 300 \text{ km}, \quad (1.11)$$

where 1 ms is the order of magnitude of bursts observed and c is the speed of light. In astronomy objects of size 300 km with the energy densities capable of producing FRBs are stellar remnants with extreme environments such as white dwarfs, neutron stars, magnetars (young neutron stars that are highly magnetized), and black holes. If the source is relativistic, then the condition in equation (1.11) does not hold and the size of the region a can scale to astronomical sizes (Rybicki and Lightman 1979).

As an example of how a compact object could generate FRBs, an enormous gamma-ray burst dubbed a ‘giant flare’ or ‘hyperflare’ from a galactic magnetar released 10^{46} erg of energy and was, at the time, the brightest event ever observed from within our galaxy, releasing more energy in 0.2 s than the sun does in a quarter of a million years (Hurley et al. 2005; Palmer et al. 2005; Popov and Postnov 2007). The powerful magnetic fields surrounding magnetars are an enormous reservoir of energy that can be released by magnetic ‘braking’ with material in the surrounding environment or through reconnection events. Reconnection events, analogous to magnetic field loops and coronal mass ejections seen in our Sun, involve the sudden and violent release of material as the end points of the super strong magnetic field snap off and then reconnect back onto the surface of the magnetar. These events are believed to be responsible for gamma ray and X-ray

bursts observed from magnetars and can potentially lead to radio emission when charged particles are trapped by and travel along the magnetic field lines (Lyutikov 2002).

Because of the rates of hyperflares and the proposed reconnection mechanism by Lyutikov (2002), flares from magnetars were quickly believed to be possible sources of FRBs (Popov and Postnov 2007). As evidenced by hyperflares, magnetars have the necessary energy budget to generate FRBs even from repeating sources and the observation of a weak FRB from a galactic magnetar (CHIME/FRB 2020a; Bochenek et al. 2020) strongly suggests magnetars as a possible progenitor of at least some FRBs (Popov and Postnov 2007; Lyubarsky 2021; Petroff, Hessels, and Lorimer 2022).

Magnetars (first described and coined in Duncan and Thompson 1992) are neutron stars that form under certain conditions during gravitational collapse, producing a magnetic field between $B \sim 10^{14} - 10^{15}$ Gauss, or three orders of magnitude greater than normal radio pulsars. The conditions for a magnetar to form include an initial rotation period on the order of 1 ms, leading to convection currents and shearing of the magnetic field that can result in much greater magnetic fields than normal (Duncan and Thompson 1992). Magnetars were first observed through the detection of repeating soft-gamma ray bursts with 8-second pulsations from the Venera 11 and 12 space probes (Mazets et al. 1979; Mazets, Golenetskij, and Guryan 1979; Kaspi and Beloborodov 2017), and observations of similar sources led to the designation of a class of astrophysical source called Soft-Gamma-ray Repeaters (SGRs) due to a lower spectral energy distribution than typical Gamma-Ray Bursts (GRBs). Certain phenomena distinguish magnetars from radio pulsars or other neutron stars, including extreme magnetic braking where magnetic energy is dissipated into surrounding material and slows the rotation period P of the magnetar. The measurement of the time derivative of a pulsating object's period \dot{P} , or the spin-down rate, can be used to estimate the magnetic field strength. The magnetic field strength can be estimated through $B = 3.2 \times 10^{19} \sqrt{P\dot{P}}$ G (Kaspi and Beloborodov 2017) and the measurement of two spin-down rates for SGR 1806-20 and

SGR 1900+14 implied magnetic field strengths of 10^{14} G, confirming the existence of magnetars and that SGRs originate from them (Kouveliotou et al. 1998, 1999).

Magnetars are difficult to detect and are primarily observed through soft-gamma ray or X-ray bursts (Duncan and Thompson 1992; Kaspi and Beloborodov 2017). The total number of known magnetars is 30, with 16 of those identified as SGRs and the remaining through their X-ray emission, named Anomalous X-ray Pulsars (AXPs) (Olausen and Kaspi 2014)⁷. The known magnetars, all in our galaxy, are confined to the galactic plane, with a scale height of 20-30 pc. This, along with the measured proper velocities (velocities orthogonal to the line of sight) of the magnetars, implies that magnetars travel about 20 pc every 10^5 years, and the lack of magnetars beyond the galactic plane implies that magnetars are exclusively young neutron stars with a lifetime less than 100,000 years (Kaspi and Beloborodov 2017).

Magnetars are a promising progenitor for some FRBs, satisfying the conditions that they be compact, with energy reservoirs large enough to power one-off FRBs as well as repeating sources in non-cataclysmic events, and with a magnetic environment that is conducive to the emission of coherent radiation.

1.3.3 Coherent Emission Mechanisms

The emission mechanism of FRBs is not known, however most theories center around generating coherent radiation through the interaction of ionized material with a local, complex magnetic field, and the propagation of electromagnetic waves in plasmas around a compact progenitor, such as a magnetar. We briefly summarize here different possible mechanisms that can produce coherent radiation; broader and deeper summaries can be found in, for example, Platts et al. (2019) and Lyubarsky (2021).

⁷<http://www.physics.mcgill.ca/~pulsar/magnetar/main.html>

Curvature Emission by Bunches

One family of theories revolves around emission from bunches of electrons travelling along the curved magnetic field lines of a progenitor, or curvature emission of bunches (Lyubarsky 2021; Wang et al. 2022). Electrons with Lorentz factors $\gamma = 1/\sqrt{1 - v^2/c^2}$ near $\gamma \sim 100$ (or 0.9999 the speed of light) traveling along magnetic field lines form bunches due to plasma waves caused by instabilities in the plasma. The power P radiated by this mechanism taking into account that the radiation originates from a plasma is given by (Gil, Lyubarsky, and Melikidze 2004; Lyubarsky 2021)

$$P \simeq 0.1 \frac{q^2 c \gamma^4}{R_c^2} \left[\frac{\omega'_c}{\omega'_p} \left(1 - \frac{\gamma_p^2}{\gamma^2} \right) \right]^2, \quad (1.12)$$

where q is the charge of the particles (usually electrons so $q = e$), R_c is the curvature radius of the magnetic field line a bunch travels along, ω'_p is the plasma frequency, $\omega'_c = c\gamma^3/R_c$ is the characteristic frequency emitted by a bunch, and γ and γ_p is the Lorentz factor of the emitting bunch and plasma, respectively. This equation shows that for plasma velocities close to the velocity of the bunch, or $\gamma_p \approx \gamma$, the emitted power is greatly suppressed and even cancels if moving together. Lyubarsky (2021) also argues that the conditions under which bunches are assumed to arise in this model are not realistic as they assume that the plasma instabilities giving rise to the bunches have much lower energy than the plasma, whereas the electric potential energy of the bunch can be shown to be almost a billion times greater than the plasma energy. Because of the theoretical uncertainty in the existence of plasma bunches along a magnetic field line and the suppression of emitted power even if the bunches exist, Lyubarsky (2021) concludes that this family of models are highly speculative. Nonetheless, some studies such as Wang et al. (2022) use the model with reasonable success in explaining some of the polarization and spectro-temporal properties of FRBs.

Synchrotron Masers and Relativistic Shocks

Masers are the generation of coherent radiation through amplification by the stimulated emission of photons (Einstein 1916). A photon with frequency corresponding to the transition energy in an atom or molecule can stimulate the emission of a photon when interacting. A photon emitted in this way is in phase with the stimulating photon and significant amplification of the radiation field (ie. an increase in the number of photons) can result if there exists a large population of atoms or molecules in an excited state, a phenomenon commonly referred to as “population inversion”.

Synchrotron radiation results from the rotational motion experienced by charged particles in a magnetic field. Electrons, which are usually the primary constituents of a plasma, cannot experience an inversion in the population of their energy levels unless they are relativistic (Lyubarsky 2021). Relativistic electron in synchrotron motion will emit at, and at harmonics of, their rotational frequency, and if an inversion exists in the population this radiation can be amplified by stimulated emission, resulting in a synchrotron maser.

A popular way of generating the inversion necessary for a synchrotron maser is through relativistic shock waves, where material emitted by the progenitor moving at extreme velocities moves into an area with strong magnetization. Charges in the relativistic shock respond to the magnetization by gyrating, creating an inversion, an ultimately producing coherent radiation (Gallant et al. 1992; Metzger, Margalit, and Sironi 2019).

Such models can explain the high degrees of linear polarization observed from FRBs such as FRB20121102A, as well as the consistent polarization angle observed over months of observations, also in FRB20121102A (Michilli et al. 2018; Gajjar et al. 2018), through a fixed direction for the magnetic field in the plasma that the shock wave encounters. If the synchrotron maser in relativistic shocks is powered by material ejected from a magnetar or similar compact object then the direction of the magnetic is fixed in the direction normal to the rotation axis as needed to explain the aforementioned polarization properties

(Metzger, Margalit, and Sironi 2019).

Dicke's Superradiance

Dicke's Superradiance (Dicke 1954) is a cooperative quantum optical phenomenon where ensembles of atoms or molecules interact with one another through their common electromagnetic field resulting in enhanced spontaneous emission rates. The radiation emanating from the ensemble is coherent, and exhibits timescales and intensities that are a function of the number of molecules in the system, and so spontaneously emit differently when together. With the understanding that the interaction with a common radiation field leads to entanglement of the gas's constituents Dicke (1954) considers a radiating gas as a single quantum-mechanical system and calculates correlations of the energy states between different atoms/molecules in the gas, for both small volumes and gas spanning a large extent with a distribution of velocities.

A simple example motivating such a correlation is given in the case of a neutron radiating in a uniform magnetic field; when alone, an excited neutron (say, with its spin up) will eventually decay to its ground state through a magnetic dipole transition and emit a photon with 100% probability. However, when in proximity to another neutron with opposite initial spin state, the system can evolve to only a 50% chance of having transitioned, since the initial state of the system is a superposition of the corresponding triplet (spin $s = 1$) and singlet ($s = 0$) states. In comparison, the probability of emission is 100% but at twice the transition rate if the system is initially in the triplet state. In contrast, because the singlet state cannot couple to the state where both neutrons are de-excited the probability of emission is 0% when in that state. Dicke (1954) also showed that a pulse of coherent radiation can stimulate gas into a state of coherent emission. Thus superradiance has the necessary ingredients for enhancing intensities of radiation from a gas, modifying the timescales of emission for potentially burst-like behaviour, and producing coherent radiation.

Applying superradiance to astrophysical masers, Rajabi and Houde (2016a,b, 2017) showed that for different spectral transitions such as the 21 cm line in Hydrogen, the OH 1612 MHz, the 6.7 GHz methanol, and the 22 GHz water spectral lines superradiance is characterized by high-intensity and coherent burst like behaviour, with timescales ranging from seconds to years. By modelling maser flares with superradiance, these studies imply that large numbers of molecules over astronomical distances can form entangled quantum mechanical systems and emit coherently as an ensemble. Pulses generated in superradiance have a characteristic time-scale T_R given by

$$T_R = \tau_{\text{sp}} \frac{8\pi}{3nL\lambda^2}, \quad (1.13)$$

where τ_{sp} is the timescale of spontaneous decay for the transition, n is the density of inverted molecules, L is the length of the superradiating sample, and λ is the wavelength of the radiation. The total number of molecules participating in the superradiant emission is given by $N = n\lambda^2 L$ for a cylindrical sample. Bursts are emitted after the inversion density reaches a critical threshold $(nL)_{\text{crit}}$ given by

$$(nL)_{\text{crit}} \simeq \frac{2\pi}{3\lambda^2} \frac{\tau_{\text{sp}}}{T'} \left| \ln \left(\pi\sqrt{N} \right) \right|^2, \quad (1.14)$$

where T' is the timescale of collisions and other non-coherent processes that dampen superradiance, and after a delay time τ_D given by

$$\tau_D \simeq \frac{T_R}{4} \left| \ln \left(\pi\sqrt{N} \right) \right|^2. \quad (1.15)$$

Equations (1.13) to (1.15) show that the duration of a pulse scales as $T_R \propto \tau_{\text{sp}}/N$ while the intensity of the pulse I can be shown to be proportional to $I \propto N^2 I_0$, where I_0 is the intensity of a single molecule when emitting non-coherently (Houde, Mathews, and Rajabi 2017; Houde et al. 2019). Superradiant pulses can also exhibit ringing, or multiple

bursts of decreasing intensity after the initial pulse.

The characteristic timescales and intensities of superradiant pulses and their dependence on the number of molecules N allow for the modelling of FRB pulses (Mathews 2017), as done in Houde, Mathews, and Rajabi (2017) for FRB110220, FRB150418, and a burst from FRB20121102A. This showed that superradiance could be used to account for the timescales, profiles, intensities, polarization and repeating behavior of FRBs. Houde et al. (2019) shows that a pulse of coherent radiation can trigger a superradiant pulse (the FRB in this model) by polarizing the medium and reducing the critical threshold $(nL)_{\text{crit}}$ needed for superradiance. Houde et al. (2019) used superradiant pulses based on the OH 1612 MHz and 6030 MHz lines to model FRB110220 (Figure 1.3) and two bursts from FRB20121102A. For FRB110220 an inversion density of $n \sim 0.01 \text{ cm}^{-3}$, a sample size of 280 au and a trigger pulse lasting 0.54 ms was sufficient to produce the profile of the FRB. For FRB20121102A similar values held, with a sample size of 300 au and a range of number densities between 0.12 and 1 cm^{-3} , with a trigger duration of 0.1 ms. These triggered superradiant models require lots of material and very short coherent triggers to produce FRBs, and Houde et al. (2019) argued that young pulsars could produce the necessary triggers out to a distance of 100 pc from the FRB source.

1.3.4 Triggered Relativistic Dynamical Model⁸

The triggered superradiant model for FRBs implies that the FRB source itself is a population of molecules or atoms in a gaseous or plasma state becoming quantum entangled through a coherent trigger. Separate from superradiance or any other emission mechanism, if the FRB source truly is a diffuse cloud of some sort then it will be subject to dynamical motions at potentially relativistic velocities that will affect the observed spectro-temporal properties of FRBs emitted from it, especially when considering the extragalactic nature of FRBs. To characterize the effect of these motions on the spectro-

⁸F. Rajabi, M. A. Chamma, C. M. Wyenberg, A. Mathews, & M. Houde. MNRAS, Volume 498, Issue 4, pp. 4936-4942. See co-authorship statement and Chapter 2 for my contribution to this paper.

temporal properties of FRBs and inspired by the triggered model in the context of superradiance, Rajabi et al. (2020) presented a simple dynamical model and derived several relationships that could account for observed effects such as the drift rate of bursts with multiple components, where sub-bursts within a burst arrive at lower frequencies at later times, or the decrease in burst duration with increasing frequency. In addition it predicted a novel inverse relationship between the sub-burst slope (drift rate within a single sub-burst) and burst duration that was verified with a small sample of bursts from FRB20121102A. This model presents a picture of FRBs that is consistent with them resulting from a narrow-band emission process and the wide-band measurements of FRBs being due to relativistic motions within the source. This model is consistent with Dicke's superradiance but is agnostic to the details of the emission mechanism and trigger, and only considers the motions of the source.

Figures 1.6 and 1.7 respectively show a schematic and time sequence of the FRB phenomenon as conceptualized within the triggered relativistic dynamical model (TRDM). The system consists of the FRB source located between the trigger and the observer with the source moving towards the observer with some relativistic velocity $\beta = v/c$. The time sequence of events consists of a trigger followed by a time delay τ'_D preceding the emission of the FRB at an assumed rest frame frequency ν_0 with duration τ'_w , where the prime indicates the durations as measured in the rest frame of the source.

By applying the Lorentz transformation on the space-time coordinates of the event to determine their coordinates in the observer's frame as well as the relativistic Doppler shift formula to account for the change in observed frequency, Rajabi et al. (2020) derive several relationships between the spectro-temporal properties of a burst. The time delay t_D and burst duration t_w in the observer frame are given by

$$t_D = \tau'_D \frac{\nu_0}{\nu_{\text{obs}}}, \quad (1.16)$$

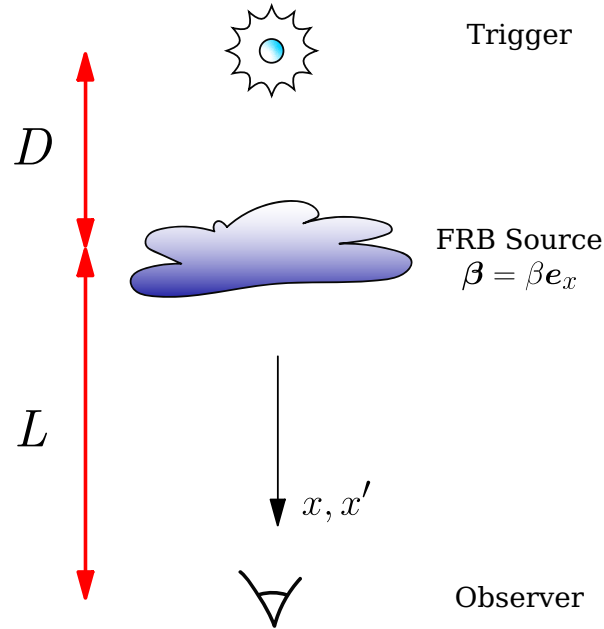


Figure 1.6: Schematic of the system considered for the FRB model of Rajabi et al. (2020). It consists of a trigger source, an FRB source and an observer. All are assumed to be aligned along the line of sight from the observer, with the trigger source located behind the FRB. The FRB source is moving at a potentially relativistic velocity $\mathbf{v} = \boldsymbol{\beta}c = \beta c \mathbf{e}_x$ relative to the observer. Figure taken from Rajabi et al. (2020).

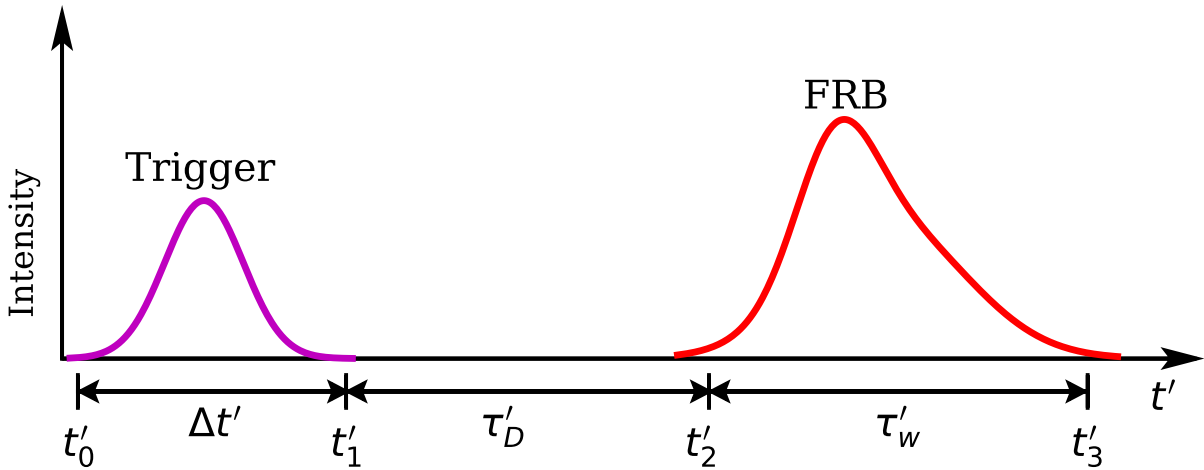


Figure 1.7: Time sequence for the trigger signal, the delay time τ'_D and the burst duration τ'_w as seen in the reference frame of the FRB source (not to scale). Figure taken from Rajabi et al. (2020).

$$t_w = \tau'_w \frac{\nu_0}{\nu_{\text{obs}}}, \quad (1.17)$$

where

$$\nu_{\text{obs}} = \nu_0 \sqrt{\frac{1 + \beta}{1 - \beta}}, \quad (1.18)$$

is the observed frequency of the burst given by the relativistic Doppler shift formula. This shows an inverse relationship between a burst's duration and its frequency.

For FRBs with multiple sub-bursts, as is occasionally observed, equation (1.16) can be used to find the differences in their arrival times Δt_D when assuming they were all emitted at the same rest frame frequency ν_0 with slightly differing velocities β to obtain

$$\Delta t_D = -t_D \left(\frac{\Delta \nu_{\text{obs}}}{\nu_{\text{obs}}} - \frac{\Delta \tau'_D}{\tau'_D} \right). \quad (1.19)$$

This equation can be used to derive a relationship for the drift rate between multiple sub-bursts $\Delta \nu_{\text{obs}}/\Delta t_D$ by considering the second term describing sub-bursts with varying proper delay time $\Delta \tau'_D$, and yields

$$\frac{\Delta \nu_{\text{obs}}}{\Delta t_D} = \frac{\nu_{\text{obs}}}{\nu_0} \frac{d\nu_{\text{obs}}}{d\tau'_D}, \quad (1.20)$$

where $d\nu_{\text{obs}}/d\tau'_D$ is a parameter whose sign determines if the sub-bursts decrease in frequency with increasing arrival time (negative) or if their frequency increases (positive). Equation (1.19) in turn can be used to find a relationship for the sub-burst slope $d\nu_{\text{obs}}/dt_D$ by considering a single sub-burst ($\Delta \tau'_D = 0$),

$$\frac{d\nu_{\text{obs}}}{dt_D} = - \left(\frac{\tau'_w}{\tau'_D} \right) \frac{\nu_{\text{obs}}}{t_w}, \quad (1.21)$$

which predicts an inverse relationship with the burst duration and a linear relationship with the observed burst frequency.

In the TRDM, the spectral extent and differences in arrival and time and duration are

simply due to differences in the velocity β of FRB sources along the line-of-sight relative to the observer.

1.4 This Thesis

The predictions of the triggered relativistic dynamical model (Rajabi et al. 2020) are all readily testable through the measurement of spectro-temporal properties and such work is the central theme of my thesis.

Chapter 2 will detail the first measurements of sub-burst slope for a small sample of bursts from the first repeater discovered, FRB20121102A. These measurements are used to validate the predictions of TRDM, finding evidence for the inverse relationship predicted between the sub-burst slope and duration.

Following this work I explore this relationship for other repeating FRBs, and Chapter 3 details an analysis of bursts from FRB20121102A once more, the second repeater discovered FRB20180814A, and the first repeating periodic source discovered FRB20180916B, where we see that the inverse relationship predicted in the TRDM holds for all three sources and that they are nearly indistinguishable from one another.

Finally, I focus on the bursts of a single source to test the limits of the TRDM and to understand if every burst from a source obeys the same spectro-temporal relationships. I analyse a broad sample of bursts from the most well observed repeater FRB20121102A. The bursts from this source span the broadest range of observed frequencies and durations and has been observed for the longest period of time (owing to it being the first discovered repeater). Chapter 4 describes this analysis and finds that the broad sample of bursts fit well with the predictions of the TRDM, and also details the discovery of a relationship between the bandwidth and sub-burst duration that cannot be explained within the TRDM, potentially providing a new clue to the emission mechanism of FRBs.

Bibliography

- Akahori, Takuya, Dongsu Ryu, and B. M. Gaensler (June 2016). “Fast Radio Bursts as Probes of Magnetic Fields in the Intergalactic Medium”. In: *ApJ* 824.2, 105, p. 105. DOI: [10.3847/0004-637X/824/2/105](https://doi.org/10.3847/0004-637X/824/2/105). arXiv: [1602.03235](https://arxiv.org/abs/1602.03235) [astro-ph.CO]. URL: <https://ui.adsabs.harvard.edu/abs/2016ApJ...824..105A>.
- Amiri, M. et al. (2019). “A second source of repeating fast radio bursts”. In: *Nature* 566.7743, pp. 235–238. DOI: [10.1038/s41586-018-0864-x](https://doi.org/10.1038/s41586-018-0864-x). arXiv: [1901.04525](https://arxiv.org/abs/1901.04525) [astro-ph.HE]. URL: <https://ui.adsabs.harvard.edu/abs/2019Natur.566..235C>.
- Anna-Thomas, Reshma et al. (Feb. 22, 2022). “A Highly Variable Magnetized Environment in a Fast Radio Burst Source”. In: *arXiv*. arXiv: [2202.11112](https://arxiv.org/abs/2202.11112) [astro-ph.HE]. URL: <https://arxiv.org/abs/2202.11112>.
- Bannister, K. W. et al. (Aug. 2019). “A single fast radio burst localized to a massive galaxy at cosmological distance”. In: *Science* 365.6453, pp. 565–570. DOI: [10.1126/science.aaw5903](https://doi.org/10.1126/science.aaw5903). arXiv: [1906.11476](https://arxiv.org/abs/1906.11476) [astro-ph.HE]. URL: <https://ui.adsabs.harvard.edu/abs/2019Sci...365..565B>.
- Bhandari, Shivani et al. (May 27, 2020). “The host galaxies and progenitors of Fast Radio Bursts localized with the Australian Square Kilometre Array Pathfinder”. In: DOI: <https://doi.org/10.3847/2041-8213/ab672e>. arXiv: [http://arxiv.org/abs/2005.13160v1](https://arxiv.org/abs/2005.13160v1) [astro-ph.GA].

- Bhardwaj, M. et al. (2021). “A Nearby Repeating Fast Radio Burst in the Direction of M81”. In: *The Astrophysical Journal Letters* 910.2, p. L18. DOI: [10.3847/2041-8213/abeaa6](https://doi.org/10.3847/2041-8213/abeaa6).
- Bochenek, C. D. et al. (Nov. 2020). “A fast radio burst associated with a Galactic magnetar”. en. In: *Nature* 587.7832, pp. 59–62. DOI: [10.1038/s41586-020-2872-x](https://doi.org/10.1038/s41586-020-2872-x). arXiv: [2005.10828](https://arxiv.org/abs/2005.10828) [astro-ph.HE]. URL: <https://ui.adsabs.harvard.edu/abs/2020Natur.587...59B>.
- Burke-Spolaor, S. et al. (Jan. 2011). “Radio Bursts with Extragalactic Spectral Characteristics Show Terrestrial Origins”. In: *The Astrophysical Journal* 727.1, 18, p. 18. DOI: [10.1088/0004-637X/727/1/18](https://doi.org/10.1088/0004-637X/727/1/18). arXiv: [1009.5392](https://arxiv.org/abs/1009.5392) [astro-ph.CO]. URL: <https://ui.adsabs.harvard.edu/abs/2011ApJ...727...18B>.
- Burns, W. R. and B. G. Clark (July 1969). “Pulsar Search Techniques”. In: *A&A* 2, pp. 280–287. URL: <https://ui.adsabs.harvard.edu/abs/1969A&A....2..280B>.
- Chamma, Mohammed A et al. (2021). “Evidence of a shared spectro-temporal law between sources of repeating fast radio bursts”. In: *Monthly Notices of the Royal Astronomical Society* 507.1, pp. 246–260. DOI: [10.1093/mnras/stab2070](https://doi.org/10.1093/mnras/stab2070).
- Champion, D. J. et al. (July 2016). “Five new fast radio bursts from the HTRU high-latitude survey at Parkes: first evidence for two-component bursts”. In: *MNRAS* 460.1, pp. L30–L34. DOI: [10.1093/mnrasl/slw069](https://doi.org/10.1093/mnrasl/slw069). arXiv: [1511.07746](https://arxiv.org/abs/1511.07746) [astro-ph.HE]. URL: <https://ui.adsabs.harvard.edu/abs/2016MNRAS.460L..30C>.
- Chatterjee, S. et al. (Jan. 2017). “A direct localization of a fast radio burst and its host”. In: *Nature* 541.7635, pp. 58–61. DOI: [10.1038/nature20797](https://doi.org/10.1038/nature20797). arXiv: [1701.01098](https://arxiv.org/abs/1701.01098) [astro-ph.HE]. URL: <https://ui.adsabs.harvard.edu/abs/2017Natur.541...58C>.
- CHIME/FRB (2020a). “A bright millisecond-duration radio burst from a Galactic magnetar”. en. In: *Nature*. DOI: [10.11570/20.0006](https://doi.org/10.11570/20.0006).

- CHIME/FRB (2020b). “Periodic activity from a fast radio burst source”. In: *Nature* 582.7812, pp. 351–355. DOI: [10.1038/s41586-020-2398-2](https://doi.org/10.1038/s41586-020-2398-2).
- CHIME/FRB Collaboration et al. (Aug. 2018). “The CHIME Fast Radio Burst Project: System Overview”. In: *ApJ* 863.1, 48, p. 48. DOI: [10.3847/1538-4357/aad188](https://doi.org/10.3847/1538-4357/aad188). arXiv: [1803.11235](https://arxiv.org/abs/1803.11235) [[astro-ph.IM](#)]. URL: <https://ui.adsabs.harvard.edu/abs/2018ApJ...863...48C>.
- CHIME/FRB Collaboration et al. (Dec. 2021). “The First CHIME/FRB Fast Radio Burst Catalog”. In: *ApJS* 257.2, 59, p. 59. DOI: [10.3847/1538-4365/ac33ab](https://doi.org/10.3847/1538-4365/ac33ab). arXiv: [2106.04352](https://arxiv.org/abs/2106.04352) [[astro-ph.HE](#)]. URL: <https://ui.adsabs.harvard.edu/abs/2021ApJS..257...59C>.
- Cordes, J. M. and T. J. W. Lazio (July 8, 2002). “NE2001.I. A New Model for the Galactic Distribution of Free Electrons and its Fluctuations”. In: arXiv: [astro-ph/0207156](https://arxiv.org/abs/astro-ph/0207156) [[astro-ph](#)].
- Cordes, J. M. and M. A. McLaughlin (2003). “Searches for Fast Radio Transients”. In: *The Astrophysical Journal* 596.2, pp. 1142–1154. DOI: [10.1086/378231](https://doi.org/10.1086/378231).
- Cordes, J. M. et al. (2004). “The Brightest Pulses in the Universe: Multifrequency Observations of the Crab Pulsar’s Giant Pulses”. In: *The Astrophysical Journal* 612.1, pp. 375–388. DOI: [10.1086/422495](https://doi.org/10.1086/422495).
- Cordes, J. M. et al. (Jan. 2006). “Arecibo Pulsar Survey Using ALFA. I. Survey Strategy and First Discoveries”. In: *ApJ* 637.1, pp. 446–455. DOI: [10.1086/498335](https://doi.org/10.1086/498335). arXiv: [astro-ph/0509732](https://arxiv.org/abs/astro-ph/0509732) [[astro-ph](#)]. URL: <https://ui.adsabs.harvard.edu/abs/2006ApJ...637..446C>.
- Cruces, M et al. (2020). “Repeating behaviour of FRB 121102: periodicity, waiting times, and energy distribution”. In: *Monthly Notices of the Royal Astronomical Society* 500.1, pp. 448–463. DOI: [10.1093/mnras/staa3223](https://doi.org/10.1093/mnras/staa3223).
- Dicke, R. H. (1954). “Coherence in Spontaneous Radiation Processes”. In: *Physical Review* 93.1, pp. 99–110. DOI: [10.1103/physrev.93.99](https://doi.org/10.1103/physrev.93.99).

- Duncan, Robert C. and Christopher Thompson (June 1992). “Formation of Very Strongly Magnetized Neutron Stars: Implications for Gamma-Ray Bursts”. In: *ApJ* 392, p. L9. DOI: [10.1086/186413](https://doi.org/10.1086/186413). URL: <https://ui.adsabs.harvard.edu/abs/1992ApJ...392L...9D>.
- Einstein, Albert (Jan. 1916). “Strahlungs-Emission und Absorption nach der Quantentheorie”. In: *Deutsche Physikalische Gesellschaft* 18, pp. 318–323. URL: <https://ui.adsabs.harvard.edu/abs/1916DPhyG...18..318E>.
- Gajjar, V. et al. (2018). “Highest Frequency Detection of FRB 121102 at 4–8 GHz Using the Breakthrough Listen Digital Backend at the Green Bank Telescope”. In: *The Astrophysical Journal* 863.1, p. 2. DOI: [10.3847/1538-4357/aad005](https://doi.org/10.3847/1538-4357/aad005).
- Gallant, Yves A. et al. (May 1992). “Relativistic, Perpendicular Shocks in Electron-Positron Plasmas”. In: *ApJ* 391, p. 73. DOI: [10.1086/171326](https://doi.org/10.1086/171326). URL: <https://ui.adsabs.harvard.edu/abs/1992ApJ...391...73G>.
- Gil, Janusz, Yuri Lyubarsky, and George I. Melikidze (Jan. 2004). “Curvature Radiation in Pulsar Magnetospheric Plasma”. In: *ApJ* 600.2, pp. 872–882. DOI: [10.1086/379972](https://doi.org/10.1086/379972). arXiv: [astro-ph/0310621](https://arxiv.org/abs/astro-ph/0310621) [astro-ph]. URL: <https://ui.adsabs.harvard.edu/abs/2004ApJ...600..872G>.
- Gruzinov, Andrei and Yuri Levin (May 2019). “Conversion Measure of Faraday Rotation-Conversion with Application to Fast Radio Bursts”. In: *ApJ* 876.1, 74, p. 74. DOI: [10.3847/1538-4357/ab0fa3](https://doi.org/10.3847/1538-4357/ab0fa3). arXiv: [1902.01485](https://arxiv.org/abs/1902.01485) [astro-ph.HE]. URL: <https://ui.adsabs.harvard.edu/abs/2019ApJ...876...74G>.
- Hankins, T. H. et al. (2003). “Nanosecond radio bursts from strong plasma turbulence in the Crab pulsar”. In: *Nature* 422.6928, pp. 141–143. DOI: [10.1038/nature01477](https://doi.org/10.1038/nature01477).
- Hankins, Timothy H. and Barney J. Rickett (1975). “Pulsar Signal Processing”. In: *Methods in Computational Physics: Advances in Research and Applications*. Elsevier, pp. 55–129. DOI: [10.1016/b978-0-12-460814-6.50007-3](https://doi.org/10.1016/b978-0-12-460814-6.50007-3).

- Hardy, L. K. et al. (Dec. 2017). “A search for optical bursts from the repeating fast radio burst FRB 121102”. In: *MNRAS* 472.3, pp. 2800–2807. DOI: [10.1093/mnras/stx2153](https://doi.org/10.1093/mnras/stx2153). arXiv: [1708.06156](https://arxiv.org/abs/1708.06156) [astro-ph.IM]. URL: <https://ui.adsabs.harvard.edu/abs/2017MNRAS.472.2800H>.
- Hessels, J. W. T. et al. (2019). “FRB 121102 Bursts Show Complex Time–Frequency Structure”. In: *The Astrophysical Journal* 876.2, p. L23. DOI: [10.3847/2041-8213/ab13ae](https://doi.org/10.3847/2041-8213/ab13ae).
- Hewish, A. et al. (1968). “Observation of a Rapidly Pulsating Radio Source”. In: *Nature* 217.5130, pp. 709–713. DOI: [10.1038/217709a0](https://doi.org/10.1038/217709a0).
- Hilmarsson, G H et al. (2021). “Polarization properties of FRB 20201124A from detections with the Effelsberg 100-m radio telescope”. In: *Monthly Notices of the Royal Astronomical Society* 508.4, pp. 5354–5361. DOI: [10.1093/mnras/stab2936](https://doi.org/10.1093/mnras/stab2936).
- Houben, L. J. M. et al. (Mar. 2019). “Constraints on the low frequency spectrum of FRB 121102”. In: *A&A* 623, A42, A42. DOI: [10.1051/0004-6361/201833875](https://doi.org/10.1051/0004-6361/201833875). arXiv: [1902.01779](https://arxiv.org/abs/1902.01779) [astro-ph.HE]. URL: <https://ui.adsabs.harvard.edu/abs/2019A&A...623A..42H>.
- Houde, Martin, Abhilash Mathews, and Fereshteh Rajabi (2017). “Explaining fast radio bursts through Dicke's superradiance”. In: *Monthly Notices of the Royal Astronomical Society* 475.1, pp. 514–522. DOI: [10.1093/mnras/stx3205](https://doi.org/10.1093/mnras/stx3205).
- Houde, Martin et al. (2019). “Triggered superradiance and fast radio bursts”. In: *Monthly Notices of the Royal Astronomical Society* 482.4, pp. 5492–5499. DOI: [10.1093/mnras/sty3046](https://doi.org/10.1093/mnras/sty3046).
- Hurley, K. et al. (Apr. 2005). “An exceptionally bright flare from SGR 1806-20 and the origins of short-duration γ -ray bursts”. In: *Nature* 434.7037, pp. 1098–1103. DOI: [10.1038/nature03519](https://doi.org/10.1038/nature03519). arXiv: [astro-ph/0502329](https://arxiv.org/abs/astro-ph/0502329) [astro-ph]. URL: <https://ui.adsabs.harvard.edu/abs/2005Natur.434.1098H>.

- Inoue, Susumu (2004). “Probing the cosmic reionization history and local environment of gamma-ray bursts through radio dispersion”. In: *Monthly Notices of the Royal Astronomical Society* 348.3, pp. 999–1008. DOI: [10.1111/j.1365-2966.2004.07359.x](https://doi.org/10.1111/j.1365-2966.2004.07359.x).
- Ioka, Kunihiro (2003). “The Cosmic Dispersion Measure from Gamma-Ray Burst Afterglows: Probing the Reionization History and the Burst Environment”. In: *The Astrophysical Journal* 598.2, pp. L79–L82. DOI: [10.1086/380598](https://doi.org/10.1086/380598).
- Jackson, John David (1975). *Classical electrodynamics*. URL: <https://ui.adsabs.harvard.edu/abs/1975clel.book.....J>.
- Jahns, J. N. et al. (Feb. 11, 2022). “The FRB 20121102A November rain in 2018 observed with the Arecibo Telescope”. In: *arXiv*. arXiv: [2202.05705](https://arxiv.org/abs/2202.05705) [astro-ph.HE]. URL: <https://arxiv.org/abs/2202.05705>.
- Josephy, A. et al. (2019). “CHIME/FRB Detection of the Original Repeating Fast Radio Burst Source FRB 121102”. In: *The Astrophysical Journal* 882.2, p. L18. DOI: [10.3847/2041-8213/ab2c00](https://doi.org/10.3847/2041-8213/ab2c00).
- Kaspi, Victoria M. and Andrei M. Beloborodov (Aug. 2017). “Magnetars”. In: *ARA&A* 55.1, pp. 261–301. DOI: [10.1146/annurev-astro-081915-023329](https://doi.org/10.1146/annurev-astro-081915-023329). arXiv: [1703.00068](https://arxiv.org/abs/1703.00068) [astro-ph.HE]. URL: <https://ui.adsabs.harvard.edu/abs/2017ARA&A.55..261K>.
- Keith, M. J. et al. (2010). “The High Time Resolution Universe Pulsar Survey - I. System configuration and initial discoveries”. In: *Monthly Notices of the Royal Astronomical Society* 409.2, pp. 619–627. DOI: [10.1111/j.1365-2966.2010.17325.x](https://doi.org/10.1111/j.1365-2966.2010.17325.x).
- Kirsten, F. et al. (May 24, 2021). “A repeating fast radio burst source in a globular cluster”. In: *arXiv*: [2105.11445](https://arxiv.org/abs/2105.11445) [astro-ph.HE].
- Kouveliotou, C. et al. (May 1998). “An X-ray pulsar with a superstrong magnetic field in the soft γ -ray repeater SGR1806 - 20”. In: *Nature* 393.6682, pp. 235–237. DOI: [10.1038/30410](https://doi.org/10.1038/30410). URL: <https://ui.adsabs.harvard.edu/abs/1998Natur.393..235K>.

- Kouveliotou, C. et al. (Jan. 1999). “Discovery of a Magnetar Associated with the Soft Gamma Repeater SGR 1900+14”. In: *ApJ* 510.2, pp. L115–L118. DOI: [10.1086/311813](https://doi.org/10.1086/311813). arXiv: [astro-ph/9809140](https://arxiv.org/abs/astro-ph/9809140) [[astro-ph](https://arxiv.org/abs/astro-ph)]. URL: <https://ui.adsabs.harvard.edu/abs/1999ApJ...510L.115K>.
- Lanman, Adam E. et al. (2022). “A Sudden Period of High Activity from Repeating Fast Radio Burst 20201124A”. In: *The Astrophysical Journal* 927.1, p. 59. DOI: [10.3847/1538-4357/ac4bc7](https://doi.org/10.3847/1538-4357/ac4bc7).
- Lorimer, D. R. and M. Kramer (2012). *Handbook of Pulsar Astronomy*. URL: <https://ui.adsabs.harvard.edu/abs/2012hpa...book....L>.
- Lorimer, D. R. et al. (2007). “A Bright Millisecond Radio Burst of Extragalactic Origin”. In: *Science* 318.5851, pp. 777–780. DOI: [10.1126/science.1147532](https://doi.org/10.1126/science.1147532).
- Luo, R. et al. (2020). “Diverse polarization angle swings from a repeating fast radio burst source”. In: *Nature* 586.7831, pp. 693–696. DOI: [10.1038/s41586-020-2827-2](https://doi.org/10.1038/s41586-020-2827-2).
- Lyubarsky, Yuri (2021). “Emission Mechanisms of Fast Radio Bursts”. In: *Universe* 7.3, p. 56. DOI: [10.3390/universe7030056](https://doi.org/10.3390/universe7030056).
- Lyutikov, Maxim (Nov. 2002). “Radio Emission from Magnetars”. In: *ApJ* 580.1, pp. L65–L68. DOI: [10.1086/345493](https://doi.org/10.1086/345493). arXiv: [astro-ph/0206439](https://arxiv.org/abs/astro-ph/0206439) [[astro-ph](https://arxiv.org/abs/astro-ph)]. URL: <https://ui.adsabs.harvard.edu/abs/2002ApJ...580L..65L>.
- Marcote, B. et al. (Jan. 2017). “The Repeating Fast Radio Burst FRB 121102 as Seen on Milliarcsecond Angular Scales”. In: *ApJ* 834.2, L8, p. L8. DOI: [10.3847/2041-8213/834/2/L8](https://doi.org/10.3847/2041-8213/834/2/L8). arXiv: [1701.01099](https://arxiv.org/abs/1701.01099) [[astro-ph.HE](https://arxiv.org/abs/astro-ph.HE)]. URL: <https://ui.adsabs.harvard.edu/abs/2017ApJ...834L...8M>.
- Mathews, Abhilash (2017). *The Role of Superradiance in Cosmic Fast Radio Bursts*. Honours thesis, The University of Western Ontario.
- Mazets, E. P., S. V. Golenetskij, and Y. A. Guryan (Dec. 1979). “Soft gamma-ray bursts from the source B1900+14”. In: *Soviet Astronomy Letters* 5, p. 343. URL: <https://ui.adsabs.harvard.edu/abs/1979SvAL....5..343M>.

- Mazets, E. P. et al. (Dec. 1979). “Observations of a flaring X-ray pulsar in Dorado”. In: *Nature* 282.5739, pp. 587–589. DOI: [10.1038/282587a0](https://doi.org/10.1038/282587a0). URL: <https://ui.adsabs.harvard.edu/abs/1979Natur.282..587M>.
- McLaughlin, M. A. and J. M. Cordes (2003). “Searches for Giant Pulses from Extragalactic Pulsars”. In: *The Astrophysical Journal* 596.2, pp. 982–996. DOI: [10.1086/378232](https://doi.org/10.1086/378232).
- McLaughlin, M. A. et al. (2006). “Transient radio bursts from rotating neutron stars”. In: *Nature* 439.7078, pp. 817–820. DOI: [10.1038/nature04440](https://doi.org/10.1038/nature04440).
- Mereghetti, S. et al. (Aug. 2020). “INTEGRAL Discovery of a Burst with Associated Radio Emission from the Magnetar SGR 1935+2154”. In: *ApJ* 898.2, L29, p. L29. DOI: [10.3847/2041-8213/aba2cf](https://doi.org/10.3847/2041-8213/aba2cf). arXiv: [2005.06335](https://arxiv.org/abs/2005.06335) [astro-ph.HE]. URL: <https://ui.adsabs.harvard.edu/abs/2020ApJ...898L..29M>.
- Metzger, Brian D., Ben Margalit, and Lorenzo Sironi (May 2019). “Fast radio bursts as synchrotron maser emission from decelerating relativistic blast waves”. In: *MNRAS* 485.3, pp. 4091–4106. DOI: [10.1093/mnras/stz700](https://doi.org/10.1093/mnras/stz700). arXiv: [1902.01866](https://arxiv.org/abs/1902.01866) [astro-ph.HE]. URL: <https://ui.adsabs.harvard.edu/abs/2019MNRAS.485.4091M>.
- Michilli, D. et al. (2018). “An extreme magneto-ionic environment associated with the fast radio burst source FRB 121102”. In: *Nature* 553.7687, pp. 182–185. DOI: [10.1038/nature25149](https://doi.org/10.1038/nature25149).
- Nice, David J. (1999). “Radio Pulses along the Galactic Plane”. In: *The Astrophysical Journal* 513.2, pp. 927–932. DOI: [10.1086/306898](https://doi.org/10.1086/306898).
- Olausen, S. A. and V. M. Kaspi (May 2014). “The McGill Magnetar Catalog”. In: *ApJS* 212.1, 6, p. 6. DOI: [10.1088/0067-0049/212/1/6](https://doi.org/10.1088/0067-0049/212/1/6). arXiv: [1309.4167](https://arxiv.org/abs/1309.4167) [astro-ph.HE]. URL: <https://ui.adsabs.harvard.edu/abs/2014ApJS..212....6O>.
- Oppermann, N. et al. (Mar. 2015). “Estimating extragalactic Faraday rotation”. In: *A&A* 575, A118, A118. DOI: [10.1051/0004-6361/201423995](https://doi.org/10.1051/0004-6361/201423995). arXiv: [1404.3701](https://arxiv.org/abs/1404.3701) [astro-ph.IM]. URL: <https://ui.adsabs.harvard.edu/abs/2015A&A...575A.118O>.

- Palmer, D. M. et al. (Apr. 2005). “A giant γ -ray flare from the magnetar SGR 1806 - 20”. In: *Nature* 434.7037, pp. 1107–1109. DOI: [10.1038/nature03525](https://doi.org/10.1038/nature03525). arXiv: [astro-ph/0503030](https://arxiv.org/abs/astro-ph/0503030) [[astro-ph](#)]. URL: <https://ui.adsabs.harvard.edu/abs/2005Natur.434.1107P>.
- Pastor-Marazuela, Inés et al. (Aug. 2021). “Chromatic periodic activity down to 120 megahertz in a fast radio burst”. In: *Nature* 596.7873, pp. 505–508. DOI: [10.1038/s41586-021-03724-8](https://doi.org/10.1038/s41586-021-03724-8). arXiv: [2012.08348](https://arxiv.org/abs/2012.08348) [[astro-ph.HE](#)]. URL: <https://ui.adsabs.harvard.edu/abs/2021Natur.596..505P>.
- Petroff, E., J. W. T. Hessels, and D. R. Lorimer (2019). “Fast radio bursts”. In: *The Astronomy and Astrophysics Review* 27.1. DOI: [10.1007/s00159-019-0116-6](https://doi.org/10.1007/s00159-019-0116-6).
- (2022). “Fast radio bursts at the dawn of the 2020s”. In: *The Astronomy and Astrophysics Review* 30.1. DOI: [10.1007/s00159-022-00139-w](https://doi.org/10.1007/s00159-022-00139-w).
- Petroff, E. et al. (Aug. 2015). “Identifying the source of perytons at the Parkes radio telescope”. In: *MNRAS* 451.4, pp. 3933–3940. DOI: [10.1093/mnras/stv1242](https://doi.org/10.1093/mnras/stv1242). arXiv: [1504.02165](https://arxiv.org/abs/1504.02165) [[astro-ph.IM](#)]. URL: <https://ui.adsabs.harvard.edu/abs/2015MNRAS.451.3933P>.
- Platts, E. et al. (2019). “A living theory catalogue for fast radio bursts”. In: *Physics Reports* 821, pp. 1–27. DOI: [10.1016/j.physrep.2019.06.003](https://doi.org/10.1016/j.physrep.2019.06.003).
- Pleunis, Z. et al. (2021a). “LOFAR Detection of 110–188 MHz Emission and Frequency-dependent Activity from FRB 20180916B”. In: *The Astrophysical Journal Letters* 911.1, p. L3. DOI: [10.3847/2041-8213/abec72](https://doi.org/10.3847/2041-8213/abec72).
- Pleunis, Ziggy et al. (June 8, 2021b). “Fast Radio Burst Morphology in the First CHIME/FRB Catalog”. In: arXiv: [2106.04356](https://arxiv.org/abs/2106.04356) [[astro-ph.HE](#)].
- Popov, S. B. and K. A. Postnov (Oct. 2007). “Hyperflares of SGRs as an engine for millisecond extragalactic radio bursts”. In: arXiv: [0710.2006](https://arxiv.org/abs/0710.2006) [[astro-ph](#)].

- Rajabi, Fereshteh and Martin Houde (2016a). “DICKE’S SUPERRADIANCE IN ASTROPHYSICS. I. THE 21 cm LINE”. In: *The Astrophysical Journal* 826.2, p. 216. DOI: [10.3847/0004-637x/826/2/216](https://doi.org/10.3847/0004-637x/826/2/216).
- (2016b). “DICKE’S SUPERRADIANCE IN ASTROPHYSICS. II. THE OH 1612 MHz LINE”. In: *The Astrophysical Journal* 828.1, p. 57. DOI: [10.3847/0004-637x/828/1/57](https://doi.org/10.3847/0004-637x/828/1/57).
- (Mar. 2017). “Explaining recurring maser flares in the ISM through large-scale entangled quantum mechanical states”. In: *Science Advances* 3.3, e1601858. DOI: [10.1126/sciadv.1601858](https://doi.org/10.1126/sciadv.1601858). arXiv: [1704.01491 \[astro-ph.GA\]](https://arxiv.org/abs/1704.01491). URL: <https://ui.adsabs.harvard.edu/abs/2017SciA...3E1858R>.
- Rajabi, Fereshteh et al. (2020). “A simple relationship for the spectro-temporal structure of bursts from FRB 121102”. In: *Monthly Notices of the Royal Astronomical Society* 498.4, pp. 4936–4942. DOI: [10.1093/mnras/staa2723](https://doi.org/10.1093/mnras/staa2723).
- Rajwade, K. M. et al. (July 2020). “Possible periodic activity in the repeating FRB 121102”. In: *MNRAS* 495.4, pp. 3551–3558. DOI: [10.1093/mnras/staa1237](https://doi.org/10.1093/mnras/staa1237). arXiv: [2003.03596 \[astro-ph.HE\]](https://arxiv.org/abs/2003.03596). URL: <https://ui.adsabs.harvard.edu/abs/2020MNRAS.495.3551R>.
- Rybicki, George B. and Alan P. Lightman (1979). *Radiative processes in astrophysics*. New York: Wiley.
- Spitler, L. G. et al. (2014). “FAST RADIO BURST DISCOVERED IN THE ARECIBO PULSAR ALFA SURVEY”. In: *The Astrophysical Journal* 790.2, p. 101. DOI: [10.1088/0004-637x/790/2/101](https://doi.org/10.1088/0004-637x/790/2/101).
- Spitler, L. G. et al. (2016). “A repeating fast radio burst”. In: *Nature* 531.7593, pp. 202–205. DOI: [10.1038/nature17168](https://doi.org/10.1038/nature17168).
- Tendulkar, S. P. et al. (Jan. 2017). “The Host Galaxy and Redshift of the Repeating Fast Radio Burst FRB 121102”. In: *ApJ* 834.2, L7, p. L7. DOI: [10.3847/2041-](https://doi.org/10.3847/2041-)

- 8213/834/2/L7. arXiv: [1701.01100](https://arxiv.org/abs/1701.01100) [astro-ph.HE]. URL: <https://ui.adsabs.harvard.edu/abs/2017ApJ...834L...7T>.
- Tendulkar, Shriharsh P. et al. (Nov. 6, 2020). “The 60-pc Environment of FRB 20180916B”. In: arXiv: [2011.03257](https://arxiv.org/abs/2011.03257) [astro-ph.HE].
- Thornton, D. et al. (2013). “A Population of Fast Radio Bursts at Cosmological Distances”. In: *Science* 341.6141, pp. 53–56. DOI: [10.1126/science.1236789](https://doi.org/10.1126/science.1236789).
- Vedantham, H. K. and V. Ravi (May 2019). “Faraday conversion and magneto-ionic variations in fast radio bursts”. In: MNRAS 485.1, pp. L78–L82. DOI: [10.1093/mnrasl/slz038](https://doi.org/10.1093/mnrasl/slz038). arXiv: [1812.07889](https://arxiv.org/abs/1812.07889) [astro-ph.HE]. URL: <https://ui.adsabs.harvard.edu/abs/2019MNRAS.485L..78V>.
- Wang, Wei-Yang et al. (2022). “Magnetospheric Curvature Radiation by Bunches as Emission Mechanism for Repeating Fast Radio Bursts”. In: *The Astrophysical Journal* 927.1, p. 105. DOI: [10.3847/1538-4357/ac4097](https://doi.org/10.3847/1538-4357/ac4097).
- Xu, H. et al. (Nov. 23, 2021). “A fast radio burst source at a complex magnetised site in a barred galaxy”. In: arXiv: [2111.11764](https://arxiv.org/abs/2111.11764) [astro-ph.HE].

Chapter 2

A simple relationship for the spectro-temporal structure of bursts from FRB 2020121102A¹

2.1 Observational evidence for the triggered relativistic dynamical model

Before discussing the consequences ensuing from the model introduced in Rajabi et al. (2020) and summarized in Section 1.3.4, it will be beneficial to define the terminology used to describe the spectro-temporal structure of FRBs. To do so we show in Figure 2.1 the example of Burst 11A detected in FRB 20121102A by Gajjar et al. (2018). As can be seen, four separate intensity pulses, labelled 11A1a, 11A1b, 11A2, and 11A3 in the figure, are identified. Following the literature, we will refer to these intensity features as “sub-bursts.” Likewise, there has been ample discussions of frequency drifts with arrival time

¹Material adapted from F. Rajabi, M. A. Chamma, C. M. Wyenberg, A. Mathews, & M. Houde. MNRAS, Volume 498, Issue 4, pp. 4936-4942. This chapter focuses on my contributions while the remaining material contributed by my co-authors is summarized in Section 1.3.4. Please see co-authorship statement for more details.

in the signals of repeating FRBs (Gajjar et al. 2018; Hessels et al. 2019; Josephy et al. 2019; CHIME/FRB Collaboration et al. 2019). Here, we differentiate between two kinds of frequency drifts: *i*) the relative downward drift in the central frequency of successive sub-bursts with increasing arrival time, generally referred to as the sad trombone effect, and *ii*) the steeper downward frequency drift within a single sub-burst; we define this behaviour as the “sub-burst drift.”² Both frequency drifts can be explained using our simple model.

Within the framework of the TRDM, there can be more than one FRB source located along the line-of-sight between the observer and the trigger source. It is important to note that equations the relativistic Lorentz transform equations (1) and (2) in Rajabi et al. (2020) and equations (1.16) to (1.18) apply equally well to all these sources, even in cases where they are located at different distances from the observer. That is, if two such FRB sources emit identical sub-bursts, i.e., at the same frequency ν_0 and with the same time-scales τ'_D and τ'_w in their local rest frames, their signals would be indistinguishable for the observer (i.e., they would be detected at the same time and would have the same duration) whenever the frames move at the same velocity relative to the observer. This is because the more distant FRB sources along the line of sight will burst earlier than sources that are closer. Within the context of our model, measured differences in time of arrival and duration between identical sub-bursts in the FRB source are solely due to differences in their respective velocity β relative to the observer.

2.1.1 Predictions made by the model – FRB 20121102A

Equations (1.16) to (1.19), although very simple, have profound implications. In what follows we discuss some predictions that can be drawn from them concerning the char-

²This terminology was updated to “sub-burst slope” in the following chapters in an attempt to reduce confusion in the literature between the two types of frequency drift. For this chapter “sub-burst drift” is equivalent to “sub-burst slope” in all cases and describes behaviour observed in a single sub-burst.

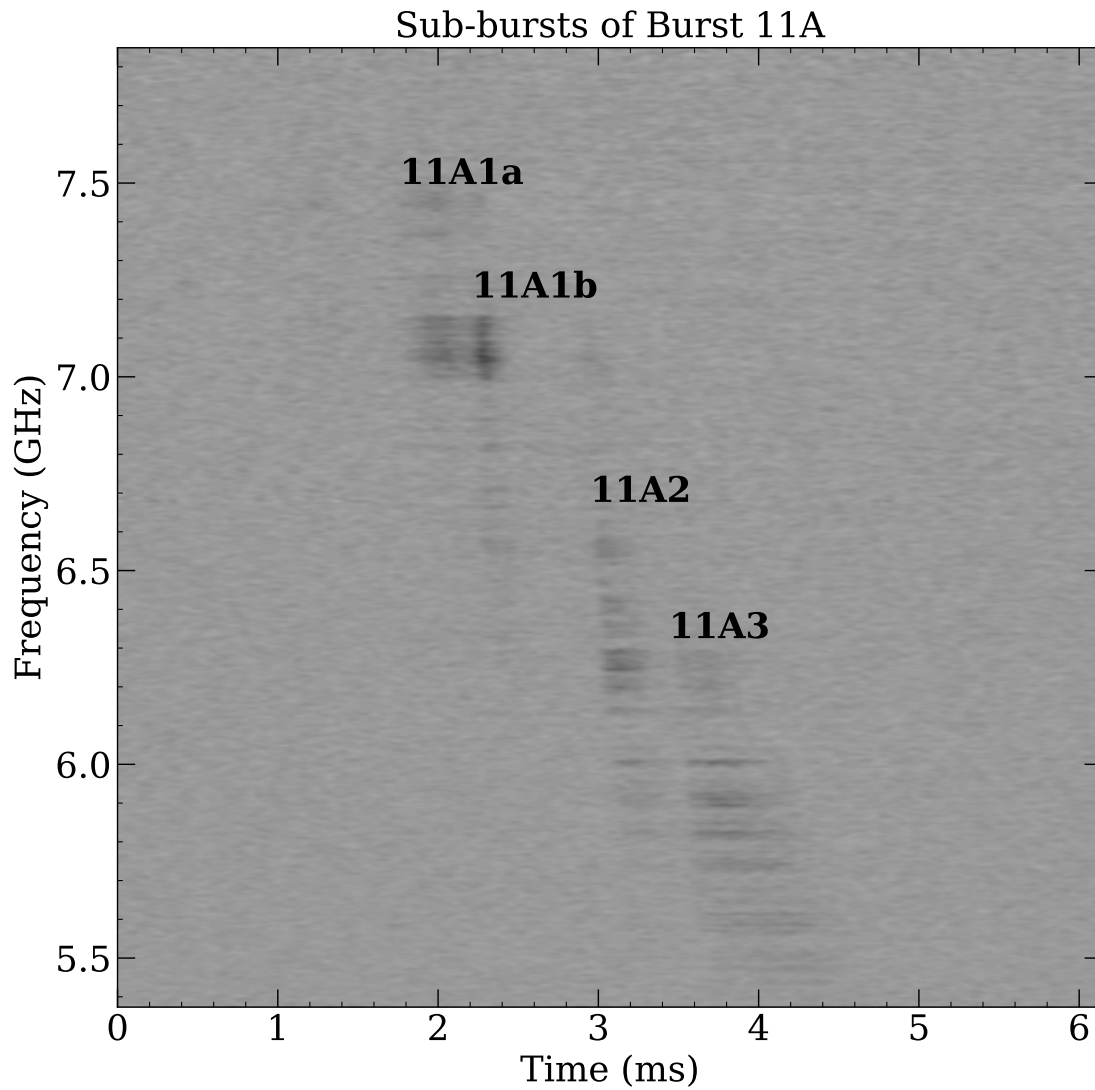


Figure 2.1: Burst 11A detected from FRB 20121102A by Gajjar et al. (2018). The different sub-bursts are identified and their relative drift is clearly seen. Many other such examples exist in the literature at different frequency bands for FRB 20121102A (e.g., Hessels et al. 2019) and other repeaters (CHIME/FRB Collaboration et al. 2019; Fonseca et al. 2020).

acteristics of FRB signals, as detected in the observer’s reference frame.

Sub-burst duration vs. frequency of observation

A readily measurable parameter of FRB pulses is their time duration. To be precise, in cases where multiple sub-bursts are detected during one event, as in Figure 2.1, we focus on the sub-burst width t_w as opposed to the duration of the whole event. Equation (1.17) clearly shows that for a given proper time-scale τ'_w and emission frequency ν_0 in the FRB rest frame one should expect shorter sub-bursts with increasing frequency of observation ν_{obs} . A similar behaviour is predicted for the observed time delay t_D (see equation 1.16). However, since the time delay cannot be unambiguously determined for a given event (i.e., the time of the trigger is unknown), it is advantageous to focus on t_w instead of t_D .

Although this behaviour is visually apparent in individual sub-bursts (see Figure 2.1), the effect should be more pronounced between observations made in different frequency bands. However, as will be seen in Sec. 2.1.1 when using the FRB 20121102A data of Michilli et al. (2018), observations at a given frequency reveal a significant spread in sub-burst durations (i.e., t_w covers a wide range of values). It follows that experimental verification of the prediction of a decrease in sub-burst duration with increasing frequency requires a significant amount of data over several frequency bandwidths. Although this complicates such a test, a decrease in sub-burst duration with increasing frequency has already been noted using comparisons of observations obtained in different frequency bands for FRB 20121102A (Gajjar et al. 2018; Hessels et al. 2019). In particular, Gajjar et al. 2018 summarize some of the past observational data on FRB 20121102A and clearly show the narrowing of signal at higher frequencies in their Figure 7b³.

³Although the decrease in burst duration with increasing ν_{obs} is clearly visible in Figure 7b of Gajjar et al. (2018), the effect is likely more pronounced than seen there as the authors do not measure the sub-burst duration t_w but rather the duration of the whole event. This provides an upper limit for t_w , especially at higher frequencies where multiple sub-bursts are more likely to be detected (as in Figure 2.1).

Sub-burst drift vs. sub-burst duration

We now discuss a striking feature that can be extracted from the dynamic spectra of FRB signals from repeaters, either from lone bursts or individual sub-bursts. More precisely, we focus on the variation in frequency with time within a given sub-burst, which, as mentioned earlier, we refer to as sub-burst drift. This feature is not to be confused with the sad trombone effect to be discussed later, which, as previously mentioned, concerns the relative drift of the central frequency in a sequence of sub-bursts. The slope of the sub-burst drift is more pronounced than that observed for the sad trombone (see Figure 2.1).

We define the sub-burst drift as the corresponding slope $d\nu_{\text{obs}}/dt_{\text{D}}$ observed in the dynamic spectrum of a signal. As mentioned in Section 1.3.4, we can find an expression for this quantity by setting $\Delta\tau'_{\text{D}} = 0$ in equation (1.19) (i.e., focusing on a single sub-burst) and thus obtain

$$\begin{aligned} \frac{d\nu_{\text{obs}}}{dt_{\text{D}}} &= -\frac{\nu_{\text{obs}}}{t_{\text{D}}} \\ &= -\left(\frac{\tau'_{\text{w}}}{\tau'_{\text{D}}}\right)\frac{\nu_{\text{obs}}}{t_{\text{w}}}, \end{aligned} \quad (2.1)$$

for the slope at the beginning of the sub-burst. The ratio of equations (1.16) and (1.17) was used for the last relation. This was done because t_{w} is readily measurable from the data while, as mentioned earlier, the delay time t_{D} is not known in the absence of the trigger signal.

Equation (2.1) predicts that for a given frequency ν_{obs} , the sub-burst drift scales inversely with its time duration t_{w} . To verify this behaviour, we have extracted $d\nu_{\text{obs}}/dt_{\text{D}}$ and t_{w} from some data available for FRB 20121102A. More precisely, both quantities were quantified using the autocorrelation function technique introduced by Hessels et al. (2019)

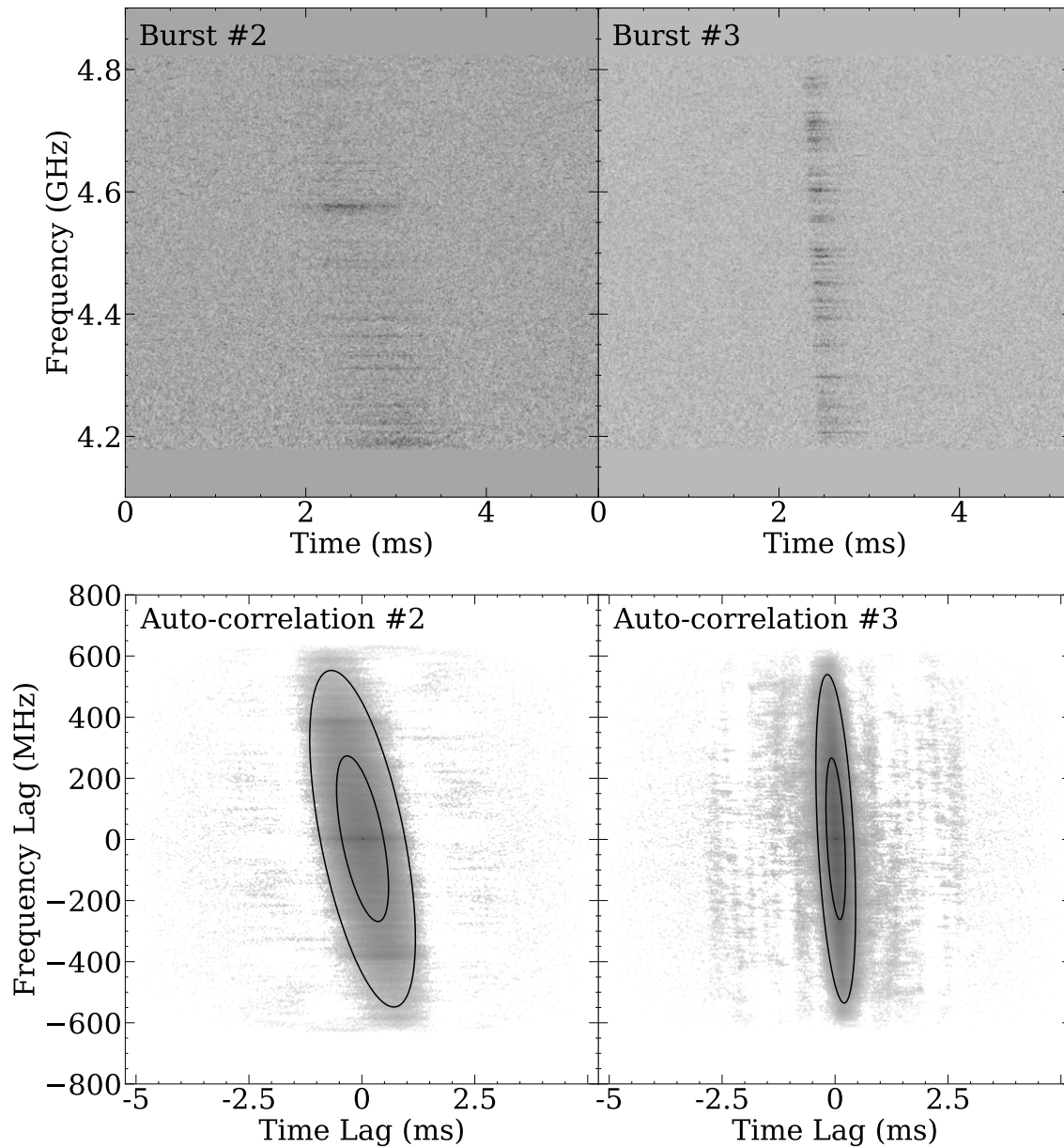


Figure 2.2: (*Top*) Dynamic spectra of Bursts #2 and #3 from Michilli et al. (2018) with (*bottom*) their two-dimensional autocorrelation functions (Hessels et al. 2019). The contours plotted on each autocorrelation function are for the one- and two-standard deviation levels of a two-dimensional Gaussian fit. The corresponding sub-burst drifts for #2 and #3 are -741 MHz/ms and -2824 MHz/ms, respectively. Note how the steeper slope for Burst #3 corresponds to a shorter sub-burst duration.

on the dynamic spectra presented in Michilli et al. (2018), Gajjar et al. (2018) (only Bursts 11A (and its sub-bursts) and 11D) and Josephy et al. (2019) (one CHIME/FRB detection centred at ~ 630 MHz). We show two examples taken from the Michilli et al. 2018 data in Figure 2.2. In all cases the autocorrelation (bottom panels) of the dynamic spectrum (top panels) was fitted to a two-dimensional Gaussian function, where the orientation of the minor and major axes relative to the vertical and horizontal axes reveal the sub-burst drift $d\nu_{\text{obs}}/dt_{\text{D}}$ while the intersection of the one-standard deviation contour with the horizontal axis provides us with an estimate of the duration t_{w} . The behaviour predicted by equation (2.1) can be clearly seen in these examples, i.e., the shorter pulse having a steeper slope $d\nu_{\text{obs}}/dt_{\text{D}}$.

Our results are summarized in Figure 2.3, where we plot $|d\nu_{\text{obs}}/dt_{\text{D}}|$ vs. t_{w} on logarithmic scales for all the data published in Michilli et al. (2018) (red circles), as well as that from Gajjar et al. (2018) (teal diamonds) and Josephy et al. (2019) (blue square, one datum). Whenever possible we identified and separated sub-bursts within a dynamic spectrum (as shown in Figure 2.1 for Burst 11A of Gajjar et al. 2018) and ran the two-dimensional autocorrelation analysis separately on each feature. Although it was at times difficult to determine when and where should such a procedure be applied, the systematic temporal narrowing of sub-bursts with steeper drifts is clearly seen in the data. The solid red curve in the figure is the result of a fit of the type $|d\nu_{\text{obs}}/dt_{\text{D}}| = A\nu_{\text{obs}}/t_{\text{w}}$ to the Michilli et al. (2018) data alone (i.e., $\nu_{\text{obs}} = 4.47$ GHz, see below), where we find $A = \tau'_{\text{w}}/\tau'_{\text{D}} \simeq 0.1$.

It should be noted that since the relation between $d\nu_{\text{obs}}/dt_{\text{D}}$ and t_{w} also depends on ν_{obs} (see equations 1.17 and 2.1), one needs to scale data points obtained at different frequencies in order to meaningfully compare them. More precisely, insertion of equation (1.17) in equation (2.1) shows that $d\nu_{\text{obs}}/dt_{\text{D}} \propto \nu_{\text{obs}}^2/\nu_0$, while $t_{\text{w}} \propto \nu_0/\nu_{\text{obs}}$. If we assume that data obtained in different frequency bands (e.g., ~ 4.5 GHz for Michilli et al. 2018,

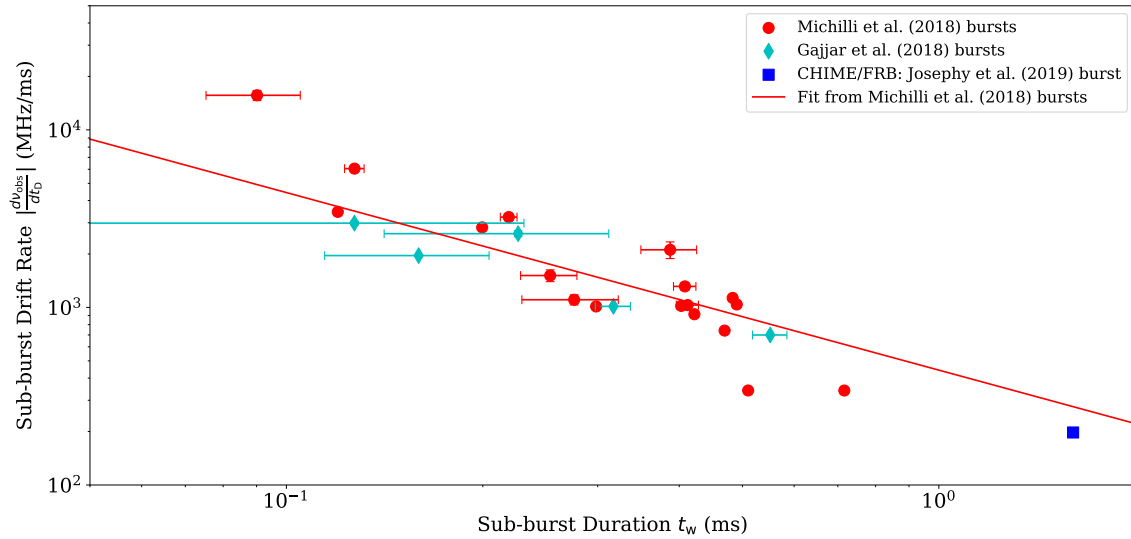


Figure 2.3: A plot of $|d\nu_{\text{obs}}/dt_{\text{D}}|$ vs. t_w on logarithmic scales for the data of Michilli et al. (2018) (red circles), Gajjar et al. (2018) (teal diamonds; only Bursts 11A (and its sub-bursts) and 11D) and Josephy et al. (2019) (blue square; one datum). These parameters were extracted using the two-dimensional autocorrelation technique of Hessels et al. (2019). The solid red curve is for the fit $|d\nu_{\text{obs}}/dt_{\text{D}}| = A\nu_{\text{obs}}/t_w$ on the Michilli et al. (2018) data (i.e., $\nu_{\text{obs}} = 4.47$ GHz); $A \simeq 0.1$. The Gajjar et al. (2018) and Josephy et al. (2019) data were scaled according to their frequency of observations relative to the Michilli et al. (2018) data (see text). Error bars shown only account for uncertainties derived from the underlying Gaussian fit and do not reflect uncertainties caused by, for example, de-dispersion of the data.

$\sim 6\text{--}8$ GHz for Gajjar et al. 2018 and $\sim 600\text{--}700$ MHz for Josephy et al. 2019) were emitted at the same frequency ν_0 in their respective rest frames, then we must choose one data set as a reference (we selected the Michilli et al. 2018 data set for this) and calibrate the others against it for direct comparison. For example, the sub-burst drifts for the Gajjar et al. (2018) data were scaled down through a multiplication by $(\nu_M/\nu_G)^2$ and their duration scaled up by ν_G/ν_M , with ν_M and ν_G the centre frequencies for the Michilli et al. (2018) and Gajjar et al. (2018) sub-bursts, respectively. We adopted a single frequency $\nu_M = 4.47$ GHz for all the Michilli et al. (2018) sub-bursts, while we adjusted ν_G for those from Gajjar et al. (2018) to match the observed frequencies. The same process was applied for the CHIME/FRB datum centred at ~ 630 MHz (Josephy et al. 2019). The fact that three sets of data, spanning more than a decade in frequency, appear to follow the same law for their respective sub-burst drifts in Figure 2.3 is significant. As we will discuss in Sec. 2.2, it is strong evidence in favour of having a single rest frame frequency of emission ν_0 for all sub-bursts detected regardless of the frequency of observation.

Relative drift between sub-bursts – the sad trombone

In cases when multiple sub-bursts are present in signals from repeating FRBs, it is often observed that the characteristic frequency tends to drift downward with increasing arrival time. This relative frequency drift between sub-bursts, i.e., the sad trombone effect, is contained in equation (1.19) of our model. More precisely, it is accounted for through the second term on the right-hand side of this equation, which describes the expected difference in arrival time for sub-bursts of varying proper time delay τ'_D . Focusing on this term only, and allowing for a dependency in the proper delay time with the local velocity within the FRB source (and thus with the observed frequency ν_{obs}) we write

$\Delta\tau'_D = \Delta\nu_{\text{obs}} d\tau'_D/d\nu_{\text{obs}}$ and find

$$\frac{\Delta\nu_{\text{obs}}}{\Delta t_D} = \frac{\nu_{\text{obs}}}{\nu_0} \frac{d\nu_{\text{obs}}}{d\tau'_D}, \quad (2.2)$$

where we also used equation (1.16). The “ Δ ” notation is used here to distinguish this effect from the sub-burst drift discussed in Sec. 2.1.1.

Equation (2.2) shows that the sign of the relative frequency drift depends on the parameter $d\nu_{\text{obs}}/d\tau'_D$. Whenever $d\nu_{\text{obs}}/d\tau'_D < 0$ the relative drift will be descending (i.e., of negative slope) with the arrival of sub-bursts, leading to the appearance of the sad trombone effect in the corresponding dynamic spectrum. As sub-bursts arrive over time, their central frequency drifts to lower values. This behaviour has already been observed for FRB 20121102A and other repeating FRBs (CHIME/FRB Collaboration et al. 2019; Fonseca et al. 2020). Salient examples of this feature can be clearly seen for Burst 11A of Gajjar et al. (2018) shown in Figure 2.1, as well as in other observations of FRB 20121102A (Hessels et al. 2019).

On the other hand, whenever $d\nu_{\text{obs}}/d\tau'_D > 0$ the opposite behaviour is expected (i.e., a “happy trombone” feature). It is interesting to note that such a behaviour has recently been observed in the FRB-like emission detected in the direction of the Galactic magnetar SGR 1935+2154 (Scholz and CHIME/FRB Collaboration 2020; CHIME/FRB 2020) and also for FRB 190611 (Day et al. 2020).

Most importantly, equation (2.2) also predicts that the relative frequency drift should be more pronounced with increasing frequency of observation ν_{obs} , for a fixed rest frame frequency of emission ν_0 . This has already been verified for FRB 20121102A by Hessels et al. (2019) through comparison of the relative sub-burst drift for measurements obtained from approximately 1–8 GHz; see their Figure 3 (top left and right panels). For example, their analysis (Fig. 3, right panel) indicates a frequency drift that is approximately four times stronger at ~ 6.5 GHz than at ~ 2 GHz (i.e., ~ -800 MHz/ms vs. \sim

-200 MHz/ms). This is consistent with the behaviour predicted by equation (2.2) under the assumption of a common rest frame frequency of emission ν_0 and parameter $d\nu_{\text{obs}}/d\tau'_{\text{D}}$ for all observations.

2.2 Discussion and summary

As we have seen in the previous section, our dynamical model, despite its simplicity, makes predictions that are verified using data available for FRB 20121102A. Perhaps most strikingly, it reveals a close relationship between the sub-burst drift and duration. For FRB 20121102A this last prediction is corroborated with the results presented in Figure 2.3. Significantly, we once again emphasize the fact that the fit to the data based on equation (2.1) was performed on those from Michilli et al. (2018) alone while the other data from Gajjar et al. (2018) and Josephy et al. (2019) were found to agree remarkably well with it. As we mentioned earlier, the fact that data sets covering more than a decade in frequency behave in a consistent manner is an important clue to the nature of the physical process underlying FRB signals in this source. Indeed, this agreement makes it difficult to imagine how these data could have resulted from emission taking place at different frequencies in their corresponding rest frames. This statement rests on the relationship between the sub-burst drift $d\nu_{\text{obs}}/dt_{\text{D}}$ and duration t_{w} through the frequency of emission ν_0 in the FRB rest frame, as implied by equations (1.17) and (2.1). In other words, it would not be possible for the three data sets to share the same law (i.e., the fit in Figure 2.3) linking these two parameters if they did not also share the same frequency ν_0 .

As far as we can tell from available data, practically all sub-bursts from repeating FRBs can have an associated frequency drift. For the FRB 20121102A data used for our analysis the extent of the frequency drift can range from 0.3 GHz to 2 GHz, but it is difficult to be specific because sometimes the (sub-)burst extends beyond the obser-

vational frequency bandwidth. Once a dispersion measure (DM) is chosen and as long as all the sub-bursts are de-dispersed to the same DM, the existence of a relationship between the sub-burst drift and duration is independent of the DM. Although applying a de-dispersion with a greater or lesser DM will certainly change the drift accordingly within a set of sub-bursts, the relative importance of the drift from one sub-burst to the other is preserved. For bursts from non-repeaters the prevalence of sub-burst drifts is difficult to assess because the de-dispersion is purposefully done so that the frequency drift (proportional to ν_{obs}^{-2}) is removed (there are no sub-burst trains from non-repeaters, so it is not possible to implement a de-dispersion that optimizes the structure of the burst as is often done for repeaters).

The earlier comment concerning a unique frequency ν_0 also applies for the sad trombone effect common to several FRBs, including FRB 20121102A (see Figure 2.1). As mentioned earlier, the measured frequency drift between sub-bursts scales approximately linearly with the observed frequency ν_{obs} (see top panels in Figure 3 of Hessels et al. (2019)). Based on equation (2.2), our model predicts the slope of the relative drift $\Delta\nu_{\text{obs}}/\Delta t_{\text{D}}$ with observed frequency ν_{obs} to vary linearly with the parameter $d\nu_{\text{obs}}/d\tau'_{\text{D}}$ and inversely with the rest frame frequency of emission ν_0 . It follows that, similarly to the case of sub-burst frequency drift discussed above, the observed behaviour is most easily explained if we are in the presence of a narrow-band emission process at frequency ν_0 in all FRB rest frames. The functionality of the two effects, i.e., the sub-burst drift and the sad trombone, with the observed frequency ν_{obs} provides strong evidence in favour of such a scenario.

Superradiance is characterized by a single time-scale T_{R} , which sets the duration τ'_{w} of the superradiance pulse and τ'_{D} the time delay before its emergence, which is needed for coherence to be established in the radiating gas. This characteristic time-scale is proportional to the spontaneous emission time-scale of the underlying molecular or atomic transition, and varies inversely with the (square of the) wavelength of the

radiation and the column density of the inverted population. In general, τ'_D is expected to be approximately one and two orders of magnitude larger than the pulse duration and T_R , respectively, in superradiant astronomical systems (Rajabi et al. 2019; Rajabi et al. 2020). This is consistent with the results of the fit shown in Figure 2.3, which implies $\tau'_w \simeq 0.1\tau'_D$.

We also note that we did not consider the potential effects of scintillation and scattering on the relationships derived in our analysis (see Section 1.1.2). Although these phenomena can affect the temporal and spectral structures of FRB signals as they propagate from the sources to the observer, it is not clear, however, how they could alter the relationship between the sub-burst drift and duration, for example. The results obtained (e.g., see Figure 2.3) seem to imply that they do not for FRB 20121102A. Accordingly, we also note that it has been previously observed that some detected pulses for FRB 20121102A did not display obvious signs of scintillation and scattering (Scholz et al. 2016).

Finally, while our model's primary objective was to explain the spectro-temporal structure common to FRB 20121102A and other repeating FRBs, it is likely to have a broader reach in its applicability. That is, it will be instructive to verify if the law linking the sub-burst drift and duration given in equation (2.1) is widely observed in other FRBs. Such a potentially universal behaviour among FRBs would be extremely helpful to improve our understanding of the physical processes underlying this phenomenon, as well as being highly constraining for existing and future models.

Acknowledgements

M.H.'s research is funded through the Natural Sciences and Engineering Research Council of Canada Discovery Grant RGPIN-2016-04460. M.H. is grateful for the hospitality of Perimeter Institute where part of this work was carried out. F.R.'s research at Perimeter

Institute is supported in part by the Government of Canada through the Department of Innovation, Science and Economic Development Canada and by the Province of Ontario through the Ministry of Economic Development, Job Creation and Trade. F.R. is in part financially supported by the Institute for Quantum Computing. M.A.C. is grateful to Victor Tranchant whose data loading and noise removal code was the starting point for the analysis pipeline. A.M. and C.M.W. are supported by the Natural Sciences and Engineering Research Council of Canada (NSERC) through the doctoral postgraduate scholarship (PGS D).

Data Availability Statement

The data pipeline is made available and maintained by M.A.C. at <https://github.com/mef51/sadtrombone>. Aggregate data of the bursts and the code for the figures are also available. Data of the FRB spectra are available either publicly or via the authors of their respective publications. The figures in this paper were prepared using the `matplotlib` package (Hunter 2007).

Bibliography

- CHIME/FRB (2020). “Periodic activity from a fast radio burst source”. In: *Nature* 582.7812, pp. 351–355. DOI: [10.1038/s41586-020-2398-2](https://doi.org/10.1038/s41586-020-2398-2).
- CHIME/FRB Collaboration Andersen, BC et al. (2019). “CHIME/FRB Discovery of Eight New Repeating Fast Radio Burst Sources”. In: *ApJ* 885.1, p. L24.
- Day, Cherie K. et al. (May 27, 2020). “High time resolution and polarisation properties of ASKAP-localised fast radio bursts”. In: arXiv: <http://arxiv.org/abs/2005.13162v1> [astro-ph.HE]. URL: <https://arxiv.org/abs/2005.13162>.
- Fonseca, E. et al. (Mar. 2020). “Nine New Repeating Fast Radio Burst Sources from CHIME/FRB”. In: *ApJ* 891.1, L6, p. L6. DOI: [10.3847/2041-8213/ab7208](https://doi.org/10.3847/2041-8213/ab7208).
- Gajjar, V. et al. (2018). “Highest Frequency Detection of FRB 121102 at 4–8 GHz Using the Breakthrough Listen Digital Backend at the Green Bank Telescope”. In: *The Astrophysical Journal* 863.1, p. 2. DOI: [10.3847/1538-4357/aad005](https://doi.org/10.3847/1538-4357/aad005).
- Hessels, J. W. T. et al. (2019). “FRB 121102 Bursts Show Complex Time–Frequency Structure”. In: *The Astrophysical Journal* 876.2, p. L23. DOI: [10.3847/2041-8213/ab13ae](https://doi.org/10.3847/2041-8213/ab13ae).
- Hunter, John D. (May 2007). “Matplotlib: A 2D Graphics Environment”. In: *Computing in Science and Engineering* 9.3, pp. 90–95. DOI: [10.1109/MCSE.2007.55](https://doi.org/10.1109/MCSE.2007.55). URL: <https://ui.adsabs.harvard.edu/abs/2007CSE.....9...90H>.

- Josephy, A. et al. (Sept. 2019). “CHIME/FRB Detection of the Original Repeating Fast Radio Burst Source FRB 121102”. In: *ApJ* 882.2, L18, p. L18. DOI: [10.3847/2041-8213/ab2c00](https://doi.org/10.3847/2041-8213/ab2c00). arXiv: [1906.11305](https://arxiv.org/abs/1906.11305) [[astro-ph.HE](#)].
- Michilli, D. et al. (2018). “An extreme magneto-ionic environment associated with the fast radio burst source FRB 121102”. In: *Nature* 553.7687, pp. 182–185. DOI: [10.1038/nature25149](https://doi.org/10.1038/nature25149).
- Rajabi, F. et al. (2019). “New evidence for Dicke’s superradiance in the 6.7 GHz methanol spectral line in the interstellar medium”. In: *MNRAS* 484.2, pp. 1590–1597. DOI: [10.1093/mnras/stz074](https://doi.org/10.1093/mnras/stz074). arXiv: [1810.04365](https://arxiv.org/abs/1810.04365) [[astro-ph.GA](#)].
- Rajabi, Fereshteh et al. (2020). “A simple relationship for the spectro-temporal structure of bursts from FRB 121102”. In: *Monthly Notices of the Royal Astronomical Society* 498.4, pp. 4936–4942. DOI: [10.1093/mnras/staa2723](https://doi.org/10.1093/mnras/staa2723).
- Scholz, P. et al. (Dec. 2016). “The Repeating Fast Radio Burst FRB 121102: Multi-wavelength Observations and Additional Bursts”. In: *ApJ* 833, 177, p. 177. DOI: [10.3847/1538-4357/833/2/177](https://doi.org/10.3847/1538-4357/833/2/177). arXiv: [1603.08880](https://arxiv.org/abs/1603.08880) [[astro-ph.HE](#)].
- Scholz, Paul and CHIME/FRB Collaboration (Apr. 2020). “A bright millisecond-timescale radio burst from the direction of the Galactic magnetar SGR 1935+2154”. In: *Astron. Telegram* 13681, p. 1.

Chapter 3

Evidence of a shared spectro-temporal law between sources of repeating fast radio bursts¹

3.1 Introduction

Fast radio bursts (FRBs) are short duration (\sim millisecond) bursts of energy at radio wavelengths exhibiting large brightness temperatures ($T_B > 10^{32}$ K; Lorimer et al. 2007; Petroff, Hessels, and Lorimer 2019), suggesting that these signals originate from non-thermal objects through some coherent emission mechanism. Still, the origin and underlying physical mechanism of FRBs remain unknown in spite of the large number of proposed models (Platts et al. 2019). FRB signals also undergo a high level of dispersion as they propagate from the source to the observer, a phenomenon quantified through the dispersion measure (DM). This dispersion results from the wavelength dependence of the

¹M. A. Chamma, F. Rajabi, C. M. Wyenberg, A. Mathews, & M. Houde. MNRAS, Volume 507, Issue 1, October 2021, Pages 246–260.

refractive index of ionized matter in astronomical media through which radiation travels at varying speeds as a function of frequency. While a first Galactic FRB was recently reported by the CHIME/FRB Collaboration and the STARE2 team toward the Galactic magnetar SGR 1935+2154 (The CHIME/FRB Collaboration et al. 2020; Bochenek et al. 2020), the DM values measured for most FRBs suggest that these signals must emanate from extragalactic sources.

Reported FRBs fall into two groups: one-off events and repeaters. While one-off events form the majority of detections, most of our knowledge about FRBs is based on the study of repeaters. At the time of writing, two repeaters (FRB 20121102A and FRB 20180916B, previously known as FRB 121102 and FRB 180916.J0158+65) show periodic behaviours, prompting continued follow-up observations (CHIME/FRB et al. 2020; Rajwade et al. 2020). Importantly, the study of dynamic spectra of repeaters reveals interesting patterns. Among these are a downward drift in the central frequency of consecutive sub-bursts with increasing arrival time within an event (the so-called “sad trombone” effect), and an average reduction in the temporal duration of individual sub-bursts with increasing frequency (Gajjar et al. 2018; Hessels et al. 2019; CHIME/FRB et al. 2019; Josephy et al. 2019).

Several models have been proposed to explain these spectro-temporal characteristics. Some models link these characteristics to the intrinsic radiation mechanism of FRBs (Wang et al. 2019; Beloborodov 2020; Metzger, Margalit, and Sironi 2019) or propagation effects (e.g., plasma lensing in Cordes et al. 2017 or scintillation in Simard and Ravi 2020), while others argue that a combination of both factors can play a part (Hessels et al. 2019). Recently, the detection of the first Galactic FRB (The CHIME/FRB Collaboration et al. 2020; Bochenek et al. 2020) has posed new challenges for existing theoretical models. For example, one sequence of sub-bursts detected toward this source reveals an upward central frequency drift with increasing arrival time (a “happy trombone” effect; see Burst 6 of Hilmarsson et al. 2021, bursts 24 and 25 in CHIME/FRB et al. 2020 and FRB 190611

in Day et al. 2020 for other examples). A few models have anticipated such a possibility for the spectra of FRBs (Simard and Ravi 2020; Rajabi et al. 2020; Beniamini and Kumar 2020). In particular, Rajabi et al. (2020) proposed a simple dynamical relativistic model where a descending or an ascending central frequency drift for a sequence of sub-bursts can be explained based on the intrinsic properties of the corresponding FRB source (as discussed in Section 3.1.1 and Appendix 2.B). But more importantly, their model also predicts that a steeper frequency drift should be present within individual sub-bursts (henceforth the “sub-burst slope”²) where the slope of the FRB signal as displayed in a waterfall (i.e., the signal intensity as a function of frequency and time) obeys a simple law scaling inversely with the temporal duration of the sub-burst. Rajabi et al. (2020) further provided evidence for this sub-burst slope behaviour for FRB 20121102A and showed that data taken over a wide range of frequencies for this repeater follow the same law, i.e., the aforementioned inverse scaling of the sub-bursts slope with their corresponding temporal duration. They then argued that this finding implies that the underlying physical process responsible for the signals detected in FRB 20121102A is intrinsically narrow-band in nature, while relativistic motions within the source are required to explain the wide observed bandwidths.

In this paper, we examine data from two additional repeaters, FRB 20180814A (initially named FRB 180814.J0422+73; CHIME/FRB et al. 2019) and FRB 20180916B (CHIME/FRB Collaboration et al. 2019; CHIME/FRB et al. 2020), and show that this form of law is closely shared between these three FRBs originating from host galaxies at different redshifts. We also consider the effect of the chosen DM on the measurements of the sub-burst slope and the temporal duration in order to understand the robustness of

²We denote an FRB event or burst as containing one lone or many pulses of radiation, as is observed for the so-called sad trombone effect, for example. A single pulse in an event containing several pulses will be defined as a sub-burst. Rajabi et al. 2020 used the term “sub-burst drift” to describe the observed signal delay t_D as a function of the measured frequency ν_{obs} within an individual sub-burst (as in equation (3.1)). However, since this term is also sometimes found in the literature to denote delays between separate sub-bursts (as in the sad trombone effect), we will instead opt for “sub-burst slope” to describe the internal drift within an individual sub-burst to avoid any possible confusion.

this relationship between the sources. Section 3.1.1 summarizes the triggered dynamical model that motivates this analysis. Section 3.2 describes the details of the analysis and the handling of the DM for each burst from each source. In Section 3.3 we highlight the results and discuss the implications of unresolved bursts in our sample, the effect of variations in DM on a measurement of sub-burst slope or drift, and finally explore physical interpretations of our result in the context of the triggered dynamical model. This finding reveals new insights on the underlying physical mechanism at the source of FRB signals and helps refine modelling and characterization efforts.

3.1.1 The triggered dynamical model of Rajabi et al. (2020)

Rajabi et al. (2020) introduced a simple dynamical model where a triggering source (e.g., a pulsar or magnetar; see Houde et al. 2019) is located directly behind an FRB source as seen by an observer. An FRB source may contain one or many sub-regions moving towards (or away from) the observer, potentially at relativistic speeds, and from which individual sub-burst signals are emanating. Such a scenario is appropriate for situations where the emitted signal is highly collimated, such as is the case for a radiation process based on Dicke’s superradiance which the FRB model proposed by Rajabi et al. 2020 is ultimately inspired by (Rajabi and Houde 2016a,b, 2017; Mathews 2017; Houde and Rajabi 2018; Houde et al. 2019; Rajabi et al. 2019; Rajabi et al. 2020). Under such conditions it can be shown that the slope of a single sub-burst signal (for repeaters an event can contain several sub-bursts) obeys the following relation

$$\frac{1}{\nu_{\text{obs}}} \frac{d\nu_{\text{obs}}}{dt_{\text{D}}} = -\frac{A}{t_{\text{w}}}, \quad (3.1)$$

where ν_{obs} , t_{w} and t_{D} are the frequency, the temporal duration of the sub-burst and the delay before its appearance (in relation to the arrival of the trigger) as measured by the observer. The systemic parameter $A \equiv \tau'_{\text{w}}/\tau'_{\text{D}}$ with τ'_{w} and τ'_{D} the corresponding sub-

burst proper temporal duration and delay in the reference frame of the corresponding FRB sub-region, respectively.

Following the model of Rajabi et al. (2020), the temporal duration of an FRB sub-burst in the observer rest frame is given by

$$t_w = \tau'_w \frac{\nu_0}{\nu_{\text{obs}}}, \quad (3.2)$$

where ν_0 is frequency of emission in the FRB rest frame. Equation (3.2) clearly predicts an inverse relationship between the observed FRB temporal width and frequency, which had previously been noticed and studied. For example, a verification of this effect can be found in Figure 7(b) of Gajjar et al. (2018) for the case of FRB 20121102A³. Although the measurements of burst temporal duration exhibit a fair amount of scatter at a given frequency (which could also be inherent to τ'_w in equation (3.2)), the predicted behaviour is consistent with the observations.

Rajabi et al. (2020) also derived the following equation for the relative drift in the observed central frequency of a sequence of sub-bursts with increasing arrival time

$$\frac{\Delta\nu_{\text{obs}}}{\Delta t_{\text{D}}} = \frac{\nu_{\text{obs}}}{\nu_0} \frac{d\nu_{\text{obs}}}{d\tau'_{\text{D}}}, \quad (3.3)$$

where the term on the left-hand side is for the relative central frequency drift and τ'_{D} is the proper temporal delay between the arrival of the trigger and the emission of the ensuing sub-burst in the FRB rest frame. The derivative $d\nu_{\text{obs}}/d\tau'_{\text{D}}$ is a physical parameter characterizing the environment of the FRB source, which determines whether the sequence of sub-bursts has the appearance of a “sad” ($d\nu_{\text{obs}}/d\tau'_{\text{D}} < 0$) or “happy trombone” ($d\nu_{\text{obs}}/d\tau'_{\text{D}} > 0$; see Rajabi et al. 2020 for more details). Equation (3.3) predicts

³As noted in Rajabi et al. (2020), the temporal narrowing effect with observed frequency is likely more pronounced than seen in Figure 7(b) of Gajjar et al. (2018) as the authors do not measure the duration of individual sub-bursts t_w but rather that of the whole event. The true values for t_w are therefore likely to be lower and the sub-burst slope more pronounced in several instances.

that the central frequency drift should scale linearly with ν_{obs} , which has previously been verified for FRB 20121102A over a wide range of frequencies. This can be asserted, for example, from Figure 3 (top panels) of Hessels et al. (2019), Figure 6 of Josephy et al. (2019) and Figure 4 of Caleb et al. (2020). Extended Figure 9 of Pastor-Marazuela et al. (2021) shows the trend for FRB 20180916B. This observed dependency could not be realized if ν_0 changed significantly in equation (3.3). For example, a change of 50% in ν_0 would markedly affect the appearance of the figures.

We also note that within the context of our triggered model, individual sub-bursts belonging to a single FRB event all results from the same background trigger signal. Their sequence of appearance in time, as seen by the observer, will vary depending on the physical properties of the medium where individual sub-bursts emanate from (which will affect the delay time in the corresponding rest frame τ'_D) and its velocity β (and therefore the frequency ν_{obs} relative to the observer). Although we expect sub-bursts belonging to a single FRB event to be clustered in time, it is also possible that sub-bursts belonging to different events be observed relatively closely in time.

3.2 Burst Analysis

Although equation (3.1) was tested and verified for FRB 20121102A in Rajabi et al. (2020) using previously published data covering more than a decade in frequency (Michilli et al. 2018; Gajjar et al. 2018; Josephy et al. 2019), it was not known at the time whether it applies equally well to other repeating FRBs. We therefore retrieved and analyzed previously published data for two other sources discovered by the CHIME/FRB Collaboration (Fonseca et al. 2020), namely FRB 20180916B (CHIME/FRB et al. 2020) and FRB 20180814A (CHIME/FRB et al. 2019). These data are all contained within the CHIME/FRB spectral band (approximately 400–800 MHz) and the corresponding dynamic spectra were analyzed using the two-dimensional autocorrelation technique in-

roduced in Hessels et al. (2019), resulting in estimates for the sub-burst slope ($d\nu_{\text{obs}}/dt_{\text{D}}$) and temporal duration (t_{w}). See Appendix 2.A for more details. These data sources were chosen purely due to their ease of accessibility and the support available. Ultimately we aim to extend this analysis to as many sources and bursts as possible.

3.2.1 The effect of the Dispersion Measure (DM)

Since the measurement of any drift rate (or almost any other spectro-temporal feature) is strongly dependant on the DM that is used to dedisperse a waterfall, and since the DM of a source can potentially vary from burst to burst as well as with time, we studied the variation of our slope and temporal duration measurements for each sub-burst at different choices of DM. Dedispersion can be performed by optimizing either the signal-to-noise (S/N) or a structure parameter and can result in different values found for the DM depending on the burst (e.g. Fig 1 of Gajjar et al. 2018). In particular, an algorithm seeking to choose a DM by maximizing S/N might superimpose the individual sub-bursts of a complex FRB event and yield a DM value that is higher than a structure optimizing algorithm. For bursts with components that are not clearly resolved it becomes ambiguous which algorithm is most accurate and the precision in the DMs determined burst to burst can be much narrower than the variations in the DM observed overall for a source (CHIME/FRB et al. 2020). It therefore becomes difficult to uncouple FRB characteristics from the nature of the medium in order to study relationships between spectro-temporal features as we hope to do. One option is to use the DM found on a burst by burst basis. However, doing this can become a complicated process of verifying that the DM algorithm choice is appropriate, which will often be ambiguous for smeared bursts where it is not clear if it consists of multiple components or not. Without a detailed understanding of the emission mechanism, the medium, the source, and the resulting DM distribution as a function of time, it is in fact much simpler and more conservative to choose a DM range as wide as possible based on the history of DMs found for the source. We shall see

Source	Data source	DM Range (pc/cm ³)
FRB 20121102A	Michilli et al. 2018	554.1–565.3
FRB 20121102A	Gajjar et al. 2018	555–570 (555–583)
FRB 20180916B	CHIME/FRB et al. 2020	346.82–349.82
FRB 20180814A	CHIME/FRB et al. 2019	188.7–190.0

Table 3.1: The range of DMs used to determine the range of possible values of each sub-burst slope and duration. These are chosen to be as wide as possible while still obtaining reasonable sub-burst slope measurements. In general, the published history of DMs found for a source (all bursts considered) determines the range used, with some DMs on the higher end excluded due to resulting positive sub-burst slopes or distortion. The DM range in parentheses is used specially for Burst 11D from FRB 20121102A in Gajjar et al. 2018 due to its high S/N optimized DM. See the text for more details.

that despite the significant uncertainties this choice entails, the data still point to the existence of an inverse trend between the sub-burst slope and temporal duration for the three sources considered here.

Table 3.1 shows the DM ranges chosen for each source and dataset. We aim to consider as broad a range of DMs as possible while still obtaining reasonable sub-burst slope measurements. For the data used from Michilli et al. 2018 DM variations are estimated by those authors to be $\lesssim 1\%$ of 559.7 pc/cm³, and we therefore consider a range of 554.1–565.3 pc/cm³. For the data from Gajjar et al. 2018, due to availability, we use the sub-bursts in Burst 11A and Burst 11D. A structure optimized DM for 11A is found at 565 pc/cm³, and their Figure 1 indicates that DMs between 555–570 are also close to optimal, so we adopt this range. For Burst 11D, due to a lack of structure we consider a range of 555–583 to be closer to its S/N optimized DM, however higher DMs are excluded as the sub-burst slopes start to become positive (which are not physical according to our model and in general usually indicate overdispersion, as described in Section 3.2.2). For data from CHIME/FRB et al. 2020 on FRB 20180916B a precise DM of 348.82 ± 0.05 pc/cm³ is found for one of the bursts, but burst-to-burst the DM can range from 348.7–350.2. We therefore choose a mid-point of about 348.82 pc/cm³ and adopt a range of 346.82–349.82 pc/cm³. The lower value for the start of the range is chosen to push the limit of acceptable DMs while still obtaining reasonable sub-burst

slope measurements. We stay away from the higher end of the observed range due to the sub-burst distortion and positive slopes observed for most cases at that high of a DM. Finally, for data from CHIME/FRB et al. 2019 on FRB 20180814A, due to the structure present in the bursts, we extend the full range of structure optimized DMs found (188.9-190 pc/cm³) to 188.7-190 pc/cm³. We ignore the higher S/N optimized DMs due to the component overlap and distortion observed when dedispersing to those DMs.

For each source, we generate a grid of DMs over the range chosen and dedisperse all bursts to each DM before performing an autocorrelation analysis. The grid spacing varies from $\Delta\text{DM} \simeq 0.1\text{--}2$ pc/cm³ depending on the source, yielding approximately 10–20 trial DMs in each case. For FRB events with multiple components like Burst 11A from Gajjar et al. 2018 for FRB 20121102A, the components are separated manually by finding valleys in the corresponding time series of the data. When necessary these components are padded with a background sample of the waterfall so that there is a wide enough temporal extent to properly dedisperse the burst. Some bursts are not clearly resolved, but wherever there is indication that the slope suddenly changes mid-burst a manual attempt is made to separate the components.

The autocorrelation analysis (see Appendix 2.A) is then performed for all dedispersed waterfalls to obtain sub-burst slope and temporal duration measurements for every burst at each DM (Hessels et al. 2019). We use these data to determine the range of possible values for each measurement. Examples of a waterfall for every sub-burst used in this analysis with their corresponding autocorrelation are shown in Figures 3.6 – 3.10 at the end of the paper, displayed for one of the trial DMs. The range found for each of these measurements is much larger than the parameter uncertainty resulting from the underlying two-dimensional Gaussian fit of the autocorrelation function used to evaluate them. Since the true underlying DM distribution for each source appears to be narrower than the DM range we have used (considering the distribution so far implied by published DMs and knowing that the distribution can change with time), the range of values found

this way must be larger than the range implied by the true uncertainties for each measurement. We therefore treat the range of values found by this analysis as upper-limit estimates of the real measurement uncertainties.

3.2.2 Measurement exclusions and fitting

With the measurements for each sub-burst at all trial DMs found, there remain measurements that are unconstrained and/or non-physical that need to be discarded before fitting. As previously mentioned we discard any positive sub-burst slope measurements which are non-physical under our model, as well as measurements where the value and/or uncertainties approaches infinity, as is the case for sub-bursts that become near vertical or circular in their autocorrelation.

The result of this exclusion process is that out of a total of 41 sub-bursts analysed, we retain all the measurements made for 28 sub-bursts over the entirety of the DM ranges specified in Table 3.1. For the remaining 13 sub-bursts the measurements excluded were taken at the higher end of the DM range, since they yielded positive sub-burst slopes. For all but one of the sub-bursts treated this way the DM range is slightly further restricted. The exception being one burst from FRB 20180814A, where the DM range is limited from $188.7 - 190.0 \text{ pc/cm}^3$ to $188.8 - 188.9 \text{ pc/cm}^3$. We specifically identify (i.e., circle) these sub-bursts when displayed in Figures 3.1 and 3.5 below to indicate the smaller range of DMs used.

Using this set of sub-burst slope and temporal duration measurements we find a fit to equation (3.1) at each DM and compute the reduced- χ^2 to select a representative DM for each source (i.e., the DM with the reduced- χ^2 closest to unity). We do not perform a fit at the highest DM of 583 pc/cm^3 for FRB20121102A as Burst 11D is the only point with a valid measurement at that DM. The representative DMs found are 558.8 and 568.3 pc/cm^3 for FRB 20121102A for the data from Michilli et al. 2018 and Gajjar et al. 2018, respectively, 348.82 pc/cm^3 for FRB 20180916B and 188.8 pc/cm^3 for

FRB 20180814A.

3.3 Results and Discussion

We show in Figure 3.1 the results of our analysis, where the sub-burst slope (normalized to the frequency of observation ν_{obs}) is plotted against the temporal width t_w for the three FRBs. Normalizing the sub-burst slope has the advantage of allowing us to combine the different sources on the same graph irrespective of the frequency of observation, shifts due to the dynamical Doppler effect or cosmological redshift. Furthermore, we note that equation (3.1) is also insensitive to temporal scaling transformations. For example, interstellar scintillation, which brings a temporal broadening scaling inversely with the fourth power of the frequency, will have no effect on our analysis. The only consequence being a shift of data points along the specific law characterized by the parameter A in equation (3.1). The points displayed in Figure 3.1 are the measurements of each sub-burst obtained at the representative DM described at the end of Section 3.2.2, and the capped lines represent the range of possible measurements over the DM range considered.

Examination of Figure 3.1 reveals that the inverse relationship between the two parameters is clearly seen for all sources on the graph for values ranging over two orders of magnitude for both the normalized sub-burst slope and the temporal duration. Also shown in the figure are fits for the predicted function A/t_w (see equation (3.1)) for the three sources at their representative DMs (see end of Section 3.2.2), with $A = 0.078 \pm 0.006$, 0.082 ± 0.006 and 0.076 ± 0.013 for FRB 20121102A, FRB 20180916B and FRB 20180814A, respectively. The shaded regions for each source represent the range of fits found when considering all DMs in the adopted range. The corresponding range of fit parameters are found to be $A = 0.042 - 0.138$ for FRB 20121102A, $A = 0.032 - 0.153$ for FRB 20180916B and $A = 0.071 - 0.152$ for FRB 20180814A. These regions overlap significantly, but leave open the possibility of unique and distinct fits between the three

sources.

A few important consequences are to be noted from the results presented in Figure 3.1. First, and most importantly, the inverse relationship between the sub-burst slope and temporal duration is observed to be independent of the selection of the DM. That is, there is an unmistakable tendency for narrower sub-bursts at higher slopes, and vice-versa, irrespective of the DM chosen. Even with the ranges of measurements seen, Figure 3.1 strongly suggests each source obeys a form of equation (3.1), where we see a clear decrease in the magnitude of slopes with increasing sub-burst durations.

Second, we note the possibility that not only is the inverse relationship between the sub-burst slope and temporal duration verified for the three sources, but they do so with similar values for A in equation (3.1) at their representative DMs. The different fits to this systemic parameter are similar given their uncertainties, and it is difficult to visually distinguish between the corresponding curves. This closeness between the values obtained for A is rather remarkable and suggests the existence of a single and common underlying physical phenomenon responsible for the emission of FRB signals in the three sources. This is significant because these FRBs are associated with different types of host galaxies at various redshifts. More precisely, FRB 20121102A is localized to a low-metallicity irregular dwarf galaxy at a redshift $z = 0.193$ (Tendulkar et al. 2017), while the redshift of FRB 20180814A is estimated to be $z \leq 0.1$ (CHIME/FRB et al. 2019). Furthermore, the candidates for the host galaxy of FRB 20180814A are not consistent with those harboring long gamma-ray bursts (LGRBs) or superluminous supernovae (SLSNe), unlike the host galaxy of FRB 20121102A (Li et al. 2019). As for FRB 20180916B, it is precisely localized to a star-forming region in a massive spiral galaxy at a redshift $z = 0.0337$ (Marcote et al. 2020). This source is the closest known extragalactic FRB, whose host galaxy does not show signatures of a strong magnetic field nor a radio counterpart as reported for FRB 20121102A. The similarities in the values for A between the three sources also

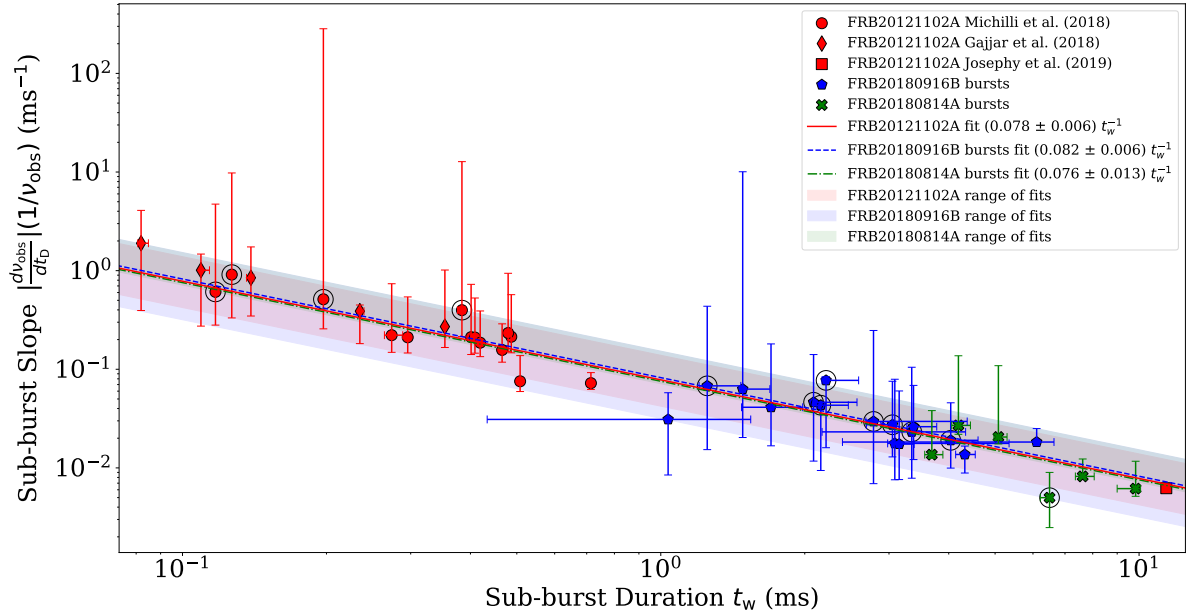


Figure 3.1: A plot of $|d\nu_{\text{obs}}/dt_D| (1/\nu_{\text{obs}})$ vs. t_w for bursts from FRB 20121102A (red circles, diamonds and square; Gajjar et al. 2018; Michilli et al. 2018; Josephy et al. 2019), FRB 20180916B (blue pentagons; CHIME/FRB et al. 2020) and FRB 20180814A (green crosses; CHIME/FRB et al. 2019). The sub-burst slope $d\nu_{\text{obs}}/dt_D$ and duration t_w were obtained using the two-dimensional autocorrelation technique of Hessels et al. (2019), while the center frequency ν_{obs} was estimated from the corresponding dynamic spectra. Each burst was dedispersed to a grid of trial DMs over the range specified by Table 3.1 and the measurements were repeated. The one point from Josephy et al. 2019 was not part of the same analysis and is shown for reference. The red, blue and green lines are for fits of the function A/t_w on the FRB 20121102A, FRB 20180916B and FRB 20180814A data, respectively, at the DM within the range of trial DMs for which the reduced- χ^2 of the fit was closest to unity, and are difficult to distinguish from one another. All points for a given source (except for the Josephy et al. 2019 datum) are of measurements made at the same DM used for the corresponding fit. The capped lines at each point represent the range of possible measurements obtained via the autocorrelation analysis for different DMs over the DM ranges chosen. As discussed in Section 3.2.1, these are used in lieu of, and are larger than, the difficult to determine true measurement uncertainties. The circled points indicate sub-bursts that required a limited DM range to constrain their measurements (see Section 3.2.2). The shaded regions represent the range of fits found when using measurements obtained at other DMs in the range. These regions overlap significantly, but indicate the possibility of unique and distinct fits between the three sources within the range of possible DMs chosen.

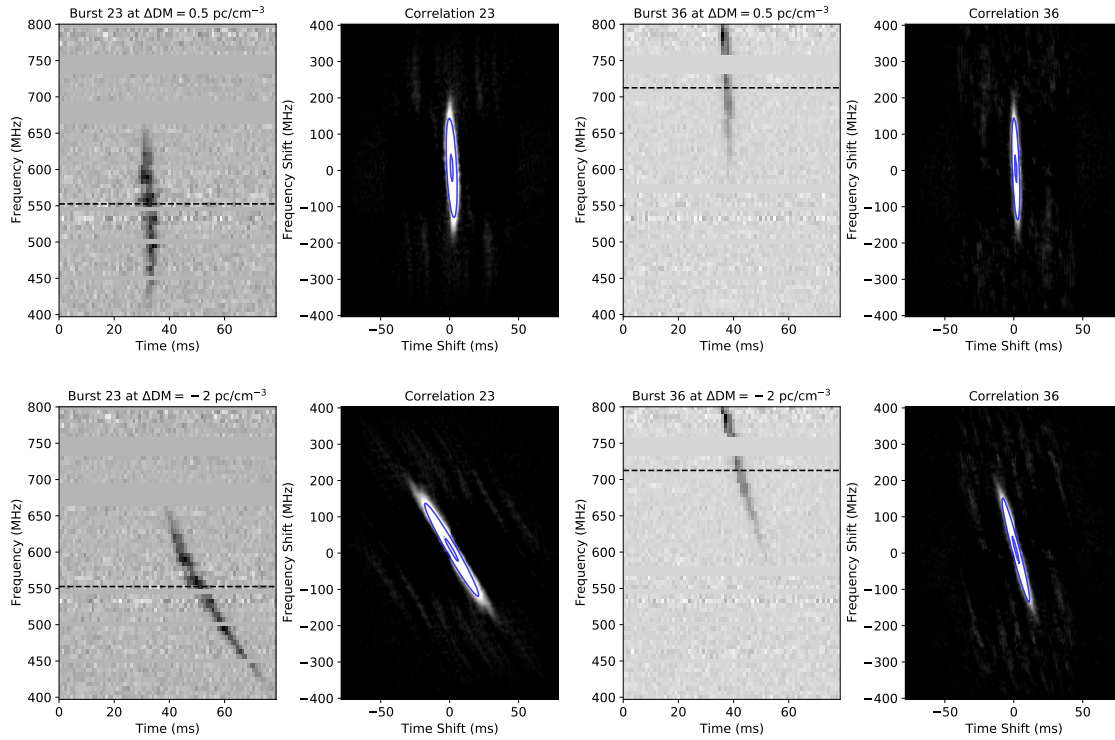


Figure 3.2: Changes to waterfalls and autocorrelations due to variations in the DM. Sub-bursts 23 (first column) and 36 (third column) for FRB 20180916B are shown with their autocorrelation functions (second and fourth columns, respectively) for two offsets $\Delta\text{DM} = 0.5 \text{ pc cm}^{-3}$ (top row) and -2 pc cm^{-3} (bottom row) from the representative value chosen for our analysis (i.e., $\text{DM} = 348.82 \text{ pc cm}^{-3}$). The rotations brought about by the small changes in DM are clearly seen in both the waterfall and autocorrelation functions. See Figure 3.8 for these bursts dedispersed to their representative DM.

suggests that the sub-burst slope law can become a suitable method for making small simplifying adjustments to the DM of waterfalls of repeating FRBs, once the dominant dispersion effects due to the interstellar and intergalactic media are accounted for. The resulting choice of DM would have the advantage of being rooted on a simple physical model resting on the relativistic nature of FRBs, and can be used to simplify analyses with large sample sizes by avoiding the complexity that can arise when choosing a DM based on the S/N or other structure criteria.

As was discussed in Rajabi et al. (2020), the three predictions made by their simple dynamical model (i.e., the narrowing of sub-bursts width t_w with increasing frequency ν_{obs} , the sad or happy trombone effect and the sub-burst slope law discussed here) provide strong evidence that the underlying physical phenomenon is narrow-band in nature. This is because the dependencies on ν_{obs} and the frequency of emission in the FRB rest frames ν_0 for the three predicted relationships are such that it would be difficult to envision how they could be realized through the data if ν_0 was allowed to vary substantially (see Section 3.3.4 for more details). Although data over a significant range of observed frequency is currently only available for FRB 20121102A (and constitutes the basis of the analysis presented in Rajabi et al. 2020), the fact that FRB 20180916B and FRB 20180814A follow the same law renders it reasonable to expect that the conclusions reached for FRB 20121102A also apply to them.

We can use this information with our model to further characterise the environment of the sources responsible for the detected bursts. Indeed using the extensive data available for FRB 20121102A one can estimate, although with limited precision at this point, the maximum Lorentz factor and the rest frame frequency of emission ν_0 . To do so we will assume highly simplified conditions, i.e., that the different FRB reference frames from which the individual sub-bursts emanate either move towards or away from the observers with the same range of speeds. We will denote by $\beta^+ > 0$ and $\beta^- = -\beta^+$ the maximum velocities (divided by the speed of light) towards and away from the observer, respectively,

with corresponding observed frequencies ν_{obs}^{\pm} . It is then straightforward to show that, under this assumption,

$$\beta^+ = \frac{\nu_{\text{obs}}^+ - \nu_{\text{obs}}^-}{\nu_{\text{obs}}^+ + \nu_{\text{obs}}^-} \quad (3.4)$$

$$\nu_0^2 = \nu_{\text{obs}}^+ \nu_{\text{obs}}^- \quad (3.5)$$

Using $\nu_{\text{obs}}^+ \simeq 7.5$ GHz and $\nu_{\text{obs}}^- \simeq 630$ MHz we find $\beta^+ \approx 0.9$ and $\nu_0 \approx 2.6$ GHz for FRB 20121102A (taking into account its known redshift $z = 0.193$ from Tendulkar et al. 2017; see Section 3.3.4 for more details). Evidently, the accuracy for these estimates is set and limited by the frequency coverage of the existing data and is likely to change as more detections are acquired. For example, confirming the purported detection of signals at 111 MHz from Fedorova and Rodin (2019) would further increase β^+ and bring down ν_0 on the order of 1 GHz. At any rate, these results imply that FRB 20121102A is potentially very strongly relativistic.

We also know that the spectral width $\Delta\nu_{\text{obs}}$ associated to individual sub-bursts for FRB 20121102A scales as $\Delta\nu_{\text{obs}} \sim 0.16 \nu_{\text{obs}}$ on average (see Figure 6 in Rajabi et al. 2020 or Figure 5 in Houde et al. 2019). This spectral extent is the result of motions (through the Doppler effect) within a given FRB rest frame from where a sub-burst centred at ν_{obs} originates. As discussed in Appendix 2.B, the observed spectral width is constrained through

$$2\Delta\beta' \leq \frac{\Delta\nu_{\text{obs}}}{\nu_{\text{obs}}} \leq \frac{2\Delta\beta'}{1 - \Delta\beta'^2}, \quad (3.6)$$

where the motions in the FRB rest frame are contained within $\pm\Delta\beta'$. We thus find $\Delta\beta' \sim 0.08$ with equation (3.6) for this source.

We thus have a picture where FRB 20121102A and similar sources would consist of systems within which a number of spatially distinct FRB rest frames, whose motions

cover a wide range of velocities (some highly relativistic relative to the observer; $|\beta| \lesssim 0.9$ for FRB 20121102A), are responsible for the emission of individual sub-bursts. In turn, each such rest frame is also host to mildly relativistic motions ($|\Delta\beta'| \lesssim 0.08$ for FRB 20121102A), which are responsible for the observed wide spectral widths of sub-bursts.

In the following sections we discuss the the ambiguity between slope and drift rate measurements that arises when sub-bursts are unresolved, the effect of DM variations on the autocorrelation of waterfalls, as well as the effects of noise and missing data on the measurement of the sub-burst slope and temporal duration. We also further discuss the determination of physical parameters of the source.

3.3.1 Unresolved bursts and slope vs. drift rate ambiguity

In practice it is difficult to be certain whether an FRB is resolved in time or not, and in several cases the difference between sub-burst slope and sub-burst drift measurements is ambiguous. For example, the waterfall of an unresolved pulse train will go through our analysis and produce a sub-burst slope measurement, while it is, in fact, a sub-burst drift rate measurement. While, as mentioned earlier, we make every effort to separate FRBs into distinct sub-bursts, it will be impossible to do this with bursts that may have originally been composed of multiple components but appear completely unresolved in the data. Here, we discuss ways through which an FRB becomes unresolved and the connection between the sub-burst slope and sub-burst drift rate measurements within the context of our model.

An FRB that was emitted as distinct components in time can appear unresolved in data either through a limited time resolution (e.g., Fig. 1 of both Michilli et al. 2021 and Bhardwaj et al. 2021), intrachannel smearing from incoherent dedispersion, limited S/N (e.g., Fig. 7 of Gourdji et al. 2019), and the blending of components through

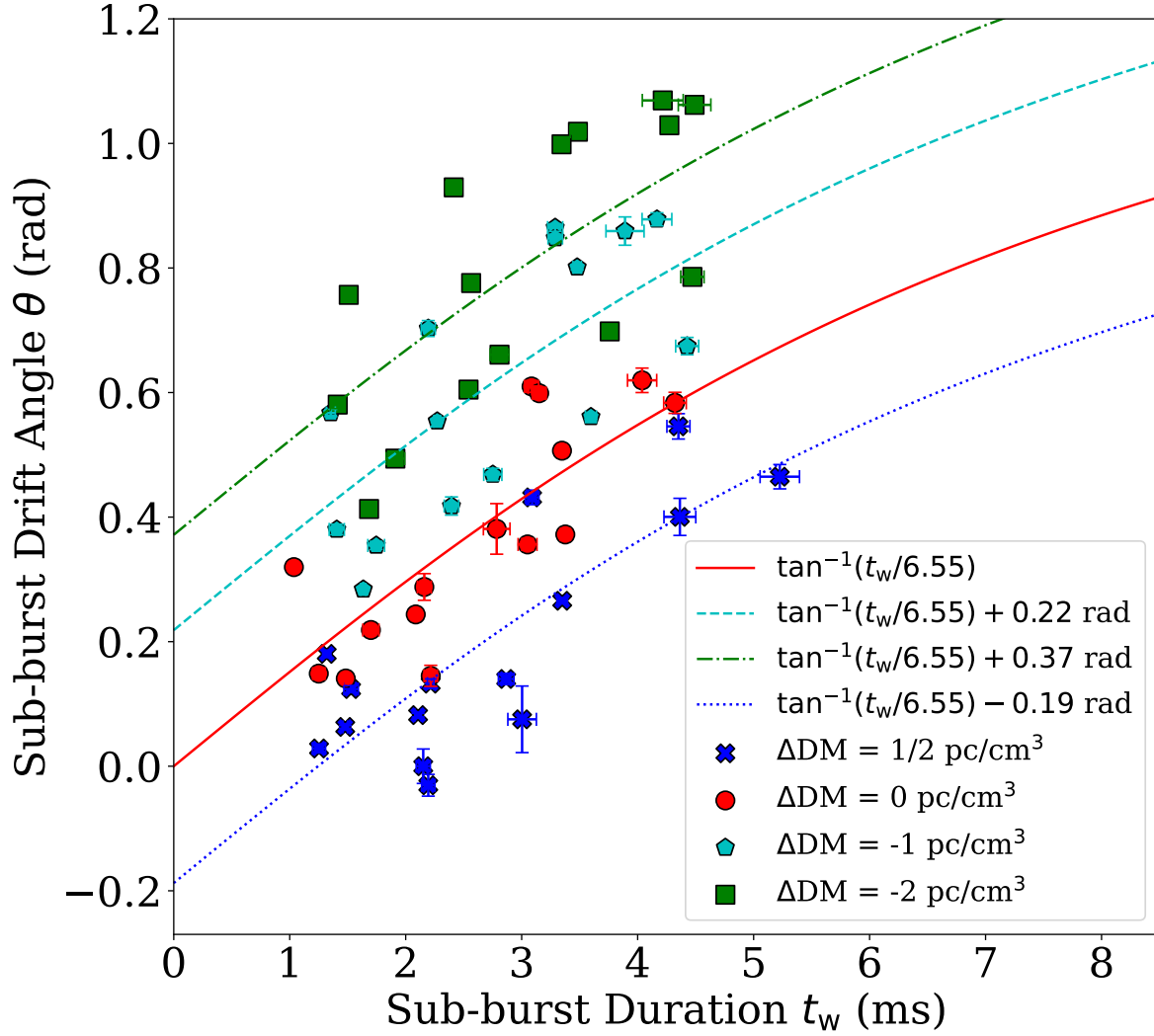


Figure 3.3: The fit angle θ vs. temporal duration t_w from sub-bursts dedispersed to small variations in the DM for the source FRB 20180916B. Red circles are sub-bursts at $\Delta\text{DM} = 0$, which corresponds to a $\text{DM} = 348.82 \text{ pc cm}^{-3}$. Blue crosses, cyan pentagons, and green squares are sub-bursts dedispersed to $\Delta\text{DM} = 0.5$, -1 , and -2 pc cm^{-3} , respectively. Error bars indicate the parameter fitting uncertainty. The red curve is the fit to the red circles and is of the form given in equation (3.8), derived from the dynamical model described in the main text. Blue, cyan, and green curves are obtained by adding a rotation (i.e., adding an angle) to the $\Delta\text{DM} = 0$ model. As discussed in Section 3.3.2 this plot demonstrates the rotational effect small variations in the DM can have on the autocorrelation of FRB waterfalls.

scatter broadening (e.g., Sec. 4.3 of Day et al. 2020). In the sample of bursts used for this analysis, bursts numbered 13 and 15 in Figure 3.6, and bursts 14, 18, and 23 in Figure 3.8 are suggestive of being composed of multiple sub-bursts, and others are likely indistinguishable from multi-bursts due to their time resolution, just as in the aforementioned example from Gourdji et al. 2019.

This raises the question of how a majority of the sub-burst slopes shown in Figure 3.1 agree with the expected relation when more outliers might be expected. Firstly, it is possible that the presence of bursts exhibiting large variations in their measurements is an indication of outlying FRBs that were incorrectly measured. Another possibility is that as the sub-bursts are smeared together, the measured duration will necessarily increase, and, since sub-bursts are mostly observed to drift downwards in frequency, the slope of the resulting autocorrelation will also be shallower. While these scenarios qualitatively describe what we should expect when measuring pulse trains as a single sub-burst, we note that our dynamical model predicts that groups of sub-bursts emitted close to each other in time will follow the same relationship as individual sub-bursts when the difference in delay time is small. This follows from equation (6) of Rajabi et al. 2020 that relates different time and frequency intervals between the FRB and observer reference frames

$$\Delta t_{\text{D}} = -t_{\text{D}} \left(\frac{\Delta \nu_{\text{obs}}}{\nu_{\text{obs}}} - \frac{\Delta \tau'_{\text{D}}}{\tau'_{\text{D}}} \right), \quad (3.7)$$

where as before t_{D} and τ'_{D} are the delay time between the trigger signal and the appearance of a sub-burst as measured in the observer's and FRB frames, respectively, and ν_{obs} is the observed frequency of the burst. The quantities $\Delta \nu_{\text{obs}}$, Δt_{D} , and $\Delta \tau'_{\text{D}}$ account for variations in these parameters. The relation central to this paper shown in equation 3.1 is obtained when $\Delta \tau'_{\text{D}} \simeq 0$, a condition that applies to groups of sub-bursts that occur closely in time as well as individual sub-bursts.

Given the possible agreement between the trends of the sub-burst slope and sub-burst drift measurements for the FRBs we have considered, we can use the following physical

interpretation in the context of our model. When observing a resolved sub-burst signal, the frequency bandwidth of the signal is determined by the dynamical velocity of the emitting material. When multiple sub-bursts are observed to occur close to each other in time (such as within a single FRB event), the drift rate of the pulse train depends on the delay time between the FRB trigger and the FRB event. When variations in the delay time are small the sub-burst drift rate will follow the same trend as the slope measurements of the individual sub-bursts. In this case, if the sub-bursts are unresolved then it will be difficult to distinguish a slope measurement from a drift rate measurement. The lack of a significant number of outliers in Figure 3.1 suggests that the situation with small variations in delay time is common.

3.3.2 DM variations as a rotation of the autocorrelation function

Following the study of the variation of measurements over ranges of plausible DMs discussed in Sec. 3.2.1, different DM choices can be modeled as rotations of the autocorrelation function of the burst. As an example, we show in Figure 3.2 two bursts each at two choices of DM. In a given waterfall we see that the shape of the burst can ‘distort’ due to the ν_{obs}^{-2} dependence on the dispersion, while that of the autocorrelation remains practically the same except for experiencing a rotation. To characterize this further we consider the sub-burst angle parameter (as opposed to the corresponding sub-burst slope derived from said angle) defining the orientation of the fitted ellipsoid’s semi-major axis measured counterclockwise from the positive frequency axis of the autocorrelation function (see Appendix 2.A). The sub-burst angles from FRB 20180916B are plotted against the corresponding temporal durations derived from the underlying two-dimensional Gaussian fits in Figure 3.3. This shows that across different DMs the measured duration varies little while the angle is offset by a constant level from values at other DMs. We can demonstrate this using equations (3.1) and (3.11) to find that the slope angle θ is related

to the sub-burst duration through

$$\theta = \arctan \left(\frac{1}{A} \frac{\nu_{\text{res}}}{\nu_{\text{obs}}} \frac{t_{\text{w}}}{t_{\text{res}}} \right), \quad (3.8)$$

where as before $A \equiv \tau'_{\text{w}}/\tau'_{\text{D}}$, and ν_{res} and t_{res} are the frequency and time resolutions of the waterfall. We also approximated ν_{obs} to be constant, which is adequate for this purpose. We find that the chosen fit obtained with equation (3.8) for the sub-bursts at $\Delta\text{DM} = 0$ (i.e., the solid curve in Figure 3.3) is also satisfactory for angles corresponding to the different ΔDM values when a simple offset angle (i.e. a rotation) is applied. Similar trends appear to hold for the other two sources considered, however it is most clear in the example of FRB 20180916B.

Measuring the sub-burst angle instead of the slope during analysis avoids the discontinuity of slope measurements around $\theta = 0$ or π , where its magnitude approaches infinity, however the uncertainty of the physically relevant quantity will still be large. The behaviour of slope measurements derived from the parameter angle in the context of autocorrelation noise is discussed in more detail in Pleunis (2020) as well as in the `dfdt`⁴ package.

3.3.3 Uncertainty due to frequency band masking

In addition to signal noise, the waterfall analyses were complicated by missing frequency bands of data, which would sometimes overlap with the frequency extent of the sub-burst under consideration. In this section we assess the extent of the uncertainty introduced by the missing frequency band data by (1) artificially masking (zero-padding) various trial Gaussian signals of known orientations and characteristic widths, (2) processing them through our pipeline, and (3) comparing the extracted sub-burst slope and duration parameters to the generating parameters.

⁴<https://github.com/zpleunis/dfdt>

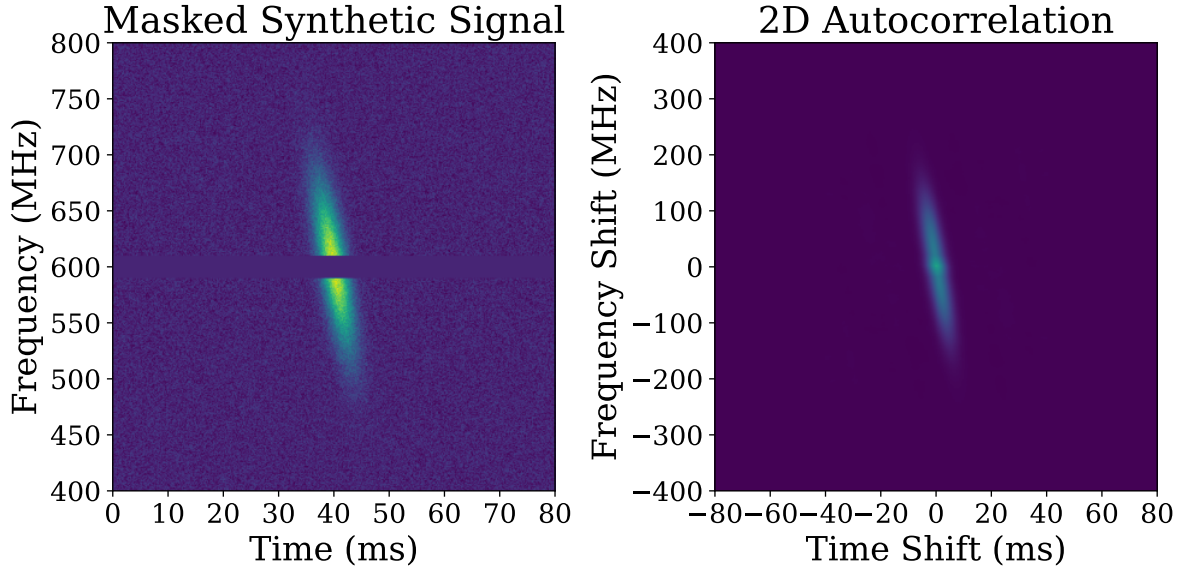


Figure 3.4: Synthetic Gaussian signal with a masked (zeroed) band (left), and 2D autocorrelation of masked signal (right). The signal shown approximately matches the characteristics of Burst 23 depicted in Figure 3.8 in each of their temporal widths, their frequency extents, their inclinations, and their total missing frequency bandwidths.

Consider for example Burst 23 of FRB 20180916B (CHIME/FRB et al. 2020) pictured, along with its two-dimensional autocorrelation, in Figure 3.8. Three frequency bands of data are absent from the original data in this burst, and the total missing bandwidth (as a fraction of the frequency extent of the sub-burst) is higher than the fractional bandwidth typically absent from sub-bursts analyzed in the paper.

To estimate the effect of missing frequency channels on our analysis we construct an artificial burst similar to Burst 23 from a Gaussian with a standard deviation along the semi-major axis of $a = 67$ MHz (90 pixels), standard deviation along the semi-minor axis $b = 2.2$ ms (15 pixels), $\theta = 10^\circ$ (inclination from vertical), and with stochastic noise of amplitude 25% that of the Gaussian amplitude. We perform our analysis on a 2D array with dimensions 540×540 pixels, having horizontal and vertical resolutions of 6.75 px/ms and 1.35 px/MHz, respectively. As a first test, we mask a band of width 18.5 MHz (25 pixels) through the center of the burst and pass this zero-padded signal through our pipeline.

The fitting procedure on the 2D autocorrelation returns $a_{\text{fit}} = 102.7$ pixels, $b_{\text{fit}} = 14.8$ pixels, and $\theta_{\text{fit}} = 9.83^\circ$. The process is visualized in Figure 3.4. For such a small inclination angle, the percentage error in t_w is very close to that of b , and is (in this case) approximately 1%. The corresponding percentage error in the sub-burst slope $d\nu_{\text{obs}}/dt_D$ is 1.7%.

We can generalize this test by shifting the frequency masking band of Figure 3.4 vertically. Upon doing so, we find that the error is independent of the frequency band’s vertical position. The percentage error for the burst duration is found to be $\simeq (-1.4 \pm 0.4)\%$, where the $\pm 0.4\%$ uncertainty applies to all band vertical positions tested, while the corresponding error in the angle is $\simeq (-1.1 \pm 0.7)\%$.

If we rotate the burst of Figure 3.4, while retaining the central band mask of 18.5 MHz (25 pixels) on burst centre, we observe a linear enhancement of error with increasing orientation. The effect is, however, a negligible one: for every burst rotation by 10° , the duration error increases by only 0.45%, while the orientation angle error decreases (or increases in magnitude) by only 0.12° . At a 30.0° burst angle, the sub-burst slope error is only 4%.

3.3.4 The narrow-band nature of the emission process

As discussed in Section 3.1.1, results from Gajjar et al. (2018) and Hessels et al. (2019) for FRB 20121102A point to a rest frame frequency of emission ν_0 that does not change significantly from burst to burst. The results presented here can be shown to also be consistent with a narrow-band emission process by inserting equation (3.2) into equation (3.1) to obtain

$$\frac{1}{\nu_{\text{obs}}^2} \frac{d\nu_{\text{obs}}}{dt_D} = -\frac{1}{\nu_0 \tau'_D}, \quad (3.9)$$

for the sub-burst slope (normalized to ν_{obs}^2), which is then predicted to be independent of ν_{obs} and scale inversely with ν_0 . Figure 3.5 shows the corresponding plot using the same data as in Figure 3.1. The broken black line is for a fit to a constant B on the combined data for the three sources, with $B \equiv (\tau'_D \nu_0)^{-1} = (6.6 \pm 0.8) \times 10^{-8}$. While there is some scatter in the data, the result is consistent with the expected lack of dependency on ν_{obs} . Any deviation could easily be accounted for with the uncertainty on the DMs and inherent variations in τ'_D . The combination of this result with the temporal narrowing and sad trombone effects discussed in Section 3.1.1 for FRB 20121102A provides evidence for the narrow-band nature of the emission process.

3.4 Conclusion

We demonstrate a method of studying the sub-burst slope in the context of DM variations from burst to burst and over time by adopting large ranges of possible DMs when measuring spectro-temporal properties of FRBs. This method reveals that even given a wide range of possible DMs for each burst from an FRB source, the slope of an individual sub-burst is inversely proportional to its temporal duration. Furthermore, for the three sources considered in this work, namely FRB 20121102A, FRB 20180916B and FRB 20180814A, significant overlap between the inverse trends found is consistent with the three relationships having a nearly identical scaling. That is, the same law can be used to describe sub-bursts from all three sources, though careful analyses over larger data sets at different frequencies would be needed to verify this. Additionally, this result suggests that the sub-burst slope law may be a useful tool for simplifying studies that require large samples of FRBs, by providing a single small adjustment DM to dedisperse waterfalls to without the complexity of verifying each burst's DM.

We believe that the simplest explanation for the existence of this trend is that the

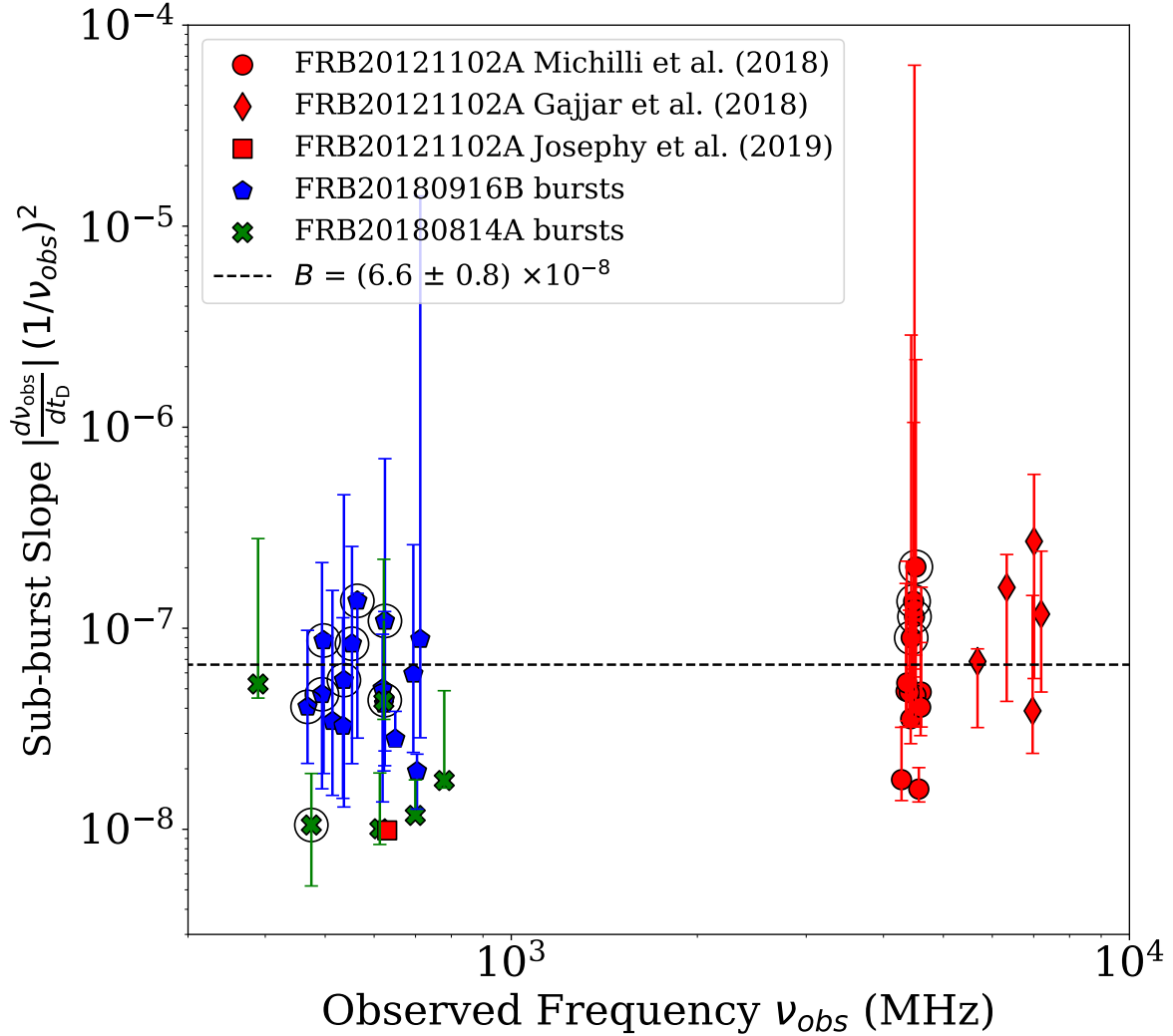


Figure 3.5: A plot of $|d\nu_{obs}/dt_D| (1/\nu_{obs}^2)$ vs. ν_{obs} for FRB 20121102A (red circles, diamonds and square from Gajjar et al. 2018, Michilli et al. 2018 and Josephy et al. 2019, respectively), FRB 20180916B (blue pentagons; CHIME/FRB et al. 2020) and FRB 20180814A (green crosses; CHIME/FRB et al. 2019). The broken black line is for a fit to a constant B on the combined data for the three sources, with $B \equiv (\tau'_D \nu_0)^{-1} = (6.6 \pm 0.8) \times 10^{-8}$. The capped lines at each point represent the range of possible values due to the range of sub-burst slopes measured at different DMs, as discussed in Section 3.2.1.

emission mechanism of these FRB sources is narrow-band in nature, which would be consistent with earlier models based on Dicke’s superradiance (Houde et al. 2019; Rajabi et al. 2019; Rajabi et al. 2020). Such a mechanism requires a trigger, which leaves room for magnetar-centric models of FRBs. To further study the relationship between the sub-burst slope and temporal duration future analyses of FRBs from all known repeater sources can be performed in the manner presented here. A large sample of sources helps to constrain the uncertainties due to variations in DM, and necessitates convenient and public access to FRB data.

Finally, we note that our discovery of a shared sub-burst slope law among these three sources suggests that this could be a universal property among repeating FRBs or at least a significant subclass of them. If deviations from this relationship exist, then it is likely the sub-burst slope law can serve as a classification tool for FRBs by discriminating sources that follow this law from those that do not. This not only motivates further searches but also provides a new tool to study and categorize FRBs based on their underlying physical mechanism.

Acknowledgements

The authors are grateful to Z. Pleunis and S. Tendulkar from the CHIME/FRB Collaboration for their help in accessing and analyzing the data for FRB 20180916B and FRB 20180814A. The authors are also grateful to the referees for the extensive feedback that significantly shaped the final manuscript. M.H. is grateful for the hospitality of Perimeter Institute where part of this work was carried out. M.H.’s research is funded through the Natural Sciences and Engineering Research Council of Canada Discovery Grant RGPIN-2016-04460. F.R.’s research at Perimeter Institute is supported in part by the Government of Canada through the Department of Innovation, Science and Economic Development Canada and by the Province of Ontario through the Ministry of

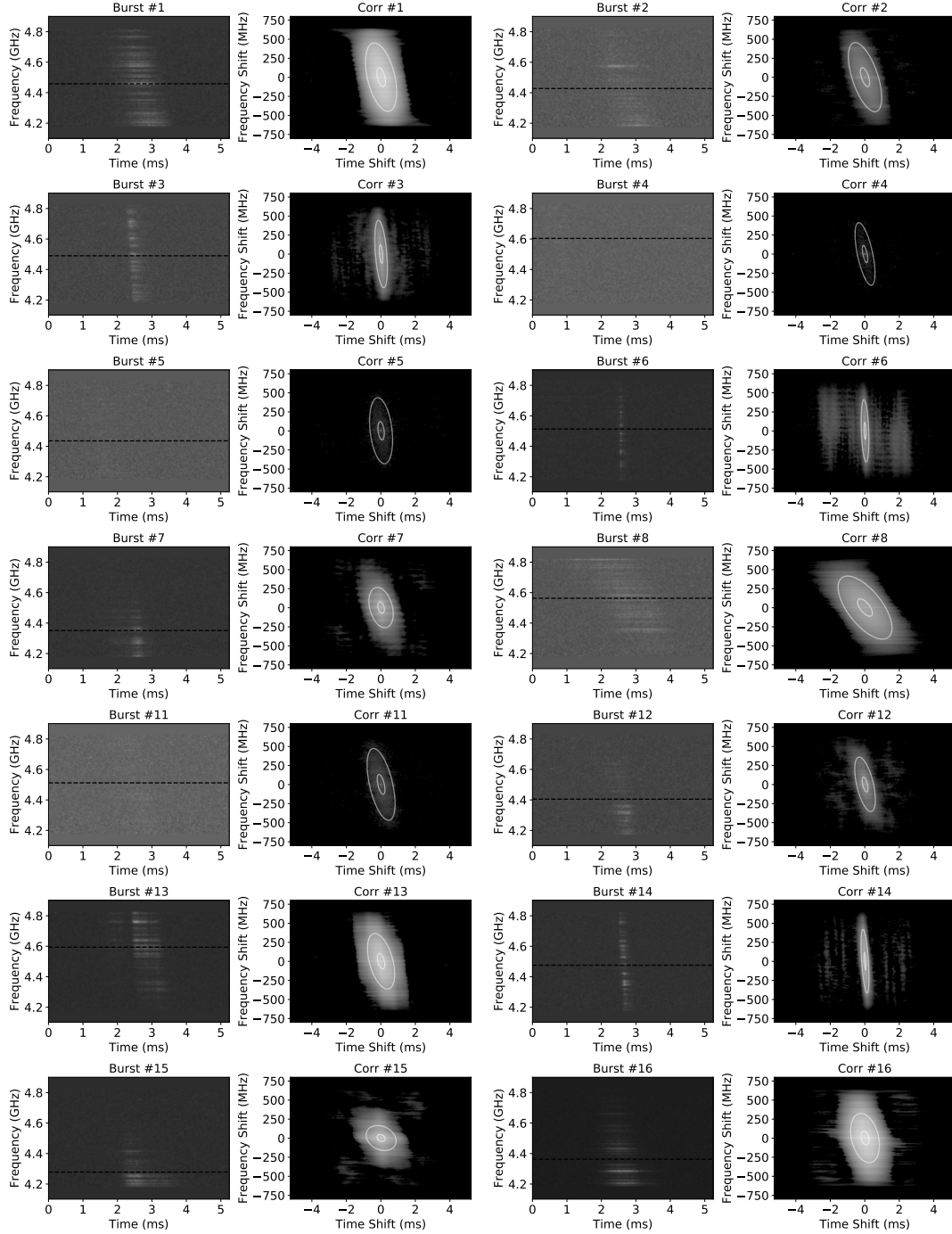


Figure 3.6: Dynamic spectra (first and third columns) and corresponding autocorrelation functions (second and fourth columns) for FRB 20121102A bursts at a frequency of approximately 4–5 GHz from Michilli et al. (2018). The dynamic spectra were dedispersed with a $DM = 559.7 \text{ pc cm}^{-3}$ and the dashed horizontal line in the waterfall denotes the center frequency ν_{obs} used for the analysis. The autocorrelation functions are modelled with a 2D Gaussian ellipsoid whose one- and two-standard deviation levels are shown using the white contours.

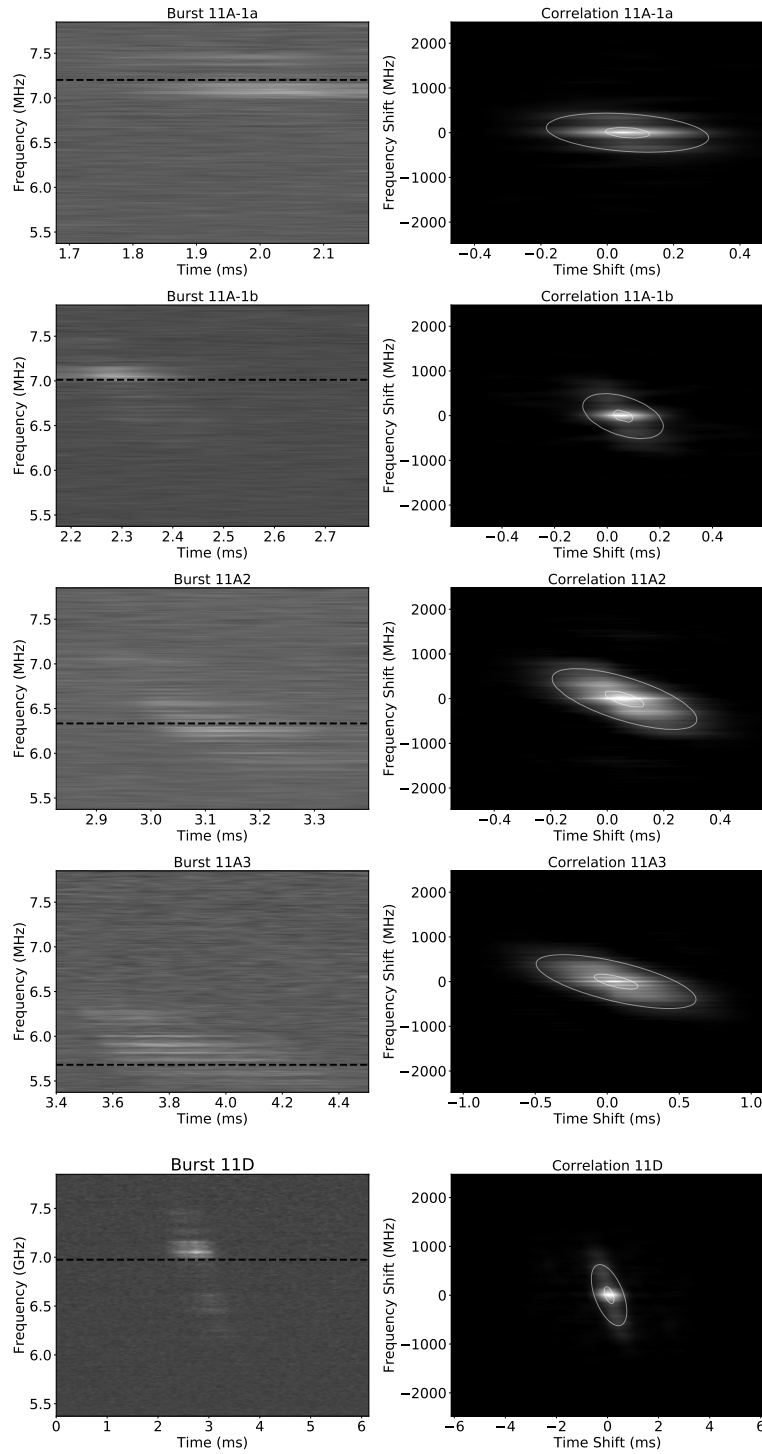


Figure 3.7: Same as Figure 3.6 but for the FRB 20121102A data at approximately 5–8 GHz published in Gajjar et al. (2018) and dedispersed with a $DM = 565 \text{ pc cm}^{-3}$. The top four sub-bursts are taken from one event, i.e., Burst 11A. Note that the time axes for the autocorrelation functions do not all share the same range, which distorts their relative appearance.

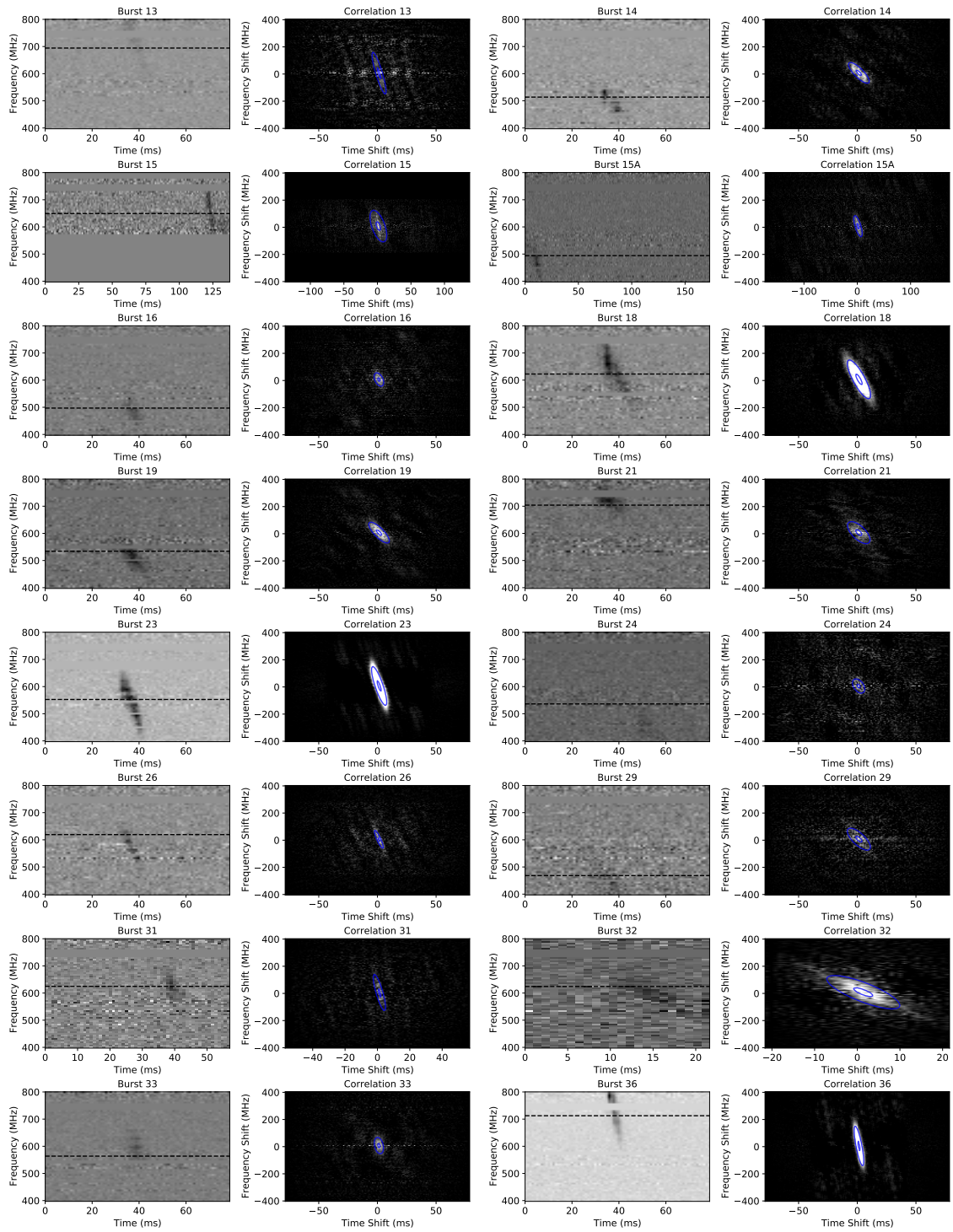


Figure 3.8: Same as Figure 3.6 but for FRB 20180916B taken from CHIME/FRB et al. (2020). These data were dedispersed with a $DM = 348.82 \text{ pc cm}^{-3}$. Note that the time axes for the autocorrelation functions do not all share the same range, which distorts their relative appearance.

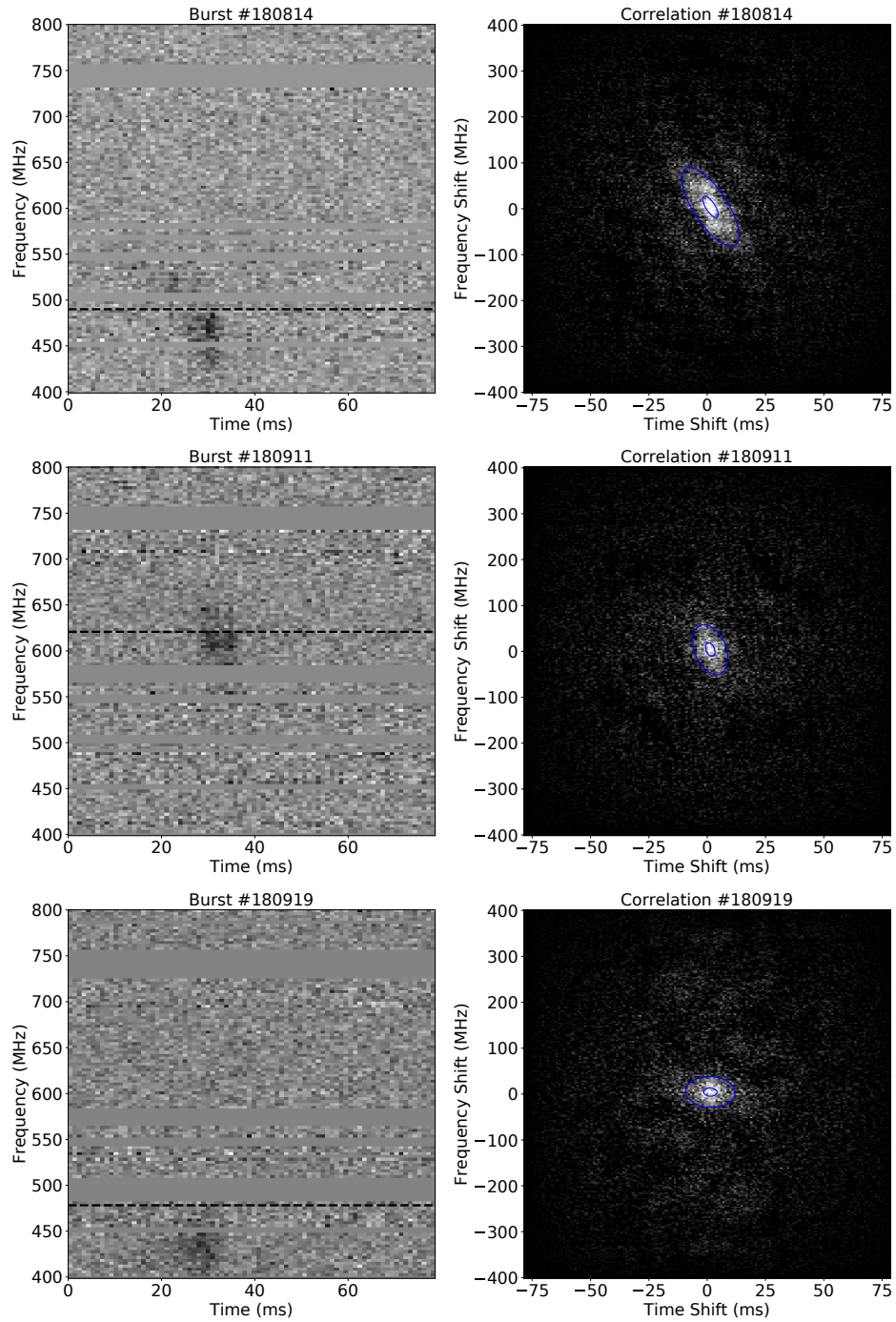


Figure 3.9: Same as Figure 3.6 but for FRB 20180814A taken from CHIME/FRB et al. (2019). These data were dedispersed with a $DM = 188.9 \text{ pc cm}^{-3}$.

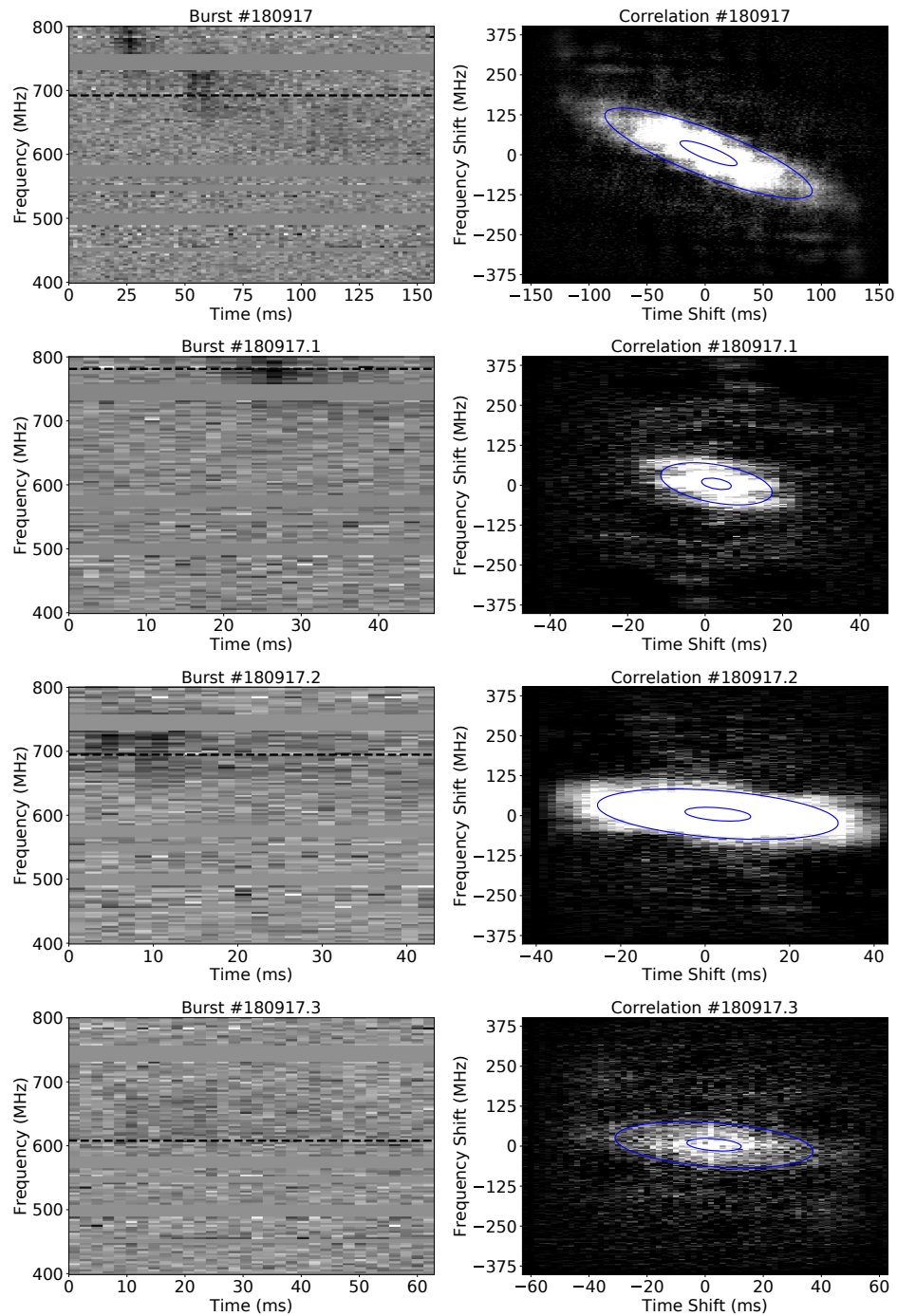


Figure 3.10: Same as Figure 3.9 but for Burst #180917 of FRB 20180814A taken from CHIME/FRB et al. (2019). The whole event is shown on the top row (not used for Figure 1 of main text), while its three separate sub-bursts are detailed in the bottom three (all used for Figure 1 of main text). Note that the time axes for the autocorrelation functions do not all share the same range, which distorts their relative appearance.

Economic Development, Job Creation and Trade. F.R. is in part financially supported by the Institute for Quantum Computing. C.M.W. and A.M. are supported by the Natural Sciences and Engineering Research Council of Canada (NSERC) through the doctoral postgraduate scholarship (PGS D).

Data Availability

The data pipeline is made available at <https://github.com/mef51/subdriftlaw> and maintained by M.A.C. Aggregate data of the bursts and the code for the figures are also available. Data of the FRB spectra are available either publicly or via the authors of their respective publications. The figures in this paper were prepared using the `matplotlib` package (Hunter 2007).

Appendices

2.A Autocorrelation Analysis

We discuss here the process of preparing and obtaining measurements from the dynamic spectra of bursts, based on the autocorrelation technique described in Hessels et al. (2019).

As mentioned in Section 3.2.1 when a waterfall consists of a train of multiple sub-bursts we separate the components and measure the slope and temporal duration of each sub-burst separately. The dynamic spectra of every sub-burst used in this analysis with its autocorrelation is shown in Figures 3.6 – 3.10.

The pipeline that every sub-burst undergoes is written in Python and consists of computing the autocorrelation of the signal, fitting a two-dimensional (2D) Gaussian to the resulting autocorrelation function, and a calculation of the physical quantities of interest from the fit parameters: namely the sub-burst slope and temporal duration. The

autocorrelation of the waterfall measures the self-similarity of the sub-burst in frequency-time space and for FRBs can be approximated by an ellipsoid with an intensity that follows a 2D Gaussian (Hessels et al. 2019). Before computing the autocorrelation and depending on the source and/or burst, some noise removal is performed. For the bursts from FRB 20121102A and FRB 20180916B this is done by subtracting from the entire spectrum a background signal obtained from a time-average of twenty or so samples taken prior to the burst. For FRB 20180814A, due to the raw format the bursts are provided in, a noise mask was acquired through correspondence with members of the CHIME/FRB Collaboration and the channels are normalized by the standard deviation of the intensity. Missing or blocked out frequency channels in dynamic spectra (e.g., because of radio frequency interference (RFI)) are zeroed out before performing the autocorrelation.

The computation of the autocorrelation function is facilitated and sped up by using a Fast Fourier Transform (FFT) of the waterfall, which is then squared and inverted (through an FFT) back to the frequency-time domain (Press et al. 2007). The autocorrelation function is then modelled with the following functional form for a rotated 2D Gaussian

$$G(x, y) = C \exp \left\{ -\frac{1}{2} \left[x^2 \left(\frac{\cos^2 \theta}{b^2} + \frac{\sin^2 \theta}{a^2} \right) + 2xy \sin \theta \cos \theta \left(\frac{1}{b^2} - \frac{1}{a^2} \right) + y^2 \left(\frac{\sin^2 \theta}{b^2} + \frac{\cos^2 \theta}{a^2} \right) \right] \right\}, \quad (3.10)$$

with the free parameters C , a , b , and θ for, respectively, the amplitude, the semi-major and semi-minor axes (i.e., the standard deviations) of the ellipsoid, and the sub-burst angle for the orientation of the semi-major axis measured counterclockwise from the positive y -axis. More precisely, the x - (i.e., for the time lag) and y -axes (i.e., for the frequency lag) are respectively oriented horizontally and vertically on the autocorrelation plots shown in Figures 3.6–3.10. To find these parameters we use the `scipy.optimize.curve_fit` package, which performs a non-linear least squares fit. The package also returns a covari-

ance matrix, which is used to calculate the uncertainty of the fitted parameters. These uncertainties are then scaled by the square-root of the reduced- χ^2 computed from the residual between the autocorrelation function and its Gaussian fit. We note again that the uncertainty calculated this way does not capture nearly the entire error budget which depends more significantly on the error in the DM (discussed in Section 3.2.1) as well the parts of the burst spectra that have been masked out and the shape of its autocorrelation.

Using the angle θ , the sub-burst slope is calculated via

$$\frac{d\nu_{\text{obs}}}{dt_{\text{D}}} = -\frac{\nu_{\text{res}}}{t_{\text{res}}} \cot \theta, \quad (3.11)$$

where ν_{res} and t_{res} are the frequency and time resolutions of the waterfall. We obtain the sub-burst duration from the fit parameters through

$$t_{\text{w}} = t_{\text{res}} \frac{ab}{\sqrt{b^2 \sin^2 \theta + a^2 \cos^2 \theta}}. \quad (3.12)$$

These expressions are also used to propagate the fit parameter uncertainties to the values of $d\nu_{\text{obs}}/dt_{\text{D}}$ and t_{w} . These uncertainties are used to confirm the assertion that DM variations are the largest source of error, as stated in Section 3.2.1.

The observation frequency ν_{obs} of each sub-burst is estimated via an intensity-weighted average of the spectrum over the whole time range. While this decreases the accuracy of the estimate as opposed to using just the on-pulse region, we find it has little bearing on the result. To fit equation (3.1) we used the `scipy.odr.RealData` package, which uses orthogonal distance regression and the uncertainties on the data to find a fit.

2.B Determination of β^+ , ν_0 and $\Delta\beta'$

The equations presented in this section apply to cases where the source of radiation travels directly toward or away from the observer.

For the determination of the maximum speed of an FRB rest frame toward the observer $\beta^+ > 0$ and ν_0 , the frequency of emission within it, we can generally set $\beta^- = -a\beta^+$ with $a \geq 0$ for the greatest (i.e., most negative) speed away from the observer. Using the relativistic Doppler shift formula (Rybicki and Lightman 1979) for the corresponding frequencies in the observer's rest frame

$$\nu_{\text{obs}}^{\pm} = \nu_0 \sqrt{\frac{1 + \beta^{\pm}}{1 - \beta^{\pm}}}, \quad (3.13)$$

we find that

$$\begin{aligned} \beta^+ &= \left(\frac{1+a}{2a} \right) \left(\frac{\nu_{\text{obs}}^{+2} + \nu_{\text{obs}}^{-2}}{\nu_{\text{obs}}^{+2} - \nu_{\text{obs}}^{-2}} \right) \\ &\times \left[1 - \sqrt{1 - \frac{4a}{(1+a)^2} \left(\frac{\nu_{\text{obs}}^{+2} - \nu_{\text{obs}}^{-2}}{\nu_{\text{obs}}^{+2} + \nu_{\text{obs}}^{-2}} \right)^2} \right] \end{aligned} \quad (3.14)$$

$$\nu_0^2 = \nu_{\text{obs}}^+ \nu_{\text{obs}}^- \sqrt{\frac{1 - (1-a)\beta^+ - a\beta^{+2}}{1 + (1-a)\beta^+ - a\beta^{+2}}}. \quad (3.15)$$

The discussion in Section 3.3 where the FRB rest frames span the range $\pm\beta^+$ corresponds to the case $a = 1$, which reduces equations (3.14)-(3.15) to equations (3.4)-(3.5) of the main text.

For the determination of $\Delta\beta'$, we start by considering that for a signal initially observed at frequency ν_{obs} a velocity change $\Delta\beta$ in the observer's rest frame will be accompanied by a change $\delta\nu_{\text{obs}}$ in frequency given by

$$\frac{\delta\nu_{\text{obs}}}{\nu_{\text{obs}}} = \frac{\Delta\beta}{1 - \beta^2}, \quad (3.16)$$

where β is the initial velocity relative to the observer. Using the special relativistic velocity addition law (Rybicki and Lightman 1979) we can relate the velocity changes in

the observer and FRB rest frames through

$$\Delta\beta = \Delta\beta' \left(\frac{1 - \beta^2}{1 + \beta\Delta\beta'} \right), \quad (3.17)$$

with $\Delta\beta'$ the corresponding velocity change in the FRB frame.

Allowing for the motions within the FRB rest frame to span the range $\pm\Delta\beta'$ (with $\Delta\beta' \geq 0$; for simplicity, we assume a symmetric velocity range about zero), while using equations (3.13) (to express β as a function of ν_{obs} and ν_0) and (3.16)-(3.17), we find the following relation for the total observed bandwidth covered by the corresponding signals

$$\frac{\Delta\nu_{\text{obs}}}{\nu_{\text{obs}}} = 2\Delta\beta' \left[1 - \Delta\beta'^2 \left(\frac{\nu_{\text{obs}}^2 - \nu_0^2}{\nu_{\text{obs}}^2 + \nu_0^2} \right)^2 \right]^{-1}. \quad (3.18)$$

Equation (3.6) follows from this relation, which reaches a maximum value when $\nu_{\text{obs}} = 0$ or $\nu_{\text{obs}} \gg \nu_0$. While equation (3.18) shows little variations whenever $\Delta\beta' \ll 1$, it could, in principle, be used to evaluate the FRB rest frame frequency ν_0 independently of equation (3.15) since it reaches a minimum of $2\Delta\beta'$ at $\nu_{\text{obs}} = \nu_0$. However, the effect is probably too small (on the order of 1% for FRB 20121102A) to be measurable given the scatter inherent to FRB data.

Bibliography

- Beloborodov, Andrei M (2020). “Blast Waves from Magnetar Flares and Fast Radio Bursts”. In: *ApJ* 896.2, p. 142.
- Beniamini, Paz and Pawan Kumar (2020). “What does FRB light-curve variability tell us about the emission mechanism?” In: *MNRAS* 498.1, pp. 651–664.
- Bhardwaj, M. et al. (2021). “A Nearby Repeating Fast Radio Burst in the Direction of M81”. In: *The Astrophysical Journal Letters* 910.2, p. L18. DOI: [10.3847/2041-8213/abeaa6](https://doi.org/10.3847/2041-8213/abeaa6).
- Bochenek, C. D. et al. (Nov. 2020). “A fast radio burst associated with a Galactic magnetar”. en. In: *Nature* 587.7832, pp. 59–62. DOI: [10.1038/s41586-020-2872-x](https://doi.org/10.1038/s41586-020-2872-x). arXiv: [2005.10828](https://arxiv.org/abs/2005.10828) [[astro-ph.HE](https://arxiv.org/abs/2005.10828)]. URL: <https://ui.adsabs.harvard.edu/abs/2020Natur.587...59B>.
- Caleb, M et al. (2020). “Simultaneous multi-telescope observations of FRB 121102”. In: *Monthly Notices of the Royal Astronomical Society* 496.4, pp. 4565–4573. DOI: [10.1093/mnras/staa1791](https://doi.org/10.1093/mnras/staa1791).
- CHIME/FRB et al. (Jan. 2019). “A second source of repeating fast radio bursts”. In: *Nature* 566.7743, pp. 235–238. DOI: [10.1038/s41586-018-0864-x](https://doi.org/10.1038/s41586-018-0864-x). arXiv: [1901.04525](https://arxiv.org/abs/1901.04525) [[astro-ph.HE](https://arxiv.org/abs/1901.04525)].
- CHIME/FRB Amiri, M et al. (2020). “Periodic activity from a fast radio burst source”. In: *Nature* 582, p. 351.

- CHIME/FRB Collaboration Andersen, BC et al. (2019). “CHIME/FRB Discovery of Eight New Repeating Fast Radio Burst Sources”. In: *ApJ* 885.1, p. L24.
- Cordes, J. M. et al. (June 2017). “Lensing of Fast Radio Bursts by Plasma Structures in Host Galaxies”. In: *ApJ* 842.1, 35, p. 35. DOI: [10.3847/1538-4357/aa74da](https://doi.org/10.3847/1538-4357/aa74da). arXiv: [1703.06580](https://arxiv.org/abs/1703.06580) [astro-ph.HE].
- Day, Cherie K. et al. (May 27, 2020). “High time resolution and polarisation properties of ASKAP-localised fast radio bursts”. In: arXiv: <http://arxiv.org/abs/2005.13162v1> [astro-ph.HE]. URL: <https://arxiv.org/abs/2005.13162>.
- Fedorova, V. A. and A. E. Rodin (Jan. 2019). “Detection of Fast Radio Bursts on the Large Scanning Antenna of the Lebedev Physical Institute”. In: *Astronomy Reports* 63.1, pp. 39–48. DOI: [10.1134/S1063772919010037](https://doi.org/10.1134/S1063772919010037). arXiv: [1812.10716](https://arxiv.org/abs/1812.10716) [astro-ph.IM].
- Fonseca, E. et al. (Mar. 2020). “Nine New Repeating Fast Radio Burst Sources from CHIME/FRB”. In: *ApJ* 891.1, L6, p. L6. DOI: [10.3847/2041-8213/ab7208](https://doi.org/10.3847/2041-8213/ab7208).
- Gajjar, V. et al. (2018). “Highest Frequency Detection of FRB 121102 at 4–8 GHz Using the Breakthrough Listen Digital Backend at the Green Bank Telescope”. In: *The Astrophysical Journal* 863.1, p. 2. DOI: [10.3847/1538-4357/aad005](https://doi.org/10.3847/1538-4357/aad005).
- Gourdji, K. et al. (2019). “A Sample of Low-energy Bursts from FRB 121102”. In: *The Astrophysical Journal* 877.2, p. L19. DOI: [10.3847/2041-8213/ab1f8a](https://doi.org/10.3847/2041-8213/ab1f8a).
- Hessels, J. W. T. et al. (2019). “FRB 121102 Bursts Show Complex Time–Frequency Structure”. In: *The Astrophysical Journal* 876.2, p. L23. DOI: [10.3847/2041-8213/ab13ae](https://doi.org/10.3847/2041-8213/ab13ae).
- Hilmarsson, G. H. et al. (2021). “Rotation Measure Evolution of the Repeating Fast Radio Burst Source FRB 121102”. In: *The Astrophysical Journal* 908.1, p. L10. DOI: [10.3847/2041-8213/abdec0](https://doi.org/10.3847/2041-8213/abdec0).
- Houde, M. et al. (Feb. 2019). “Triggered superradiance and fast radio bursts”. In: *MNRAS* 482, pp. 5492–5499. DOI: [10.1093/mnras/sty3046](https://doi.org/10.1093/mnras/sty3046). arXiv: [1810.04364](https://arxiv.org/abs/1810.04364) [astro-ph.HE].

- Houde, Martin and Fereshteh Rajabi (2018). “Interacting superradiance samples: modified intensities and timescales, and frequency shifts”. In: *Journal of Physics Communications* 2.7, p. 075015. DOI: [10.1088/2399-6528/aad300](https://doi.org/10.1088/2399-6528/aad300).
- Hunter, John D. (May 2007). “Matplotlib: A 2D Graphics Environment”. In: *Computing in Science and Engineering* 9.3, pp. 90–95. DOI: [10.1109/MCSE.2007.55](https://doi.org/10.1109/MCSE.2007.55). URL: <https://ui.adsabs.harvard.edu/abs/2007CSE.....9...90H>.
- Josephy, A. et al. (Sept. 2019). “CHIME/FRB Detection of the Original Repeating Fast Radio Burst Source FRB 121102”. In: *ApJ* 882.2, L18, p. L18. DOI: [10.3847/2041-8213/ab2c00](https://doi.org/10.3847/2041-8213/ab2c00). arXiv: [1906.11305 \[astro-ph.HE\]](https://arxiv.org/abs/1906.11305).
- Li, Ye et al. (Oct. 2019). “The FRB 121102 Host Is Atypical among Nearby Fast Radio Bursts”. In: *ApJ* 884.1, L26, p. L26. DOI: [10.3847/2041-8213/ab3e41](https://doi.org/10.3847/2041-8213/ab3e41). arXiv: [1906.08749 \[astro-ph.HE\]](https://arxiv.org/abs/1906.08749).
- Lorimer, D. R. et al. (2007). “A Bright Millisecond Radio Burst of Extragalactic Origin”. In: *Science* 318.5851, pp. 777–780. DOI: [10.1126/science.1147532](https://doi.org/10.1126/science.1147532).
- Marcote, B. et al. (2020). “A repeating fast radio burst source localized to a nearby spiral galaxy”. In: *Nature* 577.7789, pp. 190–194. DOI: [10.1038/s41586-019-1866-z](https://doi.org/10.1038/s41586-019-1866-z).
- Mathews, Abhilash (2017). *The Role of Superradiance in Cosmic Fast Radio Bursts*. Honours thesis, The University of Western Ontario.
- Metzger, Brian D., Ben Margalit, and Lorenzo Sironi (May 2019). “Fast radio bursts as synchrotron maser emission from decelerating relativistic blast waves”. In: *MNRAS* 485.3, pp. 4091–4106. DOI: [10.1093/mnras/stz700](https://doi.org/10.1093/mnras/stz700). arXiv: [1902.01866 \[astro-ph.HE\]](https://arxiv.org/abs/1902.01866). URL: <https://ui.adsabs.harvard.edu/abs/2019MNRAS.485.4091M>.
- Michilli, D. et al. (2018). “An extreme magneto-ionic environment associated with the fast radio burst source FRB 121102”. In: *Nature* 553.7687, pp. 182–185. DOI: [10.1038/nature25149](https://doi.org/10.1038/nature25149).

- Michilli, D. et al. (2021). “An Analysis Pipeline for CHIME/FRB Full-array Baseband Data”. In: *The Astrophysical Journal* 910.2, p. 147. DOI: [10.3847/1538-4357/abe626](https://doi.org/10.3847/1538-4357/abe626).
- Pastor-Marazuela, Inés et al. (Aug. 2021). “Chromatic periodic activity down to 120 megahertz in a fast radio burst”. In: *Nature* 596.7873, pp. 505–508. DOI: [10.1038/s41586-021-03724-8](https://doi.org/10.1038/s41586-021-03724-8). arXiv: [2012.08348](https://arxiv.org/abs/2012.08348) [astro-ph.HE]. URL: <https://ui.adsabs.harvard.edu/abs/2021Natur.596..505P>.
- Petroff, E., J. W. T. Hessels, and D. R. Lorimer (2019). “Fast radio bursts”. In: *The Astronomy and Astrophysics Review* 27.1. DOI: [10.1007/s00159-019-0116-6](https://doi.org/10.1007/s00159-019-0116-6).
- Platts, E. et al. (2019). “A living theory catalogue for fast radio bursts”. In: *Physics Reports* 821, pp. 1–27. DOI: [10.1016/j.physrep.2019.06.003](https://doi.org/10.1016/j.physrep.2019.06.003).
- Pleunis, Ziggy (2020). “Fast radio burst detection and morphology with the CHIME telescope”. PhD thesis. McGill University.
- Press, William H. et al. (2007). *Numerical Recipes 3rd Edition: The Art of Scientific Computing*. 3rd ed. USA: Cambridge University Press. ISBN: 0521880688.
- Rajabi, F. et al. (2019). “New evidence for Dicke’s superradiance in the 6.7 GHz methanol spectral line in the interstellar medium”. In: *MNRAS* 484.2, pp. 1590–1597. DOI: [10.1093/mnras/stz074](https://doi.org/10.1093/mnras/stz074). arXiv: [1810.04365](https://arxiv.org/abs/1810.04365) [astro-ph.GA].
- Rajabi, Fereshteh and Martin Houde (2016a). “DICKE’S SUPERRADIANCE IN ASTROPHYSICS. II. THE OH 1612 MHz LINE”. In: *The Astrophysical Journal* 828.1, p. 57. DOI: [10.3847/0004-637x/828/1/57](https://doi.org/10.3847/0004-637x/828/1/57).
- (2016b). “Dicke’s Superradiance in Astrophysics. II. THE OH 1612 MHz LINE”. In: *ApJ* 828.1, p. 57.
- (Mar. 2017). “Explaining recurring maser flares in the ISM through large-scale entangled quantum mechanical states”. In: *Science Advances* 3.3, e1601858. DOI: [10.1126/sciadv.1601858](https://doi.org/10.1126/sciadv.1601858). arXiv: [1704.01491](https://arxiv.org/abs/1704.01491) [astro-ph.GA]. URL: <https://ui.adsabs.harvard.edu/abs/2017SciA...3E1858R>.

- Rajabi, Fereshteh et al. (Sept. 2020). “A simple relationship for the spectro-temporal structure of bursts from FRB 121102”. In: MNRAS 498.4, pp. 4936–4942. DOI: [10.1093/mnras/staa2723](https://doi.org/10.1093/mnras/staa2723). arXiv: [2008.02395](https://arxiv.org/abs/2008.02395) [[astro-ph.HE](#)].
- Rajabi, Fereshteh et al. (2020). “A simple relationship for the spectro-temporal structure of bursts from FRB 121102”. In: *Monthly Notices of the Royal Astronomical Society* 498.4, pp. 4936–4942. DOI: [10.1093/mnras/staa2723](https://doi.org/10.1093/mnras/staa2723).
- Rajwade, K. M. et al. (July 2020). “Possible periodic activity in the repeating FRB 121102”. In: MNRAS 495.4, pp. 3551–3558. DOI: [10.1093/mnras/staa1237](https://doi.org/10.1093/mnras/staa1237). arXiv: [2003.03596](https://arxiv.org/abs/2003.03596) [[astro-ph.HE](#)]. URL: <https://ui.adsabs.harvard.edu/abs/2020MNRAS.495.3551R>.
- Rybicki, George B. and Alan P. Lightman (1979). *Radiative processes in astrophysics*. New York: Wiley.
- Simard, Dana and Vikram Ravi (Aug. 2020). “Scintillation Can Explain the Spectral Structure of the Bright Radio Burst from SGR 1935+2154”. In: ApJ 899.1, L21, p. L21. DOI: [10.3847/2041-8213/abaa40](https://doi.org/10.3847/2041-8213/abaa40). arXiv: [2006.13184](https://arxiv.org/abs/2006.13184) [[astro-ph.HE](#)].
- Tendulkar, S. P. et al. (Jan. 2017). “The Host Galaxy and Redshift of the Repeating Fast Radio Burst FRB 121102”. In: ApJ 834.2, L7, p. L7. DOI: [10.3847/2041-8213/834/2/L7](https://doi.org/10.3847/2041-8213/834/2/L7). arXiv: [1701.01100](https://arxiv.org/abs/1701.01100) [[astro-ph.HE](#)]. URL: <https://ui.adsabs.harvard.edu/abs/2017ApJ...834L...7T>.
- The CHIME/FRB Collaboration Andersen, B. C. et al. (Nov. 2020). “A bright millisecond-duration radio burst from a Galactic magnetar”. In: Nature 587.7832, pp. 54–58. DOI: [10.1038/s41586-020-2863-y](https://doi.org/10.1038/s41586-020-2863-y). arXiv: [2005.10324](https://arxiv.org/abs/2005.10324) [[astro-ph.HE](#)].
- Wang, Weiyang et al. (2019). “On the Time–Frequency Downward Drifting of Repeating Fast Radio Bursts”. In: ApJ 876.1, p. L15.

Chapter 4

A broad survey of spectro-temporal properties from FRB 20121102A¹

4.1 Introduction

Fast radio bursts (FRBs) are short and intense pulses of radiation whose emission mechanism eludes understanding despite a multitude of theoretical models and many recent observational efforts. Observationally, the originating environments, energy distributions, polarization properties, and activity cycles of FRB sources have been investigated, with each new study often adding a new unexpected characteristic (Petroff, Hessels, and Lorimer 2022). Theoretical explanations for FRBs center around extreme environments such as magnetars where large numbers of particles in a plasma state emit coherently (Lyubarsky 2021). This flurry of activity around FRBs has revealed significant challenges in understanding this phenomena and in constraining the possible explanations.

Many of the observational characteristics of FRBs vary dramatically from source to source, making it unclear which features are arising due to the emission mechanism, the environment, or propagation effects. The spectral luminosities of FRB sources span sev-

¹M. A. Chamma, F. Rajabi, A. Kumar & M. Houde. Submitted to MNRAS.

eral orders of magnitude and the durations of bursts can range from tens of nanoseconds to tens of milliseconds (Nimmo et al. 2022). The polarization properties of FRBs vary as well; for example in FRB 20121102A (Spitler et al. 2014, 2016) bursts have a constant polarization across their duration (Michilli et al. 2018), whereas in FRB 20180301A the polarization angle of some bursts show diverse behaviours (Luo et al. 2020). In FRB 20190520B, the range of rotation measures (RMs) observed are the broadest observed for any type of astrophysical source studied (Anna-Thomas et al. 2022), while FRB 20121102A has the largest absolute RM observed (Hilmarsson et al. 2021). These characteristics of FRB sources complicate our understanding of the processes involved and are likely due to an overlap of multiple different phenomena.

One avenue for understanding the emission mechanism of FRBs is to study the spectro-temporal properties of bursts, which has revealed several relationships that are common from burst to burst and even from source to source. Among these quantities, which include the bandwidth, duration, and central frequency, are the drift rate and the similar but distinct sub-burst slope or intra-burst drift². The drift rate refers to the change in frequency of multiple resolved sub-bursts within a single waterfall, and the tendency for later sub-bursts to arrive at lower frequencies is called the ‘sad trombone’ effect. The sub-burst slope on the other hand refers to the change in frequency with time within a single sub-burst or pulse. Hessels et al. (2019) studied bursts from FRB 20121102A and the relationship between their frequency and the drift rate of multiple resolved sub-bursts, finding that the drift rate increased with frequency. This relationship appeared to be linear (Joseph et al. 2019).

In the triggered relativistic dynamical model (TRDM) proposed by Rajabi et al. (2020), an inverse relationship was predicted between a sub-burst’s slope and its duration from the assumptions of a narrow-band emission process and relativistic motions in the

²The ‘sub-burst slope’ terminology was used in Chamma et al. (2021) while ‘intra-burst drift’ was used in Jahns et al. (2022). Both terms describe the same measurement and we will use ‘sub-burst slope’ hereafter.

source. This prediction agreed with measurements made for a sample of bursts from FRB 20121102A. This relationship was further explored in Chamma et al. (2021) where bursts analysed from three repeater sources (FRB 20180916B (CHIME/FRB 2020) and FRB 20180814A (Amiri et al. 2019) in addition to FRB 20121102A) also had sub-burst slopes that varied inversely with duration, indicating that the same relationship could describe the features of bursts from different sources. The model in Rajabi et al. (2020) also predicted a quadratic relationship between the sub-burst slope and the frequency, and some evidence of this can be seen in various datasets as plotted in Fig. 5 of Chamma et al. (2021) and Fig. 8 of Wang et al. (2022). Jahns et al. (2022) studied over 800 bursts from FRB 20121102A in the 1.1-1.7 GHz band and also found the sub-burst slope to be inversely proportional to duration. In addition they compared the sub-burst slope to a dozen drift rates and found that the drift rates were larger but seemed to extend the same trend with the duration as the sub-burst slopes do (Jahns et al. 2022). This behaviour for drift rates and sub-burst slopes obeying similar or identical relationships is expected within the TRDM when groups of sub-bursts are emitted at roughly the same time (Sec. 3.1 of Chamma et al. 2021; Rajabi et al. 2020). Given these recent discoveries it is fruitful to study the spectro-temporal features of bursts in order to better characterize these relationships, to find their limitations, and to find possible commonalities between sources that will contribute to our understanding of the FRB emission mechanism.

In this work we investigate if the same spectro-temporal relationships, such as the relationship between the sub-burst slope and the duration, are followed for a large and diverse sample of bursts from a single source as this will indicate if bursts from a single source can be differentiated based on the spectro-temporal relationships they obey as well as the robustness of these relationships. To this end we collect bursts from multiple observational studies of the repeating source FRB 20121102A, one of the best observed repeaters with bursts that cover a wide range of frequencies and durations, and measure their spectro-temporal properties. Our measurements include the central frequency, the

bandwidth, the sub-burst slope, the sad-trombone drift rate (when applicable), and the duration of every burst and sub-burst. We investigate the relationships between these quantities, and if a single relationship is sufficient to describe the data or if deviations exist.

In the following, Section 4.2 will describe the observations used and the bursts sampled for this study. Section 4.3 will describe how data are prepared, how measurements are obtained using 2D autocorrelations, and how the dispersion measure (DM) for each burst is handled and optimized within the context of the burst sample. Section 4.4 will describe the measurements obtained and explore different correlations between the spectro-temporal properties of the bursts while Section 4.5 will discuss the relationships observed, the predictions of the TRDM in more detail, and possible implications. The paper is summarized with our conclusions in Section 4.6.

4.2 Burst Sampling

We list here the observations used and the properties of the bursts sampled for our study.

Michilli et al. (2018) observed 16 bursts from FRB 20121102A using the Arecibo Observatory in a band that spanned 4.1-4.9 GHz. We use all the bursts they observed and separated the components of three of their bursts (M9, M10, and M13) for a total of 19 single pulses. The durations of these bursts range from, as measured by their full-width-half-maximum (FWHM) and excluding the bursts whose components we have separated, 0.03 ms to 1.36 ms (Michilli et al. 2018).

Gajjar et al. (2018) observed 21 bursts from FRB 20121102A using the Green Bank Telescope in a band of 4-8 GHz all of which were 100% linearly polarized. Of these observations we exclude 5 due to their low SNR and split three of their bursts (11A, 12A, and 12B) for a total of 21 single pulses, with durations that range from 0.18 ms to 1.74 ms (Gajjar et al. 2018).

Oostrum et al. (2020) observed 30 bursts from FRB 20121102A using the WSRT/Apertif telescope in a band spanning 1250-1450 MHz (and 1220 to 1520 MHz for one burst) with much lower levels of linear polarization than observed at higher frequencies. We use 23 of these bursts with the remaining seven excluded due to low SNR. All bursts from this dataset were single pulses. The durations of these bursts, as measured by a top hat pulse with an equivalent integrated flux density, spans 1.6 ms to 8.2 ms (Oostrum et al. 2020).

Aggarwal et al. (2021) searched data observed by Gourdji et al. (2019) using the Arecibo telescope in a band spanning 580 MHz (with a backend spanning 800 MHz) and centered around 1375 MHz. Including the 41 bursts found by Gourdji et al. (2019), the search yielded a total of 133 bursts in three hours of data. Notably, almost all of these bursts occur above 1300 MHz. Of these bursts we exclude almost half due to a low SNR and separate 6 into single pulses for a total of 63 bursts. The durations of the bursts used span 1.16 ms to 17.16 ms based on the FWHM obtained from the burst autocorrelation (see Section 4.3).

Li et al. (2021) used the FAST telescope to detect 1652 bursts in about 60 hours of data over 47 days in a band spanning 1000 to 1500 MHz. These bursts followed a bimodal energy distribution³ with peaks around $10^{37.8}$ and $10^{38.6}$ erg as well as a bimodal wait-time distribution with peaks at around 3.4 ms and 70 s. Jahns et al. (2022) found a weak bimodality in the burst energy distribution in their sample of 849 bursts and could not conclusively confirm the result of Li et al. (2021).

In order to investigate if these differing properties of wait-time and energy might correspond to different spectro-temporal features or relationships we sampled bursts from both peaks of the bimodal energy and wait-time distributions reported by Li et al. (2021). For the energy distribution we sampled 20 bursts from both peaks (10 each) of the energy distribution by filtering their list of bursts to those with estimated energies between $10^{37.7}$ and $10^{37.8}$ erg for the first peak and $10^{38.6}$ and $10^{38.7}$ erg for the second peak. To select

³For a discussion on differences in methodology when using the observing bandwidth versus burst bandwidth to compute burst energies see Aggarwal (2021) and Section 3 of Jahns et al. (2022).

bursts with high enough SNR for a good measurement we additionally filter bursts from the first peak that have a peak flux density greater than 10 mJy and greater than 100 mJy from the second peak. Different flux limits are chosen for each peak to ensure a large enough sample and are somewhat arbitrary. For the wait-time distribution, we filtered for bursts with wait-times between ~ 4 ms to ~ 6 ms and with a peak flux density above 40 mJy, and wait-times between ~ 63 s to ~ 100 s above 100 mJy. This yielded 11 and 13 bursts from each peak, respectively, for an additional 24 bursts. Of this sample, several more were excluded due to an SNR that was still too low to obtain measurements and many of the short wait-time bursts were split into multiple components, which finally resulted in a total of 41 single pulses. Of this total, 6 and 12 bursts were from the short and long wait-time peaks, respectively. Only 2 bursts remained from the low energy peak and 7 from the high energy peak, 1 burst was included for having a long duration, and 13 were new pulses that we had separated. Due to challenges in acquiring the data we decided to proceed with this sample. The bursts used span a frequency range of 1080-1430 MHz and their FWHM durations span 0.56-15.43 ms.

The sample of bursts analysed in this study total 167 and broadly represent all the types of bursts that have been observed from FRB 20121102A, spanning frequencies ranging from 1080 MHz to 7.4 GHz and durations from less than 1 ms to about and greater than 10 ms. Figure 4.1 shows a distribution of the frequencies and durations of the bursts used in our sample.

4.3 Methods and Analysis

This section will describe how the burst waterfalls are loaded and their spectro-temporal properties measured via 2D autocorrelations of the waterfall (Hessels et al. 2019; Chamma et al. 2021), as well as the dispersion measure (DM) ranges used for the measurements, and how measurements are reviewed and validated. We also describe a graphical user

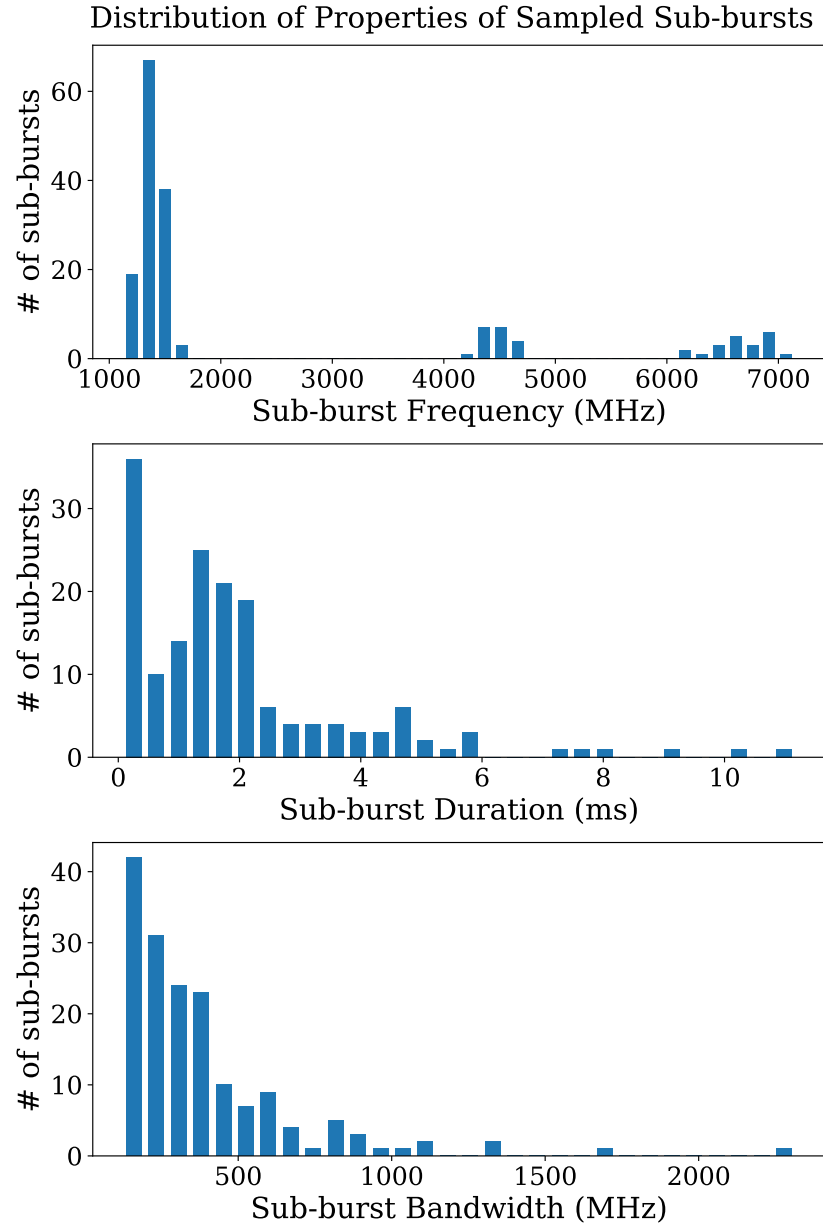


Figure 4.1: Histograms of the sub-bursts sampled for this study showing the frequency (top), sub-burst duration (middle), and sub-burst bandwidth (bottom).

interface (GUI) we developed to aid in the measurement of burst properties that is easily extensible and publicly available.

The FRB observations described in Section 4.2 were obtained from the authors of their respective publications and we describe in the following how they are pre-processed in order to reduce computation time, remove radio frequency interference (RFI), and/or crop burst files before performing measurements. FRB waterfall data are available in various formats and include `filterbank` and `PSRFITS` files, which were loaded using the `PYPULSE`⁴ and `YOUR`⁵ software packages before being stored as 2D Python `numpy` arrays.

The waterfalls of bursts from Michilli et al. (2018) were provided via an ASCII dump, dedispersed, and at frequency and time resolutions of 1.5625 MHz and 0.01024 ms, respectively, with 512 frequency channels and 512 time samples (i.e. with dimensions 512 x 512).

Burst waterfalls from Gajjar et al. (2018) were available dedispersed in `PSRFITS` format at a resolution of 183 kHz and 0.01024 ms with 19456 frequency channels and 2048 time samples, which we subsampled in frequency by a factor of 8 to obtain 2432 frequency channels at a resolution of 1.464 MHz. These were then stored in arrays of size 1690 x 2048 to exclude masked channels present at the bottom of the band.

Waterfalls from Oostrum et al. (2020) were obtained un-dedispersed in the `PSRFITS` format with resolutions of about 0.195 MHz and 0.04096 ms with size 1024 x 25000 channels, which we dedispersed to each burst’s reported DM and downsampled by a factor of 8 to resolutions of 1.5625 MHz and 0.32768 ms. These waterfalls were then centered and cropped to be stored at a size of 128 x 200 channels. In addition, before downsampling we applied both a spectral kurtosis and Savitzky-Golay filter (SK-SG filter; Agarwal et al. 2020; Nita, Gary, and Hellbourg 2016) that is available via the `YOUR` package to mask channels with high RFI.

The waterfall data from Aggarwal et al. (2021) are provided in long duration filterbank

⁴<https://github.com/mtlam/PyPulse>

⁵<https://github.com/thebyteproject/your>

files with a list of candidate timestamps, and the BURSTFIT⁶ package is used to dedisperse the data to each burst’s DM and select a 0.1 s long waterfall around the burst. These waterfalls are then saved as arrays of size 64 x 1220 at resolutions of 12.5 MHz and 0.08192 ms, respectively.

Data from Li et al. (2021) were obtained via correspondence and consisted of PSR-FITS files for each burst. We load these with YOUR at a size of 4096 x 131072 channels and resolutions of 122 kHz and 0.098304 ms, and then filter them with the SK-SG filter. We then dedisperse each waterfall to the reported burst DM, subsample to 256 frequency channels, center about the time channel with the peak frequency-averaged intensity and crop to an array of size of 256 x 1000 with resolutions of 1.952 MHz and 0.098304 ms. All the bursts in this study are preprocessed in the way described in order to facilitate the measurements of their spectro-temporal features.

Despite the pre-processing of the waterfalls there are still several tasks that are needed on a burst-by-burst basis, that, with a large number of bursts and measurements to manage, can quickly become overwhelming and difficult to review. These tasks include additional noise removal (such as masking channels or applying an SK-SG filter), additional subsampling to increase the S/N, and separating the components of bursts with multiple pulses. While these tasks can be automated to an extent, being able to manage and customize a measurement allows for more accurate results and the inclusion of strange bursts that might not fit in an automation pipeline of limited complexity. To this end we developed an extensible graphical user interface (GUI) called FRBGUI that allows a user to input additional masks, change the subsampling of the data, and isolate components of a burst, and used it to prepare bursts and obtain measurements of the spectro-temporal features.

The spectro-temporal features of each burst are obtained via a 2D Gaussian fit to the 2D autocorrelation of the burst waterfall. An autocorrelation of the waterfall helps

⁶<https://thepetabyteproject.github.io/burstfit/>

increase the S/N for measurement and limits the effect of spectral structures, noise, and banding in the burst. The Gaussian model of the autocorrelation therefore provides an analytical and robust way of measuring the spectro-temporal features from a small number of parameters. This technique is detailed in Appendix A of Chamma et al. (2021) (for example), and for this study, the Gaussian fit is obtained using the normalized physical coordinates of the autocorrelation. Thus, the dimensions of the Gaussian model's parameters are unitless, and we write with $x = t/(1 \text{ ms})$ and $y = \nu/(1 \text{ MHz})$

$$G(x, y) = C \exp \left\{ -\frac{1}{2} \left[(x - x_0)^2 \left(\frac{\cos^2 \theta}{b^2} + \frac{\sin^2 \theta}{a^2} \right) + 2(x - x_0)(y - y_0) \sin \theta \cos \theta \left(\frac{1}{b^2} - \frac{1}{a^2} \right) + (y - y_0)^2 \left(\frac{\sin^2 \theta}{b^2} + \frac{\cos^2 \theta}{a^2} \right) \right] \right\}, \quad (4.1)$$

where C , x_0 , y_0 , a , b , and θ are the model parameters corresponding to the amplitude, central x - and y - positions, the standard deviations of the Gaussian, and the orientation of the semi-major axis (a) measured counterclockwise from the positive y -axis. The fit is found using the `scipy.optimize.curve_fit` package and we found that the use of normalized physical coordinates, as defined above, when obtaining this fit improves the accuracy of the sub-burst slope measurements by almost 40% when the burst is nearly vertical. The sub-burst slope and duration are obtained via equations A2-A3 of Chamma et al. (2021), with the modification that the unit conversion becomes unity due to the choice of coordinates when obtaining the Gaussian fit, so that

$$\frac{d\nu_{\text{obs}}}{dt_{\text{D}}} = - \left(1 \frac{\text{MHz}}{\text{ms}} \right) \cot \theta, \quad (4.2)$$

$$t_{\text{w}} = (1 \text{ ms}) \frac{ab}{\sqrt{b^2 \sin^2 \theta + a^2 \cos^2 \theta}}, \quad (4.3)$$

where $d\nu_{\text{obs}}/dt_{\text{D}}$ and t_{w} are the sub-burst slope and sub-burst duration⁷, respectively,

⁷The duration defined in eq. (4.3) is the correlation length of the burst, and can be converted to other

and ν_{obs} and t_{D} are the observed frequency and delay time (or arrival time) of the burst, written in the formalism of Rajabi et al. (2020). We also compute the total bandwidth B_{tot} according to

$$B_{\text{tot}} = (1 \text{ MHz}) \sqrt{8 \ln 2} a \cos \theta, \quad (4.4)$$

which is the semi-major axis of the Gaussian ellipsoid scaled to its FWHM value and projected on to the frequency axis. Figure 4.2 shows an example measurement of the spectro-temporal properties of burst B006 from Aggarwal et al. (2021). Numerically, equation (4.2) is equivalent to finding the line that connects the peaks of each row of the autocorrelation and finding the corresponding slope, while equation (4.3) is equivalent (up to a factor of $2\sqrt{\ln 2}$) to finding the FWHM of the 1D autocorrelation at a frequency lag of zero. For bursts with multiple components in a single waterfall, the autocorrelation changes in size to include the multiple components and equations (4.2) to (4.4) are still valid. We can therefore perform the same analysis to obtain the drift rate if a fit can be found to the larger autocorrelation. The drift rates we obtain are treated distinctly from the sub-burst slopes as these potentially arise from different phenomena.

Because the choice of DM affects the value of the sub-burst slope and, to a lesser extent, the sub-burst duration, each burst is measured over a range of trial DMs. The DM can vary from burst to burst and for a single burst, especially unresolved pulses, the DM might be ambiguous if it is unclear whether to maximize the S/N of the burst or its structure (Gajjar et al. 2018; Chamma et al. 2021, Sec 2.1). We therefore measure each burst over a grid of DMs spanning 555 to 575 pc/cm^3 in steps of 0.5 pc/cm^3 , chosen to account for the historical range of DMs observed from FRB 20121102A. Each burst is incoherently dedispersed from its reported DM to the trial DM and measured via autocorrelation, resulting in 42 sets of measurements per burst including the reported

definitions of burst duration with a simple scaling. If the burst is Gaussian with a standard deviation of σ_{p} and FWHM $t_{\text{FWHM}} = 2\sqrt{2 \ln 2} \sigma_{\text{p}}$, then the correlation length t_{w} is related to those durations by $t_{\text{w}} = \sqrt{2} \sigma_{\text{p}}$, and $t_{\text{w}} = 1/\sqrt{4 \ln 2} t_{\text{FWHM}} \simeq 0.6 t_{\text{FWHM}}$.

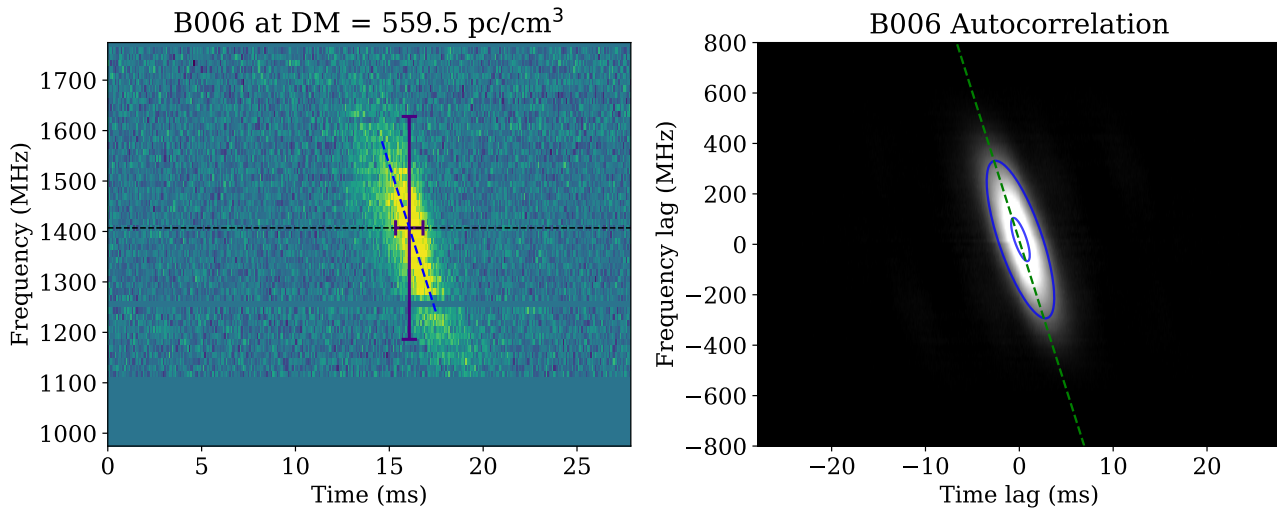


Figure 4.2: Example measurement of burst B006 from Aggarwal et al. (2021). The left panel shows the burst waterfall dedispersed to 559.5 pc/cm^3 with the dashed line, horizontal bar, and vertical bar indicating the sub-burst slope, duration, and total bandwidth obtained via the 2D Gaussian model of the autocorrelation, shown on the right. On the right, the image shows the computed autocorrelation, and the blue outlines are contours of the Gaussian model at a quarter and 90% of the peak. The dashed green line shows the corresponding slope.

burst DM.

The total set of measurements obtained over the DM grid are then filtered to exclude sub-burst slopes that are positive or with measurement errors larger than 40%. We exclude all positive sub-burst slopes under the assumption that they are unphysical and due to over dedispersion (Chamma et al. 2021; Jahns et al. 2022). Most of the measurement errors larger than 40% are due to the maximal DM in the range being greater than the published DM of a burst. Each burst therefore has a sub-burst slope that is nearly vertical at some point over the DM range where errors can be very large (see eq. 4.2).

The remaining measurements are then grouped by DM and a fit is found between the sub-burst slope and duration with the form $(d\nu_{\text{obs}}/dt_{\text{D}})/\nu_{\text{obs}} = A/t_{\text{w}}$, which is the relationship predicted for these two properties by the TRDM. Of this set of fits, we compute a reduced- χ^2 to assess the goodness of the fit and tabulate the remaining number of bursts that passed the filtering process for each DM. For each of the datasets listed

in Section 4.2, the range of DMs is limited to only include those DMs that include all the bursts in the sample, and, within this limited range, the DM with optimal (minimal) reduced- χ^2 is chosen as the representative DM for that sample.

The range of values in the remaining measurements in the limited DM range are then used as an estimate of the uncertainties. For example, the bursts from Michilli et al. (2018) are measured over the DM range 555-575 pc/cm³, and, after filtering invalid measurements, the remaining DMs that include all of the bursts range from 555-560 pc/cm³. Within this limited DM range, the DM with optimal reduced- χ^2 is found to be 558 pc/cm³, and the range of measurements over the limited DM range are used as the uncertainties of the measurement at 558 pc/cm³. Treating the measurements of each burst in this manner helps account for the effect of the DM on the measurement and allows for an estimate of the uncertainties beyond those from the Gaussian model.

The measurements are reviewed visually with the help of the bars and slope indicators such as those shown on both panels of Figure 4.2. Plots and tables of all measurements can be found online at github.com/mef51/SurveyFRB20121102A.

4.4 Results

We describe the results of the autocorrelation analysis, the measurement filtering process, and the relationships between the spectro-temporal properties in this section. The sub-burst slope (normalized by the observing frequency) vs. sub-burst duration is shown in Figure 4.3. Figures 4.4 to 4.6 show different (potential) correlations between the measured spectro-temporal properties, including the sub-burst duration and sub-burst slope with frequency, and in particular the correlations between the bandwidth with frequency, duration and sub-burst slope. Figure 4.5 examines the small sample of bursts with multiple components and shows the drift rate vs. duration and drift rate vs. frequency. In Figure 4.6 we find an unexpected correlation between the bandwidth and duration (and

Dataset	Max valid DM (pc/cm ³)	Optimal DM (pc/cm ³)	# of bursts
Michilli et al. (2018)	560.0	558.0	19
Gajjar et al. (2018)	563.5	557.5	21
Oostrum et al. (2020)	563.0	563.0	23
Aggarwal et al. (2021)	560.5	559.5	63
Li et al. (2021)	562.0	562.0	41
Weighted Average:	561.5(4)	560.1(8)	167

Table 4.1: Results from the measurement exclusion and DM optimization process described in Section 3. The maximum valid DM is the DM beyond which bursts start being excluded for having invalid sub-burst slope measurements (ie. being over-dedispersed). The optimal DM is the DM for which the reduced- χ^2 of the fit between the sub-burst slope and duration measurements at that DM is closest to unity. The DM step size used was 0.5 pc/cm³.

thus sub-burst slope). Finally we look in particular at the spectro-temporal features of bursts from Li et al. (2021) in Figure 4.7 and the absence of correlations between bursts from different energy and wait-time peaks.

As mentioned in the previous section, the measurements are filtered to exclude invalid values and this process results in some bursts not having a valid measurement at a particular DM, which results in a limited DM range after requiring that all bursts are included. After this filtering, the ranges of DMs for which bursts have valid measurement varied from dataset to dataset; while all five datasets had valid measurements down to 555 pc/cm³, the highest DMs at which all bursts in a dataset still had valid measurements differed. These maximal DMs along with the DM in that range that had the optimal fit between the sub-burst slope and duration are listed in Table 4.1. The average maximal DM (weighted by the number of bursts in each dataset) was 561.5(4) pc/cm³ and the average optimal DM was 560.1(8) pc/cm³. In the figures to follow, burst measurements are always displayed at the optimal DM of the dataset they come from, with uncertainties estimated from the range of measurements found within the limited DM range.

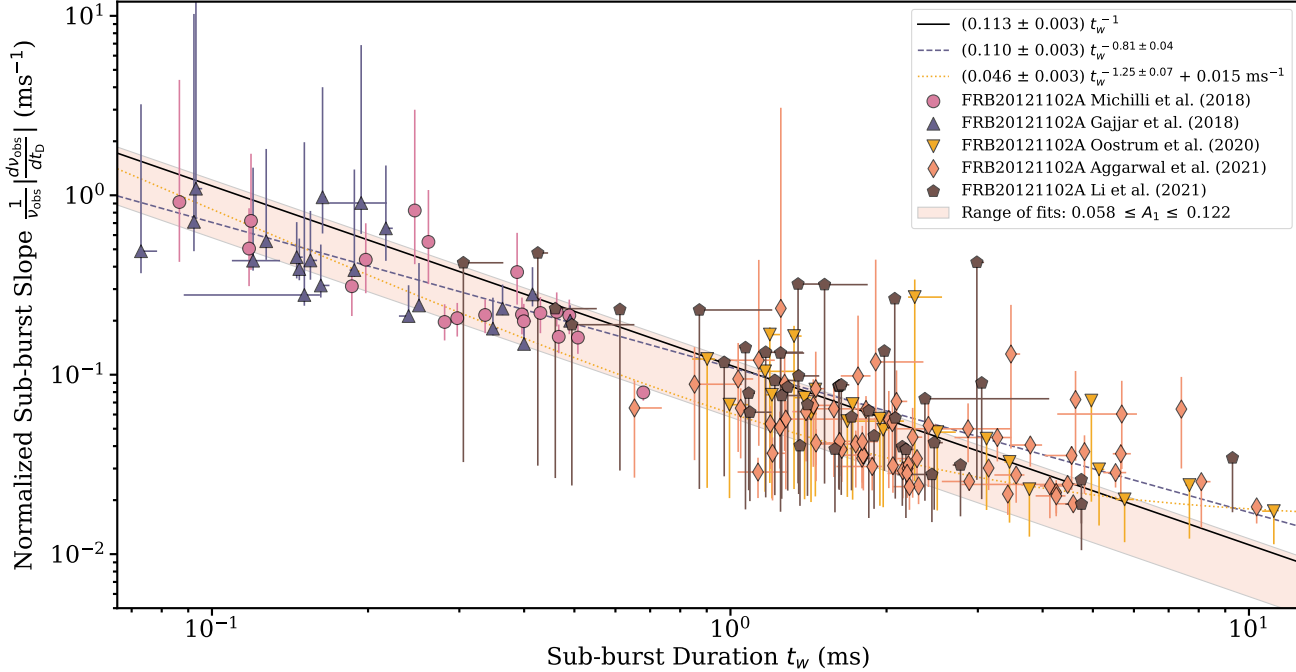


Figure 4.3: The relationship between the sub-burst slope and sub-burst duration. The sub-burst slope is normalized by the observed sub-burst frequency in order for the different datasets to be plotted together with the same relationship. The black line is a fit of the form $A t_w^{-1}$ which is the relationship predicted in the triggered relativistic dynamical model of Rajabi et al. (2020), while the other are more general fits of the form $A t_w^n$ and $A t_w^n + B$. The shaded region shows the intersection of the range of fits found over the DM ranges of each of the five datasets. Each measurement is displayed at the optimal DM for its source dataset, listed in Table 4.1. Uncertainty bars show the range of measurements found over the limited DM range (see Section 4.3). We see decent agreement between the three fits with the exponent of the expected relation lying between those found for the general fits.

4.4.1 Spectro-temporal Properties

The correlations between the spectro-temporal properties shown in Figures 4.3 to 4.6 confirm known relationships across a broad parameter range and reveal a potentially new relationship between the bandwidth and sub-burst duration (or normalized sub-burst slope). A summary of the fits found is shown in Table 4.2. A discussion of these results will be found in Section 4.5.

In Figure 4.3 we plot the sub-burst slope normalized by the observing frequency versus the sub-burst duration. We find three fits to the data using the `scipy.odr` package,

#	Form	A	n	C	Figure
1	$\frac{1}{\nu_{\text{obs}}} \frac{d\nu_{\text{obs}}}{dt_{\text{D}}} = A_1 t_{\text{w}}^{-1}$	0.113 ± 0.003			4.3
2	$\frac{1}{\nu_{\text{obs}}} \frac{d\nu_{\text{obs}}}{dt_{\text{D}}} = A_2 t_{\text{w}}^{n_2}$	0.110 ± 0.003	-0.81 ± 0.04		4.3
3	$\frac{1}{\nu_{\text{obs}}} \frac{d\nu_{\text{obs}}}{dt_{\text{D}}} = A_3 t_{\text{w}}^{n_3} + C_3$	0.046 ± 0.003	-1.25 ± 0.07	0.015 ms^{-1}	4.3
4	$t_{\text{w}} = A_4 \nu_{\text{obs}}^{-1}$	$1474 \pm 48 \text{ ms} \cdot \text{MHz}$			4.4
5	$t_{\text{w}} = A_5 \nu_{\text{obs}}^{n_5}$	283 ± 331	-0.80 ± 0.14		4.4
5b	$t_{\text{w}} = A_{5b} \nu_{\text{obs}}^{-2}$	$(5.9 \pm 0.3) \times 10^6 \text{ ms} \cdot \text{MHz}^2$			4.4
6	$\frac{d\nu_{\text{obs}}}{dt_{\text{D}}} = A_6 \nu_{\text{obs}}^2$	$(6.3 \pm 0.3) \times 10^{-5} \text{ ms}^{-1} \cdot \text{MHz}^{-1}$			4.4
7	$\frac{d\nu_{\text{obs}}}{dt_{\text{D}}} = A_7 \nu_{\text{obs}}^{n_7}$	$(1 \pm 2) \times 10^{-4}$	1.93 ± 0.23		4.4
8	$\frac{1}{\nu_{\text{obs}}} \frac{\Delta\nu_{\text{obs}}}{\Delta t_{\text{D}}} = A_8 t_{\text{w}}^{-1}$	0.145 ± 0.012			4.5
9	$\frac{1}{\nu_{\text{obs}}} \frac{\Delta\nu_{\text{obs}}}{\Delta t_{\text{D}}} = A_9 t_{\text{w}}^{n_9}$	0.119 ± 0.012	-0.71 ± 0.1		4.5
10	$\frac{\Delta\nu_{\text{obs}}}{\Delta t_{\text{D}}} = A_{10} \nu_{\text{obs}}^2$	$(2.1 \pm 0.2) \times 10^{-5} \text{ ms}^{-1} \cdot \text{MHz}^{-1}$			4.5
11	$\frac{\Delta\nu_{\text{obs}}}{\Delta t_{\text{D}}} = A_{11} \nu_{\text{obs}}^{n_{11}}$	$(1.3 \pm 0.8) \times 10^{-4}$	1.77 ± 0.08		4.5
12	$B_{\nu} = A_{12} \nu_{\text{obs}}$	0.14 ± 0.004			4.6
13	$B_{\nu} = A_{13} \nu_{\text{obs}}^{n_{13}}$	0.48 ± 0.16	0.85 ± 0.04		4.6
14	$B_{\nu} = A_{14} t_{\text{w}}^{n_{14}}$	272 ± 12	-0.53 ± 0.04		4.6
15	$B_{\nu} = A_{15} \left(\frac{1}{\nu_{\text{obs}}} \frac{d\nu_{\text{obs}}}{dt_{\text{D}}} \right)^{n_{15}}$	1225 ± 93	0.52 ± 0.05		4.6
16	$B_{\nu} = A_{16} t_{\text{w}}^{-1}$	$162 \pm 6 \text{ ms} \cdot \text{MHz}$			4.6
17	$B_{\nu} = A_{17} \left(\frac{1}{\nu_{\text{obs}}} \frac{d\nu_{\text{obs}}}{dt_{\text{D}}} \right)$	$2570 \pm 108 \text{ ms}$			4.6

Table 4.2: A summary of fits attempted with the measurement results. A typically denotes the amplitude of some kind of power-law, n denotes the index of that power law, and C is used to denote any additive constants when applicable. ν_{obs} denotes the sub-burst frequency, t_{w} denotes the sub-burst duration, and $(d\nu_{\text{obs}}/dt_{\text{D}})$ and $(\Delta\nu_{\text{obs}}/\Delta t_{\text{D}})$ denote the sub-burst slope and drift rate between multiple sub-bursts, respectively.

which performs an orthogonal distance regression, a method that takes into account the uncertainties on both variables. We use the range of measurements over the DM range as the variable uncertainties when performing the fits. The first fit is of the form $(d\nu_{\text{obs}}/dt_{\text{D}})/\nu_{\text{obs}} = A_1 t_{\text{w}}^{-1}$ which is the prediction of the TRDM and we find $A_1 = 0.113 \pm 0.003$. We fit two general power-laws, which are free of assumptions, of the form $A_2 t_{\text{w}}^{n_2}$ and $A_3 t_{\text{w}}^{n_3} + C_3$ to see if they agree with the predicted fit. These yield $A_2 = 0.110 \pm 0.003$, $n_2 = -0.81 \pm 0.04$ and $A_3 = 0.046 \pm 0.003$, $n_3 = -1.25 \pm 0.07$, $C_3 = 0.015 \text{ms}^{-1}$. For each dataset, a range of fits of the form $A t_{\text{w}}^{-1}$ is found over the DM range and the shaded region shows the intersection of those ranges across the five datasets. That is, the shaded region shows the range of fits possible within the limited DM ranges of all the datasets and is an estimate of the uncertainty on the parameter A_1 found above as a function of the DM. We see that a majority of points fall within this region and are well described by the fits, with a small population of outliers located above the rest of the points in the sub-bursts with durations greater than 1 ms. We also see the measurement ranges systematically tending to smaller sub-burst slopes with increasing duration.

In Figure 4.4, we plot the sub-burst duration and sub-burst slope against the frequency. In those two panels, the black line represents a fit of the form with the exponent fixed to the prediction of the TRDM and the tan line represents a fit where the exponent is free to vary. In the sub-burst duration vs. frequency plot, the black fit is of the form $A_4 \nu_{\text{obs}}^{-1}$, while the tan fit leaves the index free and is of the form $A_5 \nu_{\text{obs}}^{n_5}$. The free fit finds an exponent of $n_5 = -0.80 \pm 0.14$, smaller than the predicted $n = -1$, with $A_4 = 1474 \pm 48 \text{ms} \cdot \text{MHz}$ and $A_5 = 283 \pm 331$. The yellow fit is of the form $A_{5b} \nu_{\text{obs}}^{-2}$, and will be discussed in Section 4.5.2. In the sub-burst slope vs. frequency plot we fit to the TRDM form of $A_6 \nu_{\text{obs}}^2$ and again to a free index form of $A_7 \nu_{\text{obs}}^{n_7}$, finding $A_6 = (6.3 \pm 0.3) \times 10^{-5} \text{ms}^{-1} \cdot \text{MHz}^{-1}$, $A_7 = (1 \pm 2) \times 10^{-4}$ and an index of $n_7 = 1.93 \pm 0.23$, consistent with the predicted $n = 2$ relationship. Both fits visually describe the data well, and we see a large spread in the bursts in both plots.

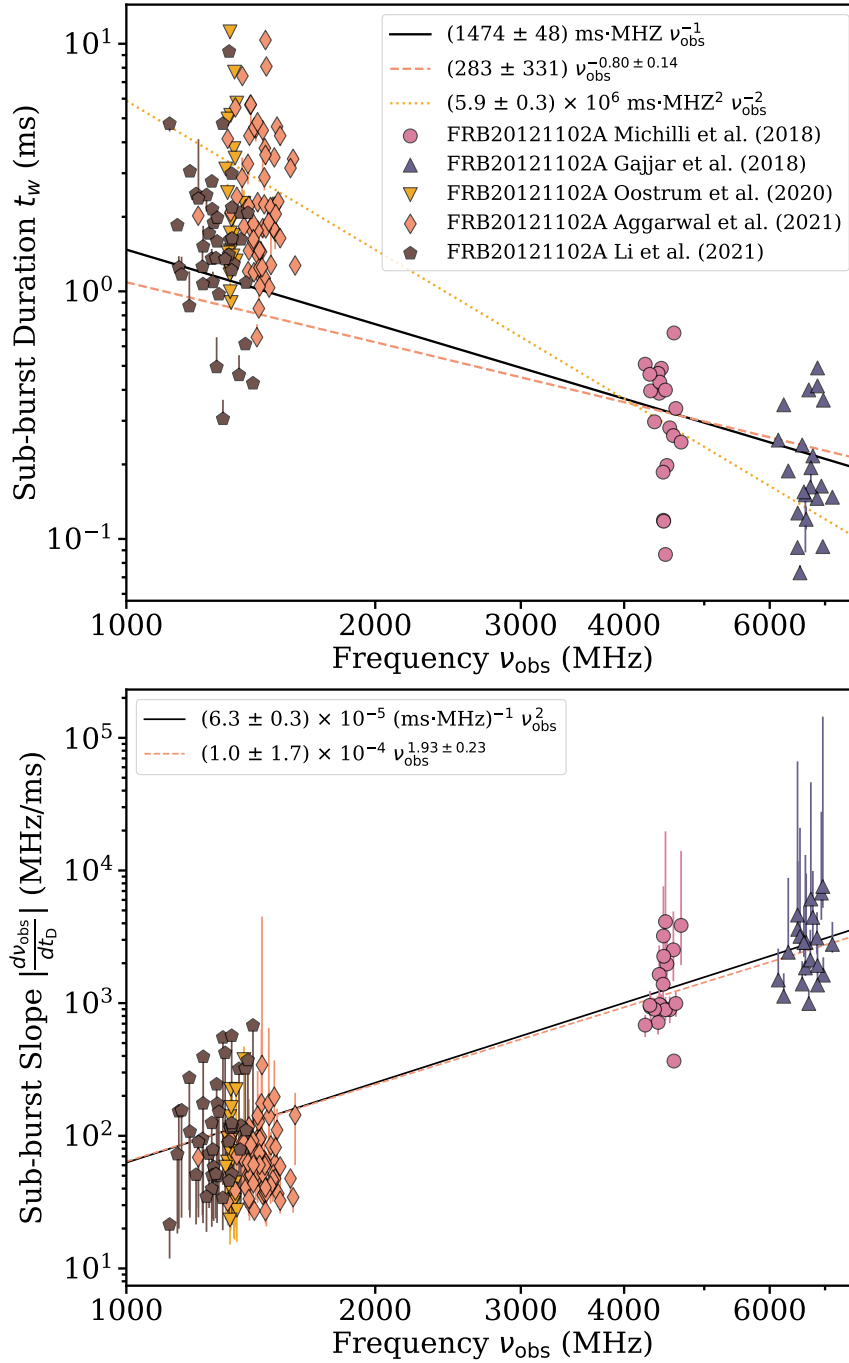


Figure 4.4: Relationships between the sub-burst duration (top) and the sub-burst slope (bottom) with burst frequency. Colors for all are shown in the top panel and are the same as in Figure 4.3. In the top and bottom panels, the black line shows a fit to the relationship predicted by the triggered relativistic dynamical model in Rajabi et al. (2020), and the tan lines are general fits of the form $A\nu_{\text{obs}}^n$.

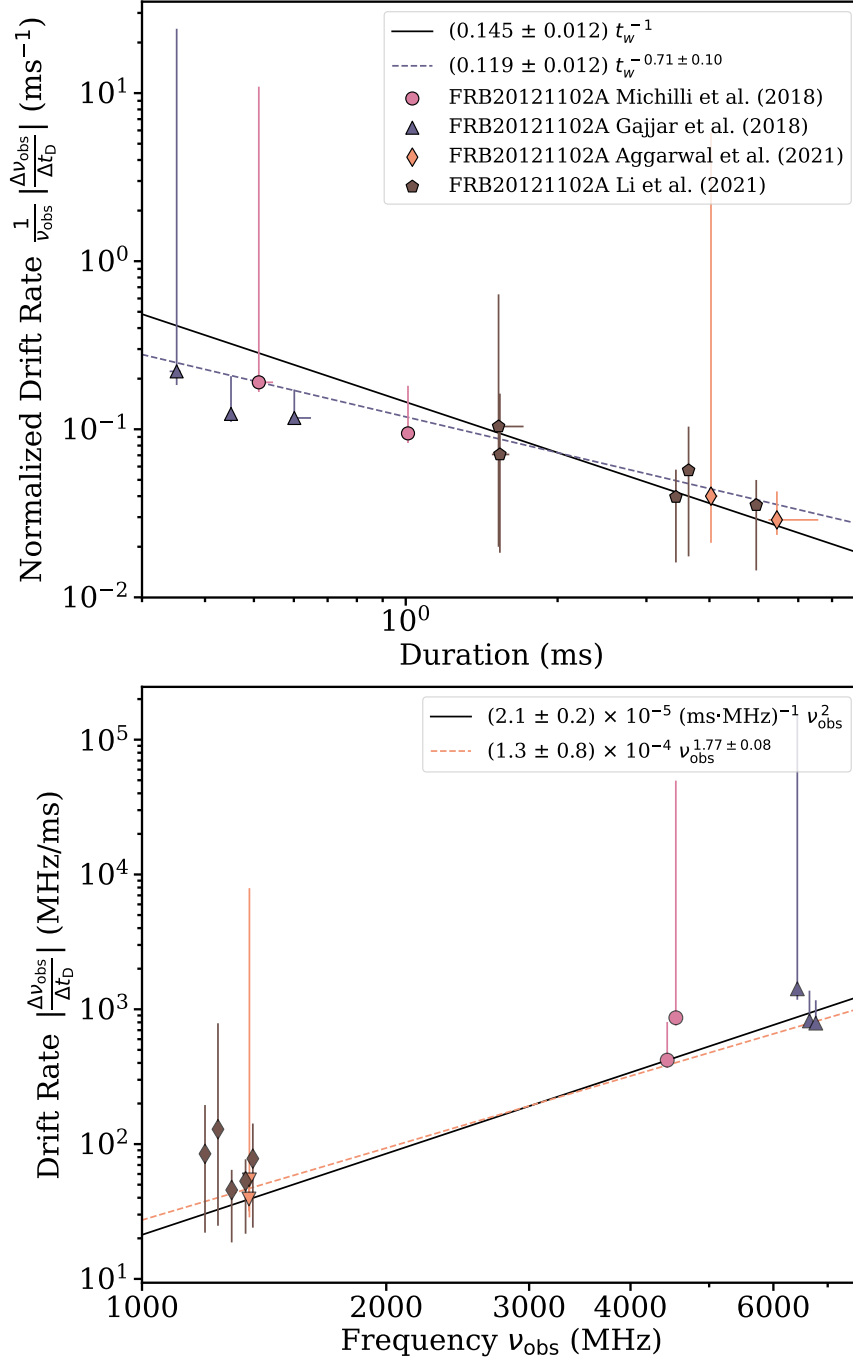


Figure 4.5: Relationships between the drift rate of multiple components and the duration (top) and the frequency of observation (bottom). On the left, fits of the form $A t_w^{-1}$ and $A t_w^n$ are made for comparison with the similar inverse relationship between the frequency-normalized sub-burst slope and duration shown in Figure 4.3. On the right, we find two fits with one locked to a power of 2 and the other allowed to change.

The drift rate of a burst with multiple components may be due to a different phenomenon than that which results in the sub-burst slope, and so we separate the drift rate measurements from the sub-burst slope measurements and show their correlations in Figure 4.5. We find that their relationships are similar to those found for the sub-burst slopes.

Of our sampled bursts only a handful showed multiple components. Most of these were measurable via the autocorrelation method but a few were not, such as in the cases where one of the bursts dominated the autocorrelation or when the drift rate was very small. The drift rates are put through the same filtering process as the sub-burst slopes and the top panel of Figure 4.5 shows the normalized drift rate vs. the duration of the event, while the bottom shows the drift rate vs. the frequency. As before, for the relationship with the duration we find one fit with the predicted form $A_8 t_w^{-1}$ which yielded $A_8 = 0.145 \pm 0.012$ and a fit with a free exponent of the form $A_9 t_w^{n_9}$ which yielded $A_9 = 0.119 \pm 0.012$ and $n_9 = -0.71 \pm 0.1$. This first fit has an A value higher than that found for the sub-burst slopes ($A_8 > A_1$) and outside the range of fits shown in Figure 4.3. The second fit found an exponent n_9 with a smaller magnitude than n_2 , the corresponding index for the sub-burst slopes. This suggests a relationship for the drift rates and duration similar to that found for the sub-burst slopes but with possibly a slightly different scaling.

For the relationship between the drift rates and the frequency (bottom panel of Figure 4.5) we perform two fits, with the first fit of the TRDM form $A_{10} \nu_{\text{obs}}^2$ yielding $A_{10} = (2.1 \pm 0.2) \times 10^{-5} \text{ ms}^{-1} \cdot \text{MHz}^{-1}$, which is about a third the value found between the sub-burst slope and frequency (A_6 , and shown in the bottom panel of Figure 4.4). A fit of the form $A_{11} \nu_{\text{obs}}^{n_{11}}$ found $A_{11} = (1.3 \pm 0.8) \times 10^{-4}$ and $n_{11} = 1.77 \pm 0.08$, with quite a large uncertainty on A_{11} . For the limited drift rates available, the fits to the drift rates' relationships are similar enough to those found for the sub-burst slopes that it is tempting to conclude that the same phenomena is responsible for both.

Figure 4.6 shows plots of the sub-burst bandwidth against the frequency, sub-burst duration, and normalized sub-burst slope, respectively. For the bandwidth versus frequency plot we find a linear fit of the form $A_{12} \nu_{\text{obs}}$ consistent with Doppler broadening of narrowband emission and a free index fit of the form $A_{13} \nu_{\text{obs}}^{n_{13}}$. This yields $A_{12} = 0.14 \pm 0.004$ and a fit with $A_{13} = 0.48 \pm 0.16$ and exponent $n_{13} = 0.85 \pm 0.04$. For the fits to bandwidth versus the sub-burst duration and normalized slope (middle and right panels), we leave the exponent free and use the forms $A_{14} t_w^{n_{14}}$ and $A_{15} (\nu_{\text{obs}}^{-1} d\nu_{\text{obs}}/dt_D)^{n_{15}}$. We find $A_{14} = 272 \pm 12$ and $n_{14} = -0.53 \pm 0.04$ for the duration and $A_{15} = 1225 \pm 93$ and $n_{15} = 0.52 \pm 0.05$ for the normalized sub-burst slope. Plotting against the sub-burst slope instead of the normalized sub-burst slope has little effect on the exponent n_{15} . That the exponents n_{14} and n_{15} are inverses of each other within the uncertainties is expected from the inverse trend between the slope and duration shown in Figure 4.3, in agreement with the prediction of the TRDM.

That there is a relationship between the bandwidth and duration or slope of a burst can be expected from the other correlations shown but, as will be discussed in Section 4.5.2, the exact form of relationship seen here is not, and is visible in these data because of the large range in frequency of the bursts sampled. However, as shown by the bandwidth limits plotted as regions in the figures, the maximum observable bandwidths for the Oostrum et al. (2020), Aggarwal et al. (2021), and Li et al. (2021) datasets are 200 MHz, 680 MHz, and 500 MHz, respectively, due to their instrumentation (with a few exceptions for bursts that had slightly different backends), implying that sub-bursts with high bandwidths and long durations could be missed.

The nearest and simplest fractional value consistent with the uncertainties of the exponent $n_{14} = -0.53 \pm 0.04$ is $-1/2$ and so the two rightmost panels of Figure 4.6, observationally complete, suggest a proportionality of $B_\nu \propto t_w^{-1/2} \propto (\nu_{\text{obs}}^{-1} d\nu_{\text{obs}}/dt_D)^{1/2}$, where B_ν is the bandwidth. The colored lines in the two rightmost panels show fits of the form $A_{16} t_w^{-1}$ and $A_{17} (\nu_{\text{obs}}^{-1} d\nu_{\text{obs}}/dt_D)$, respectively, with $A_{16} = 162 \pm 6$ ms·MHz and

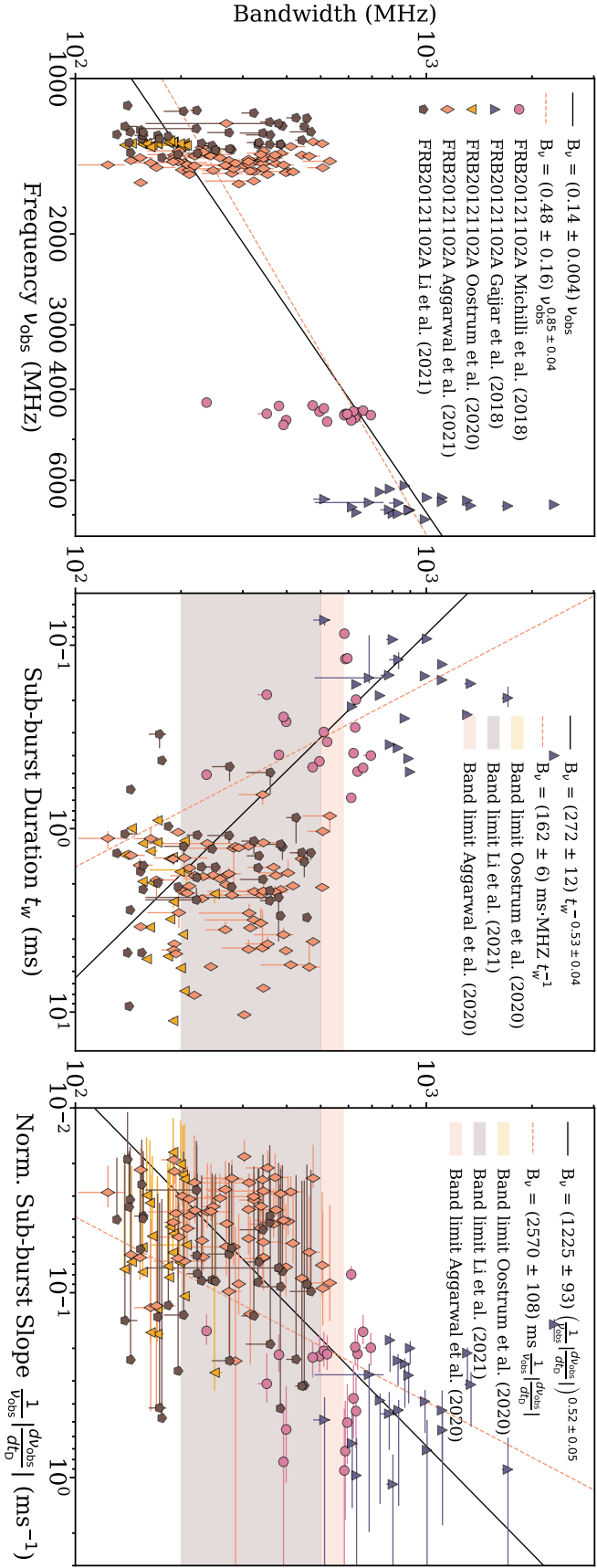


Figure 4.6: Relationships between the bandwidth and the burst frequency (left), sub-burst duration (middle) and sub-burst slope (right). The relationship between the bandwidth and frequency is linear, while the relationship with the duration goes, within uncertainties, to the power of $-1/2$. The origin of this relationship is unclear, and may be due to observational bias as indicated by the overlaid regions showing the bandwidth limits. In the right panel we see that the fit found between the bandwidth and slope is the inverse of that for the duration, as might be expected based on their inverse relationship shown in Figure 4.3.

$A_{17} = 2570 \pm 108$ ms. These are the expected relationships inferred from our earlier results to be discussed in Section 4.5.2 where we also further explore this unusual dependence.

The set of correlations described above provide evidence that the relationships predicted by the TRDM between the sub-burst duration, slope and frequency apply for a majority of bursts from this source and possibly indicate an additional unknown relationship between the bandwidth and sub-burst slope/duration.

For the sampled bursts from the bimodal peaks in energy and wait-time distributions reported by Li et al. (2021), we searched for correlations between our measured spectro-temporal properties and the burst energy and wait-time, finding that they were unrelated to each other. Figure 4.7 shows plots of the slope, sub-burst duration, bandwidth, and frequency as functions of the wait-time (top row) and burst energy (bottom row). In the top row we can see that the bursts cluster around wait-times of 10^{-2} and 10^2 seconds, corresponding to the two sampled peaks, and that the spectro-temporal measurements in all panels vary randomly and with similar ranges. In the bottom row a large number of bursts cluster around 10^{39} erg while the low energy peak at $< 10^{38}$ erg only has two points, due to difficulties we encountered in measuring these lower S/N bursts. Nonetheless, across the four panels we again see that the measurements vary widely at the high energy peak and cover similar values as the measurements from the low energy peak. For this limited sample of data we therefore conclude that no clear relationship exists between the wait-time and energy of a burst with any of its spectro-temporal properties.

We have presented in this section new measurements of the spectro-temporal properties of bursts sampled from five studies of FRB 20121102A and characterized the relationships, and lack of relationships, between them. Across this broad sample we saw that the sub-burst slope and sub-burst duration are inversely related, shown in Figure 4.3. We see that the sub-burst duration and frequency are also inversely (or potentially inverse squared) related, that the sub-burst slope goes to the square of the frequency, and that the bandwidth varies linearly with the frequency. We also looked at a handful

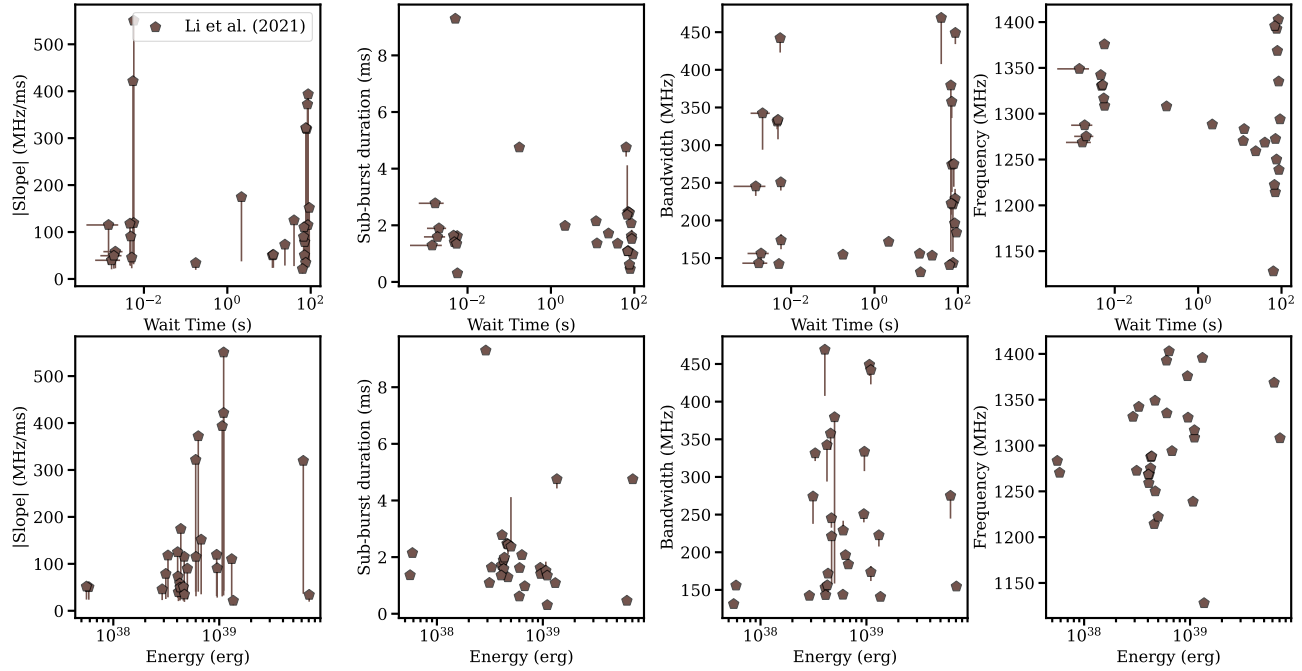


Figure 4.7: Search for correlations between measured spectro-temporal properties of 28 bursts from Li et al. (2021) and their wait-times (top) and energies (bottom), as reported by those authors. This figure does not include the 13 sub-bursts that were separated ourselves. The two peaks of the wait-time distributions can be seen in the top row around 10^{-2} and 10^2 seconds. The two peaks of the energy distribution are less obvious due to difficulties measuring bursts from the low energy ($< 10^{38}$ erg) peak and the small sample limits the possible conclusions. No obvious dependence of a burst's spectro-temporal properties on either its wait-time or energy is seen in these data.

of drift rates in our sample separately from measurements of the sub-burst slope and found similar but not identical relationships as those found for the sub-burst slope. Due to the low statistics it is unclear whether different relationships describe the sub-burst slope and drift rate or if they are identical, but nonetheless the relationships between the two are certainly difficult to distinguish. We tentatively found a relationship between the bandwidth and sub-burst duration with a proportionality consistent with $t_w^{-1/2}$. Because of the inverse relationship between the duration and normalized sub-burst slope, we therefore expect a relationship between the bandwidth and sub-burst slope that goes nearly as $[(d\nu_{\text{obs}}/dt_D)/\nu_{\text{obs}}]^{1/2}$, and this is exactly what is seen in the right panel of Figure 4.6. Finally, by looking at bursts sampled from the bimodal energy and wait-time distributions reported by Li et al. (2021), we see no connection between those two parameters and the subsequent spectro-temporal properties of a burst, though the sample size is small especially for the low energy peak.

4.5 Discussion

We discuss here our results in the context of other studies and the TRDM, including the expected relationships for the drift rates and their connection to those for the sub-burst slopes. We will also discuss the unexpected relationship observed between the bandwidth, duration, and normalized sub-burst slope, the implications of the relationships observed (and not observed, in the case of the spectro-temporal properties with the burst energy and wait-time), as well as the large spread in values seen in the measurements of the spectro-temporal properties and what these results mean for understanding FRBs overall.

Several studies have now closely examined the relationships between spectro-temporal properties of FRBs and found strong correlations between them, especially between the normalized sub-burst slope and sub-burst duration. The first report of the inverse relationship between the slope and duration was in Rajabi et al. (2020), seen with 25 bursts

from FRB 20121102A. Chamma et al. (2021) reported the same relationship for multiple sources seen with bursts from, in addition to FRB 20121102A, FRB20180916B and FRB20180814A, while also reporting that the same fit parameter A characterized the relationship for the three sources. In earlier work the data for FRB 20121102A were limited to bursts with short durations and frequencies greater than 4 GHz, and since then large numbers of bursts were made available at longer durations and lower frequencies, presenting the opportunity to understand the relationships seen earlier with improved statistics.

In this study the frequency and duration ranges are broad and the number of bursts studied from FRB 20121102A is large enough to conclude that a majority of bursts from this source follow a tight relationship between the normalized sub-burst slope and duration. The optimum fit parameter found here was $A_1 = 0.113 \pm 0.003$, which is higher than the $A = 0.078 \pm 0.006$ found by Chamma et al. (2021), along with a narrower range of fits centered around $A = 0.09$. Though the range of fits includes this earlier value, the low frequency bursts added in this study exhibit a small population of outliers that are found higher than the fit region, which may be responsible for the larger A value found here. Based on the uncertainty ranges, this population can be seen to be near the edge of its limited DM range, meaning the bursts are near vertical where errors on the slope measurement are large and close to being over-dedispersed. For most of the outliers, their ranges extend into the main population of bursts.

In Jahns et al. (2022), 849 bursts from FRB 20121102A were analysed on the lower end of our frequency range (around 1400 MHz) and a strong inverse correlation between the sub-burst duration and slope can be seen in their Figure 5. Their formalism finds the inverse of the sub-burst slope relation used here and their fit parameter of $|b| = 0.00862(37)$ MHz⁻¹ can be converted to the results here for comparison via $A = 1/(\nu_{\text{obs}}b)$, which yields $A_{\text{Jahns}} = 0.0839$ when using $\nu_{\text{obs}} = 1400$ MHz, the most common burst frequency in that sample. This value is comparable to the results found here, and differences can be due

to the burst definition used and details of the analysis (such as normalizing each point by the burst frequency).

Studies focused on a narrow range of frequencies and durations can have limited power in revealing statistical relations between properties, such as the near inverse relationship between sub-burst duration and frequency, and near quadratic relationship between sub-burst slope and frequency, shown in the two panels of Figure 4.4. The TRDM predicts the relationship between the sub-burst duration and frequency to be

$$t_w = \tau'_w \frac{\nu_0}{\nu_{\text{obs}}}, \quad (4.5)$$

where t_w is the sub-burst duration, τ'_w is the sub-burst duration in the rest frame of emission, ν_0 is the rest frame frequency, and ν_{obs} is the frequency in the observer frame. The values of τ'_w and ν_0 can be absorbed into a constant and so an inverse relationship is expected. Other evidence of this relationship can be found in Figure 7 of Gajjar et al. (2018) and Figure 3 of Hessels et al. (2019). Each ‘clump’ of bursts seen in Figure 4.4 viewed independently appears uncorrelated with the observing frequency, but placed together a downward trend becomes clear.

The relationship between sub-burst slope and frequency is similar in this regard as well, since over a narrow spectral range the two observables can appear uncorrelated. Wang et al. (2022) in their Figure 8 using data from multiple studies and multiple FRB sources and spanning a large frequency range found that trends proportional to ν^2 and $\nu^{2.29}$ fit the data well. A quadratic relationship between sub-burst slope and frequency was previously implied by the results of Chamma et al. (2021) in their Figure 5. Our results here show similar relationships fit well, with the free exponent fit finding a value of $\nu^{1.93 \pm 0.23}$ that is quadratic within the uncertainty.

The relationship between the sub-burst slope and frequency was derived in Chamma et al. (2021) from the TRDM using equation (4.5) and the relationship between the

sub-burst slope and duration, and is given by

$$\frac{1}{\nu_{\text{obs}}} \frac{d\nu_{\text{obs}}}{dt_{\text{D}}} = - \left(\frac{\tau'_{\text{w}}}{\tau'_{\text{D}}} \right) \frac{1}{t_{\text{w}}} = - \frac{A}{t_{\text{w}}}, \quad (4.6)$$

where as before $d\nu_{\text{obs}}/dt_{\text{D}}$ is the sub-burst slope, t_{D} is the delay time (or arrival time), and τ'_{D} is the delay time in the rest frame of the FRB. The fit parameter A is seen here as the ratio between the rest frame sub-burst duration and delay time, and this relationship is the one predicted for the sub-burst slope and duration, shown with the black fit in Figure 4.3. Combining equations (4.5) and (4.6) we obtain

$$\frac{d\nu_{\text{obs}}}{dt_{\text{D}}} = - \frac{A\nu_{\text{obs}}^2}{\tau'_{\text{w}}\nu_0} \equiv -A_6 \nu_{\text{obs}}^2, \quad (4.7)$$

where the new constant $A_6 = A/(\tau'_{\text{w}}\nu_0) = 1/(\tau'_{\text{D}}\nu_0)$. This is a quadratic relationship between the sub-burst slope and frequency and is shown by our results as well as the results of Chamma et al. (2021) and Wang et al. (2022).

The TRDM assumes a fundamentally narrow-band emission process at a rest frame frequency ν_0 and if the rest frame sub-burst duration τ'_{w} can be estimated with a more detailed model of the emission process, then the ratio of A and A_6 would provide a measure of ν_0 , through

$$\frac{A}{A_6} = \nu_0 \tau'_{\text{w}}. \quad (4.8)$$

For example using our results of $A_1 = 0.113 \pm 0.003$ and $A_6 = (6.3 \pm 0.3) \times 10^{-5} \text{ ms}^{-1} \cdot \text{MHz}^{-1}$ and with an order of magnitude estimate of $\tau'_{\text{w}} \approx 1 \text{ ms}$, we can very roughly estimate ν_0 to be on the order 1 GHz. The relationships between the sub-burst slope, duration and frequency are difficult to characterize without a broad sample of observations, but if those data are available such as with FRB 20121102A, they serve as useful tools especially in the context of the TRDM.

The TRDM offers a simple explanation for the relationships observed by assuming a narrow-band emission process for FRBs at a common rest frame frequency ν_0 .

4.5.1 Drift rate vs duration and frequency

As discussed in Section 4.4, the drift rate relationships with duration and frequency are plotted in Figure 4.5 and these relationships appear to be analogous to those for the sub-burst slope. For the limited data available, the drift rate relationship with frequency seems to be adequately described by the fit proportional to ν_{obs}^2 , as the free fit is proportional to $\nu_{\text{obs}}^{1.77}$, which is closer to quadratic than not. We can derive a relationship between the drift rate and the frequency using equation 8 of Rajabi et al. (2020), which describes the change in frequency with arrival time of distinct sub-bursts. Expanding the $d\nu_{\text{obs}}/d\tau'_D$ term in that equation we get

$$\frac{\Delta\nu_{\text{obs}}}{\Delta t_D} = \frac{\nu_{\text{obs}}}{\nu_0} \frac{d\nu_{\text{obs}}}{d\tau'_D} = \frac{\nu_{\text{obs}}}{\nu_0} \frac{d\nu_{\text{obs}}}{d\beta} \frac{d\beta}{d\tau'_D}, \quad (4.9)$$

where β is the fraction of the speed of light the FRB source is moving with along the line of sight. By using the relativistic Doppler shift formula $\nu_{\text{obs}} = \nu_0 \sqrt{(1 + \beta)/(1 - \beta)}$, we can evaluate $d\nu_{\text{obs}}/d\beta$ in the above expression to obtain

$$\frac{\Delta\nu_{\text{obs}}}{\Delta t_D} = \frac{\nu_{\text{obs}}^2}{\nu_0} \gamma^2 \frac{d\beta}{d\tau'_D}, \quad (4.10)$$

where $\gamma = 1/\sqrt{1 - \beta^2}$. Equation (4.10) shows a ν_{obs}^2 dependence with the frequency with $\gamma^2 d\beta/d\tau'_D$ a parameter characterizing the region under study. More data are required to what relationship exists between the drift rate and frequency, and the result of such an analysis can be interpreted within the model based on the relations described above. The data also seem to suggest an inverse relationship analogous to the relationship between the sub-burst slope and sub-burst duration. As mentioned earlier, this can be expected in the TRDM when groups of sub-bursts are emitted at roughly the same time (Sec. 3.1

of Chamma et al. 2021; Rajabi et al. 2020).

4.5.2 Bandwidth vs. Sub-burst Duration relationship

The correlations of spectro-temporal properties with the bandwidth shown in Figure 4.6 reveal known as well as unknown relationships. One known spectro-temporal correlation seen in FRBs is the scaling of bandwidth with frequency. For example, in Houde et al. (2019), the linear relationship shown in the top panel of Figure 4.6 between bandwidth and frequency is seen in their Figure 5, and includes points between 2 and 4 GHz. Their slope, once converted for comparison is 0.156, close to the value $A_{12} = 0.14 \pm 0.004$ obtained here. This linear relationship between the bandwidth and frequency follows from the non- or weakly-relativistic Doppler effect (Houde et al. 2019).

The relationships found in the bottom panels of Figure 4.6 where $B_\nu \propto t_w^{-1/2}$ and $B_\nu \propto (d\nu_{\text{obs}}/dt_D)^{1/2}$ are unexpected, difficult to verify, and statistically significant enough to be considered real. Based on our results, the expected dependence is $B_\nu \propto t_w^{-1}$ because of the dependences $t_w \propto \nu_{\text{obs}}^{-1}$ (top panel of Figure 4.4) and $B_\nu \propto \nu_{\text{obs}}$ (top panel of Figure 4.6). Accordingly, the expected dependence between B_ν and $d\nu_{\text{obs}}/dt_D$ is linear. However, fits of the form $B_\nu \propto t_w^{-1}$ and $B_\nu \propto d\nu_{\text{obs}}/dt_D$, shown by the colored lines in the bottom panels of Figure 4.6, fail to simultaneously cross both the low frequency and high frequency bursts as well as the $B_\nu \propto t_w^{-1/2}$ and $B_\nu \propto (d\nu_{\text{obs}}/dt_D)^{1/2}$ fits do.

Because the bandwidth appears to be linear with frequency, we can perform a test fit on the sub-burst duration and frequency that assumes the form $t_w \propto \nu_{\text{obs}}^{-2}$ since this would imply a bandwidth-duration relationship of the form $B_\nu \propto t_w^{-1/2}$ consistent with our results. Indeed, the ν_{obs}^{-2} fit (shown in the first panel of Figure 4.4) is adequate enough of a fit that we cannot be entirely certain whether $t_w \propto \nu_{\text{obs}}^{-1}$ or $t_w \propto \nu_{\text{obs}}^{-2}$. However, we note that the relationship $t_w \propto \nu_{\text{obs}}^{-1}$ is at the basis for the sub-burst slope law, i.e., $(d\nu_{\text{obs}}/dt_D)/\nu_{\text{obs}} \propto t_w^{-1}$, through a simple derivative, and that this relation appears to be securely confirmed here and elsewhere (Rajabi et al. 2020; Chamma et al. 2021; Jahns

et al. 2022). Furthermore a combination of the sub-burst slope law with $t_w \propto \nu_{\text{obs}}^{-2}$ leads to a relationship $d\nu_{\text{obs}}/dt_D \propto \nu_{\text{obs}}^3$, which is not compatible with our results. That is, the relationship $d\nu_{\text{obs}}/dt_D \propto \nu_{\text{obs}}^2$ is clearly verified with the data. For these reasons we are inclined to favour a $t_w \propto \nu_w^{-1}$ relation and therefore conclude that the $B_\nu \propto t_w^{-1/2}$ functionality is real.

There is no known relationship within the TRDM that explains the $B_\nu \propto t_w^{-1/2}$ relationship between the bandwidth and the sub-burst duration, or the $B_\nu \propto [(d\nu_{\text{obs}}/dt_D)/\nu_{\text{obs}}]^{1/2}$ relationship between the bandwidth and sub-burst slope. If the velocity distribution of the FRB source, which determines the bandwidth in the TRDM, is an independent variable that helps in determining the sub-burst duration and sub-burst slope, then it is not clear what physical mechanism enables the velocity of one sample of material to determine the duration of the pulse emitted by material moving at a different velocity. Conversely, it is difficult to understand how the duration of a pulse t_w , which would imply a correlation bandwidth on the order $\sim 1/t_w$, could be physically related to an overall FRB bandwidth spanning a frequency range several orders of magnitude broader. The lack of a physical picture that explains this bandwidth-duration/slope relationship within the TRDM suggests that the explanation may be related to the physics of the emission process.

4.5.3 Spectro-temporal properties and their relationship to the emission process

Across the different relationships explored and the broad sample of bursts considered from FRB 20121102A, there does not seem to be a large population of outliers that breaks sharply from the relationships described. This fact, in light of the absence of correlations between the spectro-temporal properties and the energies and wait-times, suggests a separation between some of the spectro-temporal properties of an FRB and its emission mechanism. A simple interpretation for the lack of outliers or bursts classified by the

trend their spectro-temporal properties follow is that the correlations between properties like the sub-burst slope, duration and frequency of FRBs (at least from this source) originate from the relativistic dynamics of the source as explained by the TRDM. The correlation between the bandwidth and duration, unexplained in the TRDM as discussed above, falls into a different category.

The results presented here suggest that the FRB emission from this source comes from material that is moving relativistically, since several spectro-temporal correlations of FRB 20121102A are explainable through the dynamics of that material and the TRDM, and not due to the actual emission process.

This view is supported by the results shown in Figure 4.7, where several spectro-temporal properties appear uncorrelated with both the wait-time and energy of a burst. Further supporting examples are the plots with energy displayed in Figure 5 of Jahns et al. (2022) for bursts around 1400 MHz, the relationship between the frequency and flux density shown in Figure 4 of Gajjar et al. (2018) for bursts around 7 GHz, and plots of different properties with the fluence shown in Figure 5 of Aggarwal et al. (2021) for bursts around 1400 MHz, all of which imply no clear relationship between the spectro-temporal properties and burst energies.

These aforementioned studies are done independently over a narrow range of frequencies and durations. An analysis with a broad sample such as the one used for this study that focuses on the energy and/or fluxes of bursts would be needed to confirm the lack of correlation between burst energies and spectro-temporal properties such as the sub-burst slope or duration, as the present results and literature suggest.

There is considerable statistical spread in the values of sub-burst slope, duration and bandwidth seen in Figures 4.3 to 4.6 from each dataset that could be related to the emission process. For example, the data for Michilli et al. (2018) cluster around 4.5 GHz, but values for the sub-burst slope range from 5×10^2 MHz/ms to 4×10^3 MHz/ms, and the sub-burst duration spans nearly an order of magnitude. Similar statements are true

for all the other datasets considered. In the TRDM the sub-burst duration and sub-burst slope (see equations 4.5 and 4.6) are related to the rest frame frequency ν_0 , and the rest frame duration and delay times τ'_w and τ'_D . The dependence of the sub-burst duration and slope on these properties, which in the TRDM are determined exclusively by the emission process and FRB environment, is possibly the cause of the scatter seen in the spectro-temporal properties. Characterizing the scatter of spectro-temporal properties for large samples of bursts may therefore be an avenue for studying the emission process.

4.6 Conclusions

We studied the spectro-temporal properties and the relationships between them of a broad sample of 167 bursts from FRB 20121102A with frequencies ranging from 1 to 7.5 GHz and sub-burst durations ranging from less than 1 ms to about 10 ms from the observational studies of Michilli et al. (2018), Gajjar et al. (2018), Oostrum et al. (2020), Aggarwal et al. (2021), and Li et al. (2021). Bursts from the latter study were sampled from the two peaks of the bimodal energy and bimodal wait-time distributions reported therein in order to search for relationships between those parameters and the spectro-temporal properties of the bursts. Our measurements of the spectro-temporal properties include measurements of the sub-burst slope, sub-burst duration, burst bandwidth, center frequency, and scintillation drift rate (when applicable) at each DM between 555 to 575 pc/cm^3 in steps of 0.5 pc/cm^3 . The complete set of measurements are available online along with an extensible graphical user interface called FRBGUI that was developed and used to prepare and perform measurements on the burst waterfalls.

We characterized multiple relationships between the measured spectro-temporal properties of bursts from FRB 20121102A finding general agreement with multiple predictions from the TRDM described in Rajabi et al. (2020), which fundamentally assumes a narrow-band emission process and up-to relativistic motion. We found, as in Rajabi et al. (2020),

Chamma et al. (2021) and Jahns et al. (2022), an inverse relationship between the sub-burst slope and sub-burst duration. In addition, we find an inverse relation between the sub-burst duration and frequency, a quadratic relation between the sub-burst slope and frequency, and a linear relationship between the sub-burst bandwidth and frequency.

The 12 drift rates measured were seen to follow relationships with the duration and frequency that are analogous to the ones obeyed by the sub-burst slope. However, more drift rates are needed to properly characterize these trends.

We also found an unexpected correlation with power-law index consistent with $-1/2$ between the sub-burst bandwidth and sub-burst duration ($B_\nu \propto t_w^{-1/2}$), and because of the inverse relationship between the sub-burst slope and duration, a relationship between the bandwidth and sub-burst slope with power-law index consistent with $1/2$ ($B_\nu \propto [(d\nu_{\text{obs}}/dt_D)/\nu_{\text{obs}}]^{1/2}$). This relationship is unexplained and is potentially uncertain due to the limited observing bands at lower frequencies, however this would not explain the lack of small bandwidth, short duration sub-bursts observed at high frequencies.

We found no correlations between the spectro-temporal properties of a burst and its energy or wait-time.

Except for the bandwidth relationship with the normalized sub-burst slope and duration, the multiple relationships observed between the spectro-temporal properties generally agree with the predictions made in Rajabi et al. (2020). Therefore, more data are needed from FRB 20121102A between 2 and 4 GHz and high bandwidth bursts should be searched for at low frequencies (below 2 GHz), as well as low bandwidth bursts at high frequencies, in order to test the limits of the bandwidth-duration/slope relationship found.

The general agreement of the spectro-temporal properties with the predictions of the TRDM from this broad sample of bursts from FRB 20121102A suggests that several of the spectro-temporal relationships of all bursts from FRB 20121102A can be explained by dynamical motions of the FRB source. Meanwhile, the dispersion of values observed

in the spectro-temporal properties seems to arise from parameters in the model that are determined exclusively by the emission mechanism such as the rest frame frequency of emission and the rest frame timescales. Therefore, characterizing the dispersion of spectro-temporal properties from large samples of bursts may also inform on the emission mechanism of FRBs.

Acknowledgements

We are grateful to Di Li for arranging access to and support with the FAST data. The authors are grateful to Christopher Wyenberg for feedback and discussions on drafts of this manuscript. M.H.'s research is funded through the Natural Sciences and Engineering Research Council of Canada Discovery Grant RGPIN-2016-04460. Plots in the paper were prepared using the Matplotlib package (Hunter 2007).

Data Availability

All spectro-temporal measurements are available online at github.com/mef51/SurveyFRB20121102A. The waterfalls of the FRBs can be obtained from the authors of their respective publications. The graphical user interface FRBGUI and related scripts used to perform the measurements are available at github.com/mef51/frbgui.

Bibliography

- Agarwal, Devansh et al. (2020). “Initial results from a real-time FRB search with the GBT”. In: *Monthly Notices of the Royal Astronomical Society* 497.1, pp. 352–360. DOI: [10.1093/mnras/staa1927](https://doi.org/10.1093/mnras/staa1927).
- Aggarwal, Kshitij (2021). “Observational Effects of Banded Repeating FRBs”. In: *The Astrophysical Journal Letters* 920.1, p. L18. DOI: [10.3847/2041-8213/ac2a3a](https://doi.org/10.3847/2041-8213/ac2a3a).
- Aggarwal, Kshitij et al. (2021). “Comprehensive Analysis of a Dense Sample of FRB 121102 Bursts”. In: *The Astrophysical Journal* 922.2, p. 115. DOI: [10.3847/1538-4357/ac2577](https://doi.org/10.3847/1538-4357/ac2577).
- Amiri, M. et al. (2019). “A second source of repeating fast radio bursts”. In: *Nature* 566.7743, pp. 235–238. DOI: [10.1038/s41586-018-0864-x](https://doi.org/10.1038/s41586-018-0864-x). arXiv: [1901.04525](https://arxiv.org/abs/1901.04525) [astro-ph.HE]. URL: <https://ui.adsabs.harvard.edu/abs/2019Natur.566.235C>.
- Anna-Thomas, Reshma et al. (Feb. 22, 2022). “A Highly Variable Magnetized Environment in a Fast Radio Burst Source”. In: *arXiv*. arXiv: [2202.11112](https://arxiv.org/abs/2202.11112) [astro-ph.HE]. URL: <https://arxiv.org/abs/2202.11112>.
- Chamma, Mohammed A et al. (2021). “Evidence of a shared spectro-temporal law between sources of repeating fast radio bursts”. In: *Monthly Notices of the Royal Astronomical Society* 507.1, pp. 246–260. DOI: [10.1093/mnras/stab2070](https://doi.org/10.1093/mnras/stab2070).
- CHIME/FRB (2020). “Periodic activity from a fast radio burst source”. In: *Nature* 582.7812, pp. 351–355. DOI: [10.1038/s41586-020-2398-2](https://doi.org/10.1038/s41586-020-2398-2).

- Gajjar, V. et al. (2018). “Highest Frequency Detection of FRB 121102 at 4–8 GHz Using the Breakthrough Listen Digital Backend at the Green Bank Telescope”. In: *The Astrophysical Journal* 863.1, p. 2. DOI: [10.3847/1538-4357/aad005](https://doi.org/10.3847/1538-4357/aad005).
- Gourdji, K. et al. (2019). “A Sample of Low-energy Bursts from FRB 121102”. In: *The Astrophysical Journal* 877.2, p. L19. DOI: [10.3847/2041-8213/ab1f8a](https://doi.org/10.3847/2041-8213/ab1f8a).
- Hessels, J. W. T. et al. (2019). “FRB 121102 Bursts Show Complex Time–Frequency Structure”. In: *The Astrophysical Journal* 876.2, p. L23. DOI: [10.3847/2041-8213/ab13ae](https://doi.org/10.3847/2041-8213/ab13ae).
- Hilmarsson, G. H. et al. (2021). “Rotation Measure Evolution of the Repeating Fast Radio Burst Source FRB 121102”. In: *The Astrophysical Journal* 908.1, p. L10. DOI: [10.3847/2041-8213/abdec0](https://doi.org/10.3847/2041-8213/abdec0).
- Houde, Martin et al. (2019). “Triggered superradiance and fast radio bursts”. In: *Monthly Notices of the Royal Astronomical Society* 482.4, pp. 5492–5499. DOI: [10.1093/mnras/sty3046](https://doi.org/10.1093/mnras/sty3046).
- Hunter, John D. (May 2007). “Matplotlib: A 2D Graphics Environment”. In: *Computing in Science and Engineering* 9.3, pp. 90–95. DOI: [10.1109/MCSE.2007.55](https://doi.org/10.1109/MCSE.2007.55). URL: <https://ui.adsabs.harvard.edu/abs/2007CSE....9...90H>.
- Jahns, J. N. et al. (Feb. 11, 2022). “The FRB 20121102A November rain in 2018 observed with the Arecibo Telescope”. In: *arXiv*. arXiv: [2202.05705](https://arxiv.org/abs/2202.05705) [astro-ph.HE]. URL: <https://arxiv.org/abs/2202.05705>.
- Josephy, A. et al. (2019). “CHIME/FRB Detection of the Original Repeating Fast Radio Burst Source FRB 121102”. In: *The Astrophysical Journal* 882.2, p. L18. DOI: [10.3847/2041-8213/ab2c00](https://doi.org/10.3847/2041-8213/ab2c00).
- Li, D. et al. (2021). “A bimodal burst energy distribution of a repeating fast radio burst source”. In: *Nature* 598.7880, pp. 267–271. DOI: [10.1038/s41586-021-03878-5](https://doi.org/10.1038/s41586-021-03878-5).
- Luo, R. et al. (2020). “Diverse polarization angle swings from a repeating fast radio burst source”. In: *Nature* 586.7831, pp. 693–696. DOI: [10.1038/s41586-020-2827-2](https://doi.org/10.1038/s41586-020-2827-2).

- Lyubarsky, Yuri (2021). “Emission Mechanisms of Fast Radio Bursts”. In: *Universe* 7.3, p. 56. DOI: [10.3390/universe7030056](https://doi.org/10.3390/universe7030056).
- Michilli, D. et al. (2018). “An extreme magneto-ionic environment associated with the fast radio burst source FRB 121102”. In: *Nature* 553.7687, pp. 182–185. DOI: [10.1038/nature25149](https://doi.org/10.1038/nature25149).
- Nimmo, K. et al. (Feb. 2022). “Burst timescales and luminosities as links between young pulsars and fast radio bursts”. In: *Nature Astronomy* 6, pp. 393–401. DOI: [10.1038/s41550-021-01569-9](https://doi.org/10.1038/s41550-021-01569-9). arXiv: [2105.11446](https://arxiv.org/abs/2105.11446) [astro-ph.HE]. URL: <https://ui.adsabs.harvard.edu/abs/2022NatAs...6..393N>.
- Nita, Gelu M., Dale E. Gary, and Gregory Hellbourg (2016). “Spectral kurtosis statistics of quantized signals”. In: *2016 Radio Frequency Interference (RFI)*. IEEE. DOI: [10.1109/rfint.2016.7833535](https://doi.org/10.1109/rfint.2016.7833535).
- Oostrum, L. C. et al. (2020). “Repeating fast radio bursts with WSRT/Apertif”. In: *Astronomy & Astrophysics* 635, A61. DOI: [10.1051/0004-6361/201937422](https://doi.org/10.1051/0004-6361/201937422).
- Petroff, E., J. W. T. Hessels, and D. R. Lorimer (2022). “Fast radio bursts at the dawn of the 2020s”. In: *The Astronomy and Astrophysics Review* 30.1. DOI: [10.1007/s00159-022-00139-w](https://doi.org/10.1007/s00159-022-00139-w).
- Rajabi, Fereshteh et al. (2020). “A simple relationship for the spectro-temporal structure of bursts from FRB 121102”. In: *Monthly Notices of the Royal Astronomical Society* 498.4, pp. 4936–4942. DOI: [10.1093/mnras/staa2723](https://doi.org/10.1093/mnras/staa2723).
- Spitler, L. G. et al. (2014). “FAST RADIO BURST DISCOVERED IN THE ARECIBO PULSAR ALFA SURVEY”. In: *The Astrophysical Journal* 790.2, p. 101. DOI: [10.1088/0004-637x/790/2/101](https://doi.org/10.1088/0004-637x/790/2/101).
- Spitler, L. G. et al. (2016). “A repeating fast radio burst”. In: *Nature* 531.7593, pp. 202–205. DOI: [10.1038/nature17168](https://doi.org/10.1038/nature17168).

- Wang, Wei-Yang et al. (2022). “Magnetospheric Curvature Radiation by Bunches as Emission Mechanism for Repeating Fast Radio Bursts”. In: *The Astrophysical Journal* 927.1, p. 105. DOI: [10.3847/1538-4357/ac4097](https://doi.org/10.3847/1538-4357/ac4097).

Chapter 5

Summary and Conclusions

In this thesis I have explored the spectro-temporal properties of repeating fast radio bursts (FRBs) and the relationships between them guided by the predictions of the triggered relativistic dynamical model (TRDM; Rajabi et al. 2020). This chapter will summarize the thesis and its key conclusions, and discuss potential future work.

FRBs originate from (except for one) extragalactic sources and therefore are subject to significant propagation effects as they travel through the intergalactic medium. These propagation effects include dispersion, scintillation, and scattering. Dispersion affects an FRB by delaying the arrival time of lower frequency parts of the signal, by up to several seconds. The amount of dedispersion required to correct for the effect of dispersion is quantified with the dispersion measure (DM). In general, the greater the DM required, the greater the density of free ions along of sight.

After dedispersion, an FRB is on the order of milliseconds long, and there can remain a small delay in the arrival times of the lower frequency parts of a burst. When seen in a single pulse, this is called the sub-burst slope, or the frequency drift with time within a single pulse. When FRBs arrive with multiple distinct time resolved pulses, we see that the pulses with lower central frequencies tend to arrive later. This is called the sad-trombone drift rate.

The TRDM models FRBs as a narrow-band emission process originating from a cloud of material such a gas or a plasma that experiences motions potentially nearing relativistic

velocities. Using a relativistic transform, the TRDM makes predictions about spectro-temporal properties of FRBs such as their duration, sub-burst slopes, and drift rates that can be tested using measurements of observed FRBs. One such prediction that is key is that the sub-burst slope should be inversely proportional to the sub-burst duration.

In Chapter 2, we used several bursts from FRB20121102A spanning an order of magnitude in frequency and found that the slope of a sub-burst was in fact inversely proportional to its duration. Within the context of the TRDM, the good agreement found is consistent with the fact that all these bursts were emitted at the same frequency ν_0 when observed in each burst's rest frame.

Based on our analysis, all FRBs from repeating sources appear to have a well-defined sub-burst slope, which is not the case for FRBs from one-off sources. This is because bursts with multiple components have not been observed from one-off sources (Pleunis et al. 2021). Without a history of bursts with multiple components to constrain DMs for the source, the only reasonable way to dedisperse a one-off burst is to choose the DM that makes it as vertical as possible, and thus, no delay in arrival times in parts of the signal can be seen. This does not preclude the existence of sub-burst slopes in one-off FRBs, however it does make it much more challenging to investigate them.

In Dicke's Superradiance, the rest frame delay time τ'_D is expected to be about one order of magnitude larger than the rest frame burst duration τ'_w . This expectation is consistent with our fit to the sub-burst slope and duration relationship, where we found $A \equiv \tau'_w/\tau'_D \simeq 0.1$.

Scintillation and scattering can affect the measured values of spectro-temporal properties such as the sub-burst slope. However, since they affect all properties systematically, they cannot affect the relative values between them, and thus not the relationships observed between them. Instead, scintillation and scattering slide values along the trend of the relationship .

This analysis validates the TRDM for a small sample of bursts from FRB20121102A

and naturally leads to the question of can it be used for other sources? Is the TRDM common to repeating sources of FRBs? In Chapter 3 we examine this question and analyse the properties of bursts from additional repeating sources FRB20180814A and FRB20180916B.

Because the DM can greatly affect the value of the sub-burst slope measured we introduce a method of studying them by performing measurements over large ranges of DMs to estimate the uncertainty caused by the choice of DM. It is difficult to know what the true DM of a burst is given varying structures in bursts and the potentially time-varying nature of the DM for a source due to changes in its environment.

We found that even for a large range of DMs, the bursts from FRB20121102A, FRB20180814A, and FRB20180916B still exhibited an inverse relationship between their sub-burst slopes and durations. We found separate fits for each source and found that they were statistically consistent with being identical to one another, i.e. the same scaling of the relationship described all three sources. This result suggests a common law between different sources of repeating fast radio bursts.

If such a law holds and is common to different sources then it can be used to optimize the DM of a burst by choosing the DM such that it coincides with the expected law. To confirm this however, more sources need to be investigated with a larger number of bursts.

Before investigating the potential of a law common to multiple sources, I decided to investigate if all the bursts from a single source in fact strictly adhered to the same relationships. In Chapter 4, we examined a broad sample of 167 bursts across five observational studies of FRB20121102A with durations ranging from <1 ms to about 10 ms and frequencies ranging from ~ 1 to 7.5 GHz. Within this sample was a sub-sample of bursts selected based on their wait-times (the time between bursts) and burst energies. The sub-burst slope, duration, bandwidth, burst frequency and drift rate (when applicable) were measured for each burst over a large range of DMs. I performed these

measurements with a graphical user interface called FRBGUI that I developed to aid in preparing, reviewing and measuring the burst waterfalls.

Across this broad sample we confirmed our earlier results and again found that the sub-burst slope was inverse to the duration, as expected. We also found that the duration was inversely proportional to the frequency ($t_w \propto \nu_{\text{obs}}^{-1}$), the sub-burst slope was quadratic with the frequency ($d\nu_{\text{obs}}/dt_D \propto \nu_{\text{obs}}^2$), and the bandwidth was linear with frequency ($B_\nu \propto \nu_{\text{obs}}$), as expected from the TRDM and consistent with Doppler broadening.

However, we found an unexpected relationship between the bandwidth, duration and sub-burst slope. This relationship is of the form $B_\nu \propto t_w^{-1/2}$, and because of the inverse relationship with the sub-burst slope, $B_\nu \propto (d\nu_{\text{obs}}/dt_D)^{1/2}$. This relationship may be observational since the instruments used for the lower frequency bursts had low observing bandwidth, but this would not explain the lack of small bandwidth bursts at high frequency or the lack of short duration bursts with small bandwidth. This relationship is difficult to explain within the TRDM, as it implies that the duration of a pulse somehow determines the velocity extent of material in the source cloud, or vice-versa.

The drift rates we analysed followed similar relationships found for the sub-burst slopes, but only 12 were present in this sample and more are needed to confirm the relationships found. Wait-times and burst energies did not seem to have any correlations with any of the spectro-temporal properties. These results suggests that most spectro-temporal properties are largely determined by the TRDM, while other properties like wait-time, energy, and bandwidth are determined by the so far unknown details of the emission mechanism.

There are multiple possible avenues for further study implied by the results presented here. Given the general agreement of the TRDM with the spectro-temporal properties in the broad survey of FRB20121102A, it is important to add the bursts of more repeating sources to the plots of the relationships found. There are currently 24 repeaters known with thousands of bursts observed. A shared law would be a strong common element

between sources and an important tool for understanding repeating FRBs. Deviations from this law could be even more illuminating, and may indicate a hitherto unknown sub-classification of repeating FRBs. A shared law would also be important in precisely de-dispersing bursts from repeating FRBs and enable more careful analyses.

There is no guarantee that the drift rates of FRBs should follow similar relationships as those found for sub-burst slopes, but if they do (or do not), then this provides an additional constraint on physical models. Across the literature, few drift rates have been analysed compared to the total number of bursts. A focus on obtaining more of these for comparison with the relationships found for sub-burst slopes can provide additional clues on the emission of FRBs.

In the sample used for the survey of bursts from FRB20121102A, we saw a large dispersion in the measured values of spectro-temporal properties. Studying this statistical dispersion may provide information on the emission mechanism, as it is not clear why bursts are so varied in their properties.

More data is needed in the 2 GHz to 4 GHz bands especially for FRB20121102A, due to the large gaps in burst frequencies seen in our survey. Data in this band will help constrain the relationships we have found and provide more precise fits.

Additional observations and precise fits will be essential for understanding the unexpected bandwidth-duration-slope relationship found in FRB20121102A. Searches for high bandwidth, long duration bursts as well as for low bandwidth short duration bursts can help confirm the existence of this relationship. This relationship is only apparent across a broad frequency range, as significant dispersion in the observed bandwidths and durations of bursts makes these properties seem uncorrelated. If such a frequency range of bursts can be observed in other repeaters, observing the same relationship may provide another connection between them. The unique form of the bandwidth-duration-slope relationship may provide a strong constraint on models of the FRB emission mechanism.

Bibliography

- Pleunis, Ziggy et al. (June 8, 2021). “Fast Radio Burst Morphology in the First CHIME/FRB Catalog”. In: arXiv: [2106.04356](https://arxiv.org/abs/2106.04356) [[astro-ph.HE](#)].
- Rajabi, Fereshteh et al. (2020). “A simple relationship for the spectro-temporal structure of bursts from FRB 121102”. In: *Monthly Notices of the Royal Astronomical Society* 498.4, pp. 4936–4942. DOI: [10.1093/mnras/staa2723](https://doi.org/10.1093/mnras/staa2723).

Curriculum Vitae

Name: Mohammed Afif Chamma

Post-Secondary Education and Degrees: University of Western Ontario
London, Ontario, Canada
M.Sc. Astronomy
2016 – 2018

University of Ottawa
Ottawa, Ontario, Canada
Honours B.Sc. Physics & Mathematics with CO-OP
2011 – 2016

Honours and Awards: Ontario Graduate Scholarship
2021 – 2022

Ontario Graduate Scholarship
2019 – 2020

Related Work Experience: Teaching Assistant
University of Western Ontario
2016 – 2021

Western High Altitude Stratospheric Balloon Team, Researcher and Lead
University of Western Ontario
2018 – 2021

CO-OP Researcher
a) Accelerator Mass Spectrometry Laboratory at University of Ottawa
b) Physics Department at University of Ottawa
c) Statistics Canada
2014 – 2015

Software Developer
Benbria
2012 – 2013